

University of Trento  
University of Brescia  
University of Padova  
University of Trieste  
University of Udine  
University IUAV of Venezia

**CRACKS, SHEAR BANDS AND  
LAMELLAR INCLUSIONS  
IN HOMOGENEOUSLY  
PRESTRESSED MATERIALS**

Francesco Dal Corso

Advisor  
prof. D. Bigoni

2009

UNIVERSITY OF TRENTO

Graduate School in Structural Engineering

Modelling, Preservation and Controls of Materials and Structures

XXI Cycle

Ph.D. Program Head: prof. D. Bigoni

Final Examination: 26 March 2009

Board of Examiners:

Prof. Marco Savoia, University of Bologna

Prof. Guido Magenes, University of Pavia

Prof. Robert M. McMeeking, University of California, Santa Barbara

Prof. Stathis Bousias, University of Patras

# Summary

---

Localized deformation patterns are experimentally observed to prelude failure in many ductile materials (such as metal, alloy, granular material and plastic) and in quasi-brittle materials (such as concrete and rock). Moreover, the presence of a second phase in composites may promote failure due to stress concentrations at the inclusion boundaries.

In order to investigate shear bands nucleation, propagation and interaction with a second phase or a defect, analytical solutions for an infinite nonlinear elastic solid subject to a uniform far-field deformation increment are obtained for the following types of inclusion:

- i) A crack, revealing features related to the interaction between shear bands and crack tip fields. This solution is also fundamental to the understanding of the shear band problem;
- ii) A rigid line inclusion, the so-called ‘stiffener’, showing the emergence of shear bands at the stiffener tips in highly deformed ductile materials. For null prestress the solution is shown to match correctly with photoelastic experiments and to predict the fracture patterns for a brittle material containing a stiffener;
- iii) A pre-existing shear band, showing that the deformation is highly focussed and aligned coaxial to the shear band and the energy release rate to blow up to infinity, for incremental loading occurring when the prestress approaches the elliptic boundary, so that the propagation becomes ‘unrestrainable’.

All these analytical results substantiate the experimental observations that shear bands emerge at the inclusion tips and they are preferential near-failure deformation modes.

# Sommario

---

In molti materiali duttili (come metalli, leghe, materiali granulari e plastiche) e quasi fragili (come cemento e rocce) si osservano sperimentalmente percorsi di deformazione localizzata prima della rottura. Inoltre, la presenza nei compositi di una seconda fase può favorire la rottura a causa della concentrazione degli sforzi in vicinanza dell'inclusione.

Al fine di studiare la nucleazione di shear band, la propagazione e la loro interazione con una seconda fase o un difetto, si ottengono soluzioni analitiche per un solido elastico non lineare soggetto ad un incremento di deformazione uniforme all'infinito per i seguenti tipi di inclusione:

- i) Frattura; la soluzione mostra l'interazione tra le shear band e i campi vicini a una frattura. Tale soluzione risulta fondamentale anche nella comprensione del problema della shear band;
- ii) Inclusione lineare rigida 'stiffener'; la soluzione mostra la nascita delle shear band agli apici dello stiffener in materiali duttili e, per valori nulli di prestress, risulta essere in accordo con esperimenti fotoelastici e capace di predire i percorsi di frattura in materiali fragili contenenti tali inclusioni;
- iii) Shear band preesistente; la soluzione mostra una deformazione altamente concentrata e allineata coassialmente alla shear band e dimostra che, per incrementi di carico sovrapposti ad un prestress prossimo alla perdita di ellitticità, l'energy release rate incrementale diventa infinito e pertanto la propagazione della shear band diventa 'inarrestabile'.

Tutti questi risultati analitici confermano le osservazioni sperimentali relative alla nascita delle shear band agli apici delle inclusioni ed al fatto che esse rappresentino un modo di deformazione preferenziale in prossimità della rottura.

# Acknowledgements

---

The constant optimism and great enthusiasm of my advisor, Prof. Davide Bigoni, have been fundamentals during these years. I would like to express profound gratitude to him for his remarks, suggestions and encouragements throughout this research work.

I am grateful to all members of the group of solid mechanics at the University of Trento, in particular I am highly thankful to Dr. Massimiliano Gei for his cooperation and to Giovanni Noselli for the experiments performed at the Teaching Lab. for Physical Modeling of Structures and Photoelasticity (managed by Prof. Davide Bigoni) and at the Materials and Structural Testing Lab. (managed by Prof. Riccardo Zandonini).

Finally, I am especially indebted to all my family and, above all, I express my thanks to my beloved wife Elena for her heart, patience and never-ending support.

Trento, September 2008

Francesco Dal Corso

## Published papers

---

The main results presented in this thesis have been summarized in the following papers:

- 1) Dal Corso, F., Bigoni, D. and Gei, M. (2008). The stress concentration near a rigid line inclusion in a prestressed, elastic material. Part I. Full field solution and asymptotics. *J. Mech. Phys. Solids* **56**, 815–838;
- 2) Bigoni, D., Dal Corso, F. and Gei, M. (2008). The stress concentration near a rigid line inclusion in a prestressed, elastic material. Part II. Implications on shear band nucleation, growth and energy release rate. *J. Mech. Phys. Solids* **56**, 839–857;
- 3) Bigoni, D. and Dal Corso, F. (2008). The unrestrainable growth of a shear band in a prestressed material. *Proc. R. Soc. A* **464**, 2365–2390;
- 4) Dal Corso, F. and Bigoni, D. (2009). The interactions between shear bands and rigid lamellar inclusions in a ductile metal matrix. *Proc. R. Soc. A* **465**, 143–163.

# Contents

---

<b>1</b>	<b>Introduction</b>	<b>1</b>
<b>2</b>	<b>Incremental constitutive equations</b>	<b>5</b>
2.1	Biot constitutive equations . . . . .	6
2.2	Specific cases of material behaviour . . . . .	7
2.2.1	Mooney-Rivlin material . . . . .	8
2.2.2	$J_2$ -deformation theory of plasticity . . . . .	8
2.3	Positive definiteness of constitutive tensor . . . . .	10
2.4	Strong ellipticity and ellipticity . . . . .	11
2.5	Regime classification . . . . .	12
2.6	Shear band inclinations . . . . .	15
2.7	Shear banding as an initial bifurcation mode . . . . .	19
2.8	Surface bifurcation . . . . .	20
<b>3</b>	<b>Crack in a prestressed material</b>	<b>23</b>
3.1	Crack parallel to an orthotropy axis . . . . .	26
3.1.1	Mode I . . . . .	27
3.1.2	Mode II . . . . .	31
3.1.3	Incremental stress intensity factors . . . . .	35
3.1.4	Crack solution and surface bifurcation condition . . . . .	35
3.2	Crack inclined with respect to the orthotropy axes . . . . .	36
3.3	Shear bands interacting with a finite-length crack . . . . .	39
3.4	Incremental energy release rate for crack growth . . . . .	44

<b>4</b>	<b>Stiffener in a prestressed material</b>	<b>49</b>
4.1	Stiffener parallel to an orthotropy axis . . . . .	55
4.1.1	Asymptotic solution . . . . .	56
4.1.2	The strange failure modes near a stiffener in a brittle material . . . . .	66
4.1.3	Full-field solution for a uniform incremental Mode I at infinity . . . . .	68
4.1.4	Incremental stress intensity factors . . . . .	75
4.1.5	Shear bands interacting with a stiffener . . . . .	76
4.2	Stiffener inclined with respect to the orthotropy axes . . . . .	84
4.3	Incremental solution in the parabolic and hyperbolic regimes . . . . .	89
4.4	Incremental energy release rate for stiffener growth . . . . .	93
4.4.1	Stiffener parallel to the orthotropy axis . . . . .	97
4.4.2	The inclined stiffener . . . . .	99
4.4.3	The incremental axial force in the stiffener under Mode I perturbation . . . . .	100
<b>5</b>	<b>Shear band in a prestressed material</b>	<b>105</b>
5.1	The shear band model . . . . .	107
5.2	The stress state near a shear band and its propagation . . . . .	109
5.2.1	Shear band at the EI/P boundary . . . . .	109
5.2.2	Shear band at the EC/H boundary . . . . .	110
<b>A</b>	<b>Experiments on samples containing a thin platelet</b>	<b>117</b>
<b>B</b>	<b>Material behaviour</b>	<b>121</b>
B.1	The Mooney-Rivlin material . . . . .	121
B.2	The $J_2$ -deformation theory of plasticity . . . . .	122
<b>C</b>	<b>Simple boundary value problems in finite elasticity</b>	<b>125</b>
C.1	Uniaxial plane strain elongation . . . . .	125
C.2	Simple shear of an elastic block . . . . .	130
<b>D</b>	<b>Prescribed rigid-rotation of a stiffener</b>	<b>139</b>
<b>E</b>	<b>A stiffener embedded in a classical elastic material</b>	<b>143</b>
	<b>Nomenclature</b>	<b>145</b>
	<b>Bibliography</b>	<b>147</b>

# Chapter 1

---

## Introduction

Localized deformation patterns are experimentally observed to prelude failure in many ductile materials (such as metal, alloy, granular material, plastic) and in quasi-brittle materials (such as concrete and rock). Moreover, the presence of a second phase in composites may promote failure due to stress concentrations at the phase boundaries. In these cases numerical approaches have hardly the necessary resolution to detail the mechanical fields and only analytical solutions permit to disclose the mechanisms of failure in highly-deformed composite materials.

The main goal of this thesis is to provide analytical solutions for nonlinear elastic solids containing a dilute suspension of ‘thin defects’ [modeled as fractures, rigid line inclusions (stiffeners) and pre-existing shear bands] and to investigate the shear bands nucleation, propagation and interaction with a second phase.

The incremental constitutive equations used to describe nonlinear materials are briefly introduced in Chapter 2 together with the condition for their positive definiteness, specific cases of material behavior, ellipticity and regime classification of the incremental constitutive equations, surface instability and shear band inclination.

The full-field solution for a finite-length crack in a prestressed material is provided in Chapter 3. This solution is new in the case when the crack is inclined with respect to the material orthotropic axes and it is fundamental to the understanding of the shear band problem treated in Chapter 5. Moreover, this solution is interesting in itself since reveals features related to the interaction between shear bands and crack tip fields, so that it may explain experimental observations relative to crack growth in ductile materials.

A rigid line inclusion, a so-called ‘stiffener’, embedded in a prestressed material incrementally loaded is considered in Chapter 4. The obtained analytical solutions explain the experimentally observed emergence of shear bands at the stiffener tips in highly deformed ductile materials (see Fig. 1.1). For

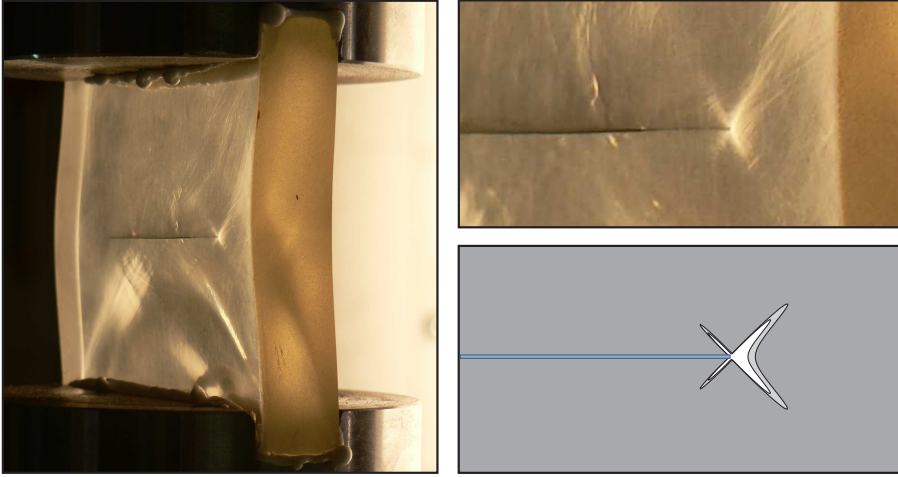


Figure 1.1: Two-component epoxy resin sample (sample S3, see appendix A) containing an aluminum platelet loaded uniaxially in vertical compression (photo taken at the University of Trento at a 50 MPa of compressive stress, experiment performed by G. Noselli). Light reflection evidences strain localization at the end of the platelet (clearly visible in the detail on the right, upper part). Note the similarity with the analytical solution (obtained in §4.1.3) reported on the right, lower part (for a highly anisotropic material,  $\xi = 0.015$ , without prestress,  $k = 0$ , near the boundary of ellipticity loss).

null prestress the solution is shown to match correctly with photoelastic experiments (see Fig. 1.2). These experiments also confirm the fracture patterns for a brittle material containing a stiffener (see Fig. 1.3), which do not obey a hoop-stress criterion and result completely different from those found for cracks. Moreover, the incremental energy release rate and incremental  $J$ -integral are derived, related to a reduction (or growth inhibition) of the stiffener.

Finally, in Chapter 5 a weak line inclusion model is introduced to analytically quantify and investigate the stress state and the growth conditions of a finite-length pre-existing shear band in a prestressed material. The deformation is shown to become highly focussed and aligned coaxial to the shear band –a finding that provides justification for the experimentally observed

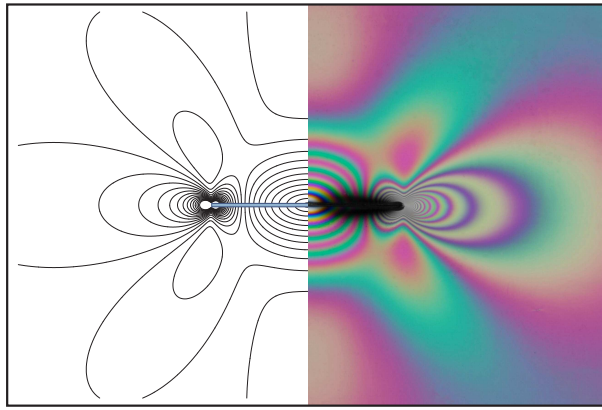


Figure 1.2: Isochromatic fringe pattern obtained employing a transmission photoelastic test at 0.11 MPa mean tensile loading on a two-component epoxy resin sample (sample S1, see appendix A) containing an aluminum platelet (photo taken at the University of Trento, experiment performed by G. Noselli). Photoelastic results (right) are compared with theoretical solution (left) in terms of in-plane principal stress difference contours plotted for an incompressible and isotropic elastic material, initially unstressed, and deformed in plane strain (see appendix A for a full discussion).



Figure 1.3: Growth of two fractures at the end of an aluminum platelet embedded in a two-component epoxy resin sample (sample S2, see appendix A) under tensile loading (photos taken at the University of Trento, experiment performed by G. Noselli). Both fractures have initiated horizontally (at a mean stress near to 30 MPa), where the stiffener is still attached to the resin.

strong tendency towards rectilinear propagation– and the energy release rate to blow up to infinity, for incremental loading occurring when the prestress approaches the elliptic boundary. It is concluded that the propagation be-

comes ‘unrestrainable’, a result substantiating the experimental observation that shear bands are preferential near-failure deformation modes.

## Chapter 2

---

### Incremental constitutive equations for incompressible nonlinear elasticity

*The incremental constitutive equations used later are briefly introduced. Positive definiteness, specific cases of material behaviour, ellipticity and regime classification of the incremental constitutive equations, surface instability and shear band inclinations are also reported.*

Small elastic deformations superimposed upon a given state of finite deformation are considered within the framework of incremental nonlinear elasticity. We refer to the two-dimensional Biot (1965) theory of incompressible elasticity. This theory is of great importance, since it provides a simple but rigorous approach to the behaviour of prestressed solids. In fact, incompressible elasticity is an important model for finitely strained materials for the following reasons:

- i) rubber, which is an important material capable of large elastic strain, is nearly incompressible;
- ii) finite strain elasticity is often used as a model for the plastic branch of severely deformed ductile metals; for these materials the plastic deformation is incompressible and dominates the elastic small deformation (although with such a model it is not possible to analyze unloading);
- iii) the equations governing deformations of incompressible elasticity are in some cases easier to handle for obtaining analytical solutions [although from numerical point of view incompressibility remains always a problem,

which can be emended using various techniques, for instance boundary elements methods (Brun et al. 2003a, 2003b; Bigoni et al. 2007)].

Therefore, specific cases of material behaviour, namely the Mooney–Rivlin and  $J_2$ -deformation theory of plasticity materials, are presented (§2.2).

## 2.1 Biot constitutive equations

An incompressible, nonlinear elastic material is considered, deformed under plane strain condition. According to the Biot (1965) theory, the response to an incremental loading is expressed in terms of the nominal (unsymmetrical) stress<sup>1</sup> increment  $\dot{\mathbf{t}}$  related to the gradient of incremental displacement  $\nabla \mathbf{v}$ , satisfying the incompressibility constraint (the usual summation convention for repeated indices is assumed),

$$\text{tr} \nabla \mathbf{v} = v_{i,i} = v_{1,1} + v_{2,2} = 0, \quad (2.1)$$

through the linear relation

$$\dot{\mathbf{t}} = \mathbb{G}[\nabla \mathbf{v}^T] + \dot{p} \mathbf{I}, \quad (2.2)$$

where the apex T denotes the transpose,  $\dot{p}$  is the incremental in-plane mean stress and the components of constitutive fourth-order tensor  $\mathbb{G}$  (possessing the major symmetry  $\mathbb{G}_{ijkl} = \mathbb{G}_{klij}$ ) are:

$$\begin{aligned} \mathbb{G}_{1111} &= \mu(\xi - k - \eta), & \mathbb{G}_{1122} &= -\mu \xi, & \mathbb{G}_{1112} &= \mathbb{G}_{1121} = 0, \\ \mathbb{G}_{2211} &= -\mu \xi, & \mathbb{G}_{2222} &= \mu(\xi + k - \eta), & \mathbb{G}_{2212} &= \mathbb{G}_{2221} = 0, \\ \mathbb{G}_{1212} &= \mu(1 + k), & \mathbb{G}_{1221} &= \mathbb{G}_{2112} = \mu(1 - \eta), & \mathbb{G}_{2121} &= \mu(1 - k). \end{aligned} \quad (2.3)$$

The components (2.3) of the constitutive fourth-order tensor  $\mathbb{G}$  depend on the current state of stress (expressed through the principal components of Cauchy stress,  $T_1$  and  $T_2$ ) and material response to shear ( $\mu$  for shear parallel and  $\mu_*$  for shear inclined at  $\pi/4$  with respect to  $T_1$ )<sup>2</sup> describing orthotropy (aligned

<sup>1</sup>The Cauchy stress tensor  $\mathbf{T}$  and the nominal stress tensor  $\mathbf{t}$  are related through  $\mathbf{T} = J^{-1} \mathbf{F} \mathbf{t}$ , where  $\mathbf{F}$  is the deformation gradient and  $J = \det \mathbf{F} = 1$  for incompressibility.

<sup>2</sup>The two incremental moduli  $\mu$  and  $\mu_*$  were given by Biot (1965) (see Appendix A by Brun et al. 2003a for details) in the form

$$\begin{aligned} \mu &= \frac{1}{2} \frac{\lambda_1^2 + \lambda_2^2}{\lambda_1^2 - \lambda_2^2} \left( \lambda_1 \frac{\partial W}{\partial \lambda_1} - \lambda_2 \frac{\partial W}{\partial \lambda_2} \right), \\ \mu_* &= \frac{1}{4} \left( \lambda_1 \frac{\partial W}{\partial \lambda_1} + \lambda_2 \frac{\partial W}{\partial \lambda_2} + \lambda_1^2 \frac{\partial^2 W}{\partial \lambda_1^2} + \lambda_2^2 \frac{\partial^2 W}{\partial \lambda_2^2} - 2\lambda_1 \lambda_2 \frac{\partial^2 W}{\partial \lambda_1 \partial \lambda_2} \right), \end{aligned} \quad (2.4)$$

parallel to the current principal stress directions), see Bigoni and Capuani (2002; 2005) for details, through the dimensionless quantities:

$$\xi = \frac{\mu_*}{\mu}, \quad \eta = \frac{T_1 + T_2}{2\mu}, \quad k = \frac{T_1 - T_2}{2\mu}. \quad (2.5)$$

Finally, we note that the constitutive eqns. (2.2)–(2.3) can be rewritten in the useful form

$$\begin{aligned} \dot{t}_{11} &= \mu(2\xi - k - \eta)v_{1,1} + \dot{p}, \\ \dot{t}_{22} &= \mu(2\xi + k - \eta)v_{2,2} + \dot{p}, \\ \dot{t}_{12} &= \mu[(1 + k)v_{2,1} + (1 - \eta)v_{1,2}], \\ \dot{t}_{21} &= \mu[(1 - \eta)v_{2,1} + (1 - k)v_{1,2}]. \end{aligned} \quad (2.6)$$

## 2.2 Specific cases of material behaviour

For initially isotropic materials under plane strain condition, Biot (1965) obtained the following relation for the deviatoric dimensionless parameter  $k$ , eqn. (2.5)<sub>3</sub>,

$$k = \frac{\lambda^4 - 1}{\lambda^4 + 1}, \quad (2.7)$$

where  $\lambda = \lambda_1$  is the principal stretch, representing a prestrain measure.

In terms of logarithmic strains  $\epsilon_i = \ln \lambda_i$  ( $i = 1, \dots, 3$ ), the deviatoric dimensionless parameter  $k$ , eqn. (2.7), becomes

$$k = \tanh(2\epsilon_1). \quad (2.8)$$

We note from (2.8) that:

$$|k| < 1, \quad \text{and in particular} \quad \begin{cases} k = 0, & \text{for } \epsilon_1 = 0; \\ k \rightarrow \pm 1, & \text{for } \epsilon_1 \rightarrow \pm\infty. \end{cases} \quad (2.9)$$

Differently from  $k$ , the shear moduli ratio  $\xi$ , eqn. (2.5)<sub>1</sub>, is given by the assumption of a specific material model [as shown for Mooney–Rivlin (§2.2.1) and for J<sub>2</sub>-deformation theory (§2.2.2) materials].

---

where  $W(\lambda_1, \lambda_2, \lambda_3)$  represents the strain energy density function [and  $\lambda_i$  ( $i=1,2,3$ ) are the principal stretches].

### 2.2.1 Mooney-Rivlin material

For a Mooney-Rivlin material (see appendix B.1 for details), useful to model isotropic rubber-like elastic media, we have

$$\mu = \mu_* = \frac{\mu_0}{2} (\lambda_1^2 + \lambda_2^2), \quad (2.10)$$

where  $\mu_0$  is the initial shear modulus (C.12), so that

$$\xi = 1. \quad (2.11)$$

The curve for a Mooney-Rivlin material is reported in Fig. 2.1 in the  $k$ - $\xi$  plane.

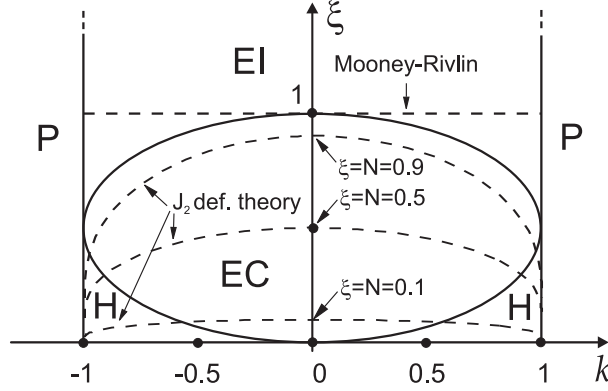


Figure 2.1: Relation between stress deviator  $k$  and anisotropy coefficient  $\xi$  for Mooney-Rivlin and  $J_2$ -deformation theory materials. For a  $J_2$ -material the hardening exponent  $N$  has been taken equal to 0.1, 0.5 and 0.9. Note that the EC/H boundary is always approached for every hardening coefficient, while the EI/P boundary is approached for a Mooney-Rivlin material for infinite stretch  $\lambda$ .

### 2.2.2 $J_2$ -deformation theory of plasticity

For a  $J_2$ -deformation theory of plasticity (see appendix B.2 for details), particularly suited to analyse the plastic branch of the constitutive response of ductile metals, we have

$$\begin{aligned} \mu &= \frac{1}{3} E_s (\epsilon_1 - \epsilon_2) \coth (\epsilon_1 - \epsilon_2), \\ \mu_* &= \frac{1}{9} \frac{E_s}{\epsilon_e^2} \left[ 3(\epsilon_1 + \epsilon_2)^2 + N(\epsilon_1 - \epsilon_2)^2 \right], \end{aligned} \quad (2.12)$$

where  $E_s = E_s(\epsilon_e)$  is a secant modulus (B.13),  $N \in ]0, 1]$  is a strain hardening exponent and  $\epsilon_e$  is the effective strain (B.11)<sub>2</sub>. In the plane strain case ( $\epsilon_3 = 0$  and  $\epsilon_1 = -\epsilon_2$ ), we obtain

$$\mu = \frac{2\epsilon_1}{3} E_s \coth(2\epsilon_1), \quad \mu_* = \frac{N}{3} E_s, \quad (2.13)$$

so that

$$\xi = \frac{N(\lambda^4 - 1)}{2(\ln \lambda)(\lambda^4 + 1)}, \quad (2.14)$$

or, alternatively,

$$\xi = \frac{N}{2\epsilon_1} \tanh(2\epsilon_1). \quad (2.15)$$

We note from (2.15) that:

$$0 < \xi < N, \quad \text{and in particular} \quad \begin{cases} \xi = N, & \text{for } \epsilon_1 = 0; \\ \xi \rightarrow 0, & \text{for } \epsilon_1 \rightarrow \pm\infty. \end{cases} \quad (2.16)$$

The curves for a  $J_2$ -deformation theory material described by eqn. (2.14) are reported in Fig. 2.1 for different values of  $N$  in the  $k$ - $\xi$  plane while the incremental shear modulus  $\mu$  and  $\mu_*$  (2.13) normalized through division by  $K$  (positive constitutive parameter, see Appendix B.2 for details) are reported in Fig. 2.2.

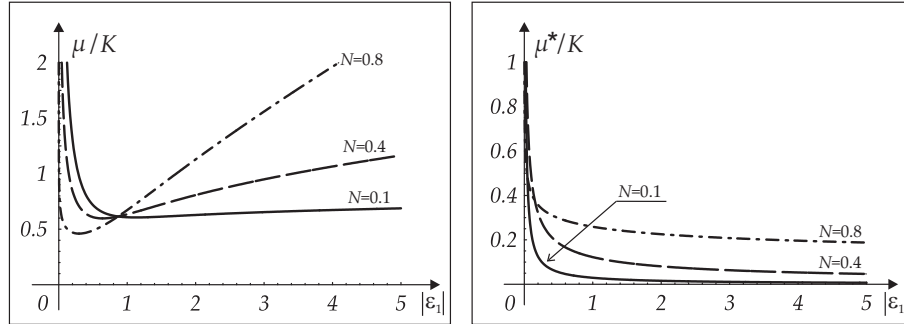


Figure 2.2: Incremental shear modulus  $\mu$  (left) and  $\mu_*$  (right) for a  $J_2$ -material, eqn. (2.13), normalized through division by  $K$  (positive constitutive parameter, see Appendix B.2 for details) versus the principal strain  $\epsilon_1 = \ln \lambda_1$  for different values of the hardening parameter  $N$ . Note that at null prestress ( $\epsilon_1 = 0$ ) both  $\mu$  and  $\mu_*$  tend to infinity so that a  $J_2$ -deformation theory material becomes incrementally rigid.

### 2.3 Positive definiteness of constitutive tensor

Positive definiteness of the constitutive fourth-order tensor  $\mathbb{G}$  (2.3) is a local sufficient condition for uniqueness which, in the two-dimensional context and under the incompressibility constraint (2.1), can be written as

$$v_{j,i}\mathbb{G}_{ijkl}v_{l,k} > 0, \quad v_{2,2} = -v_{1,1}, \quad (2.17)$$

which can be developed to yield the single condition (note that  $v_{2,2}$  has been eliminated using incompressibility)

$$(\mathbb{G}_{1111} - 2\mathbb{G}_{1122} + \mathbb{G}_{2222})v_{1,1}^2 + \mathbb{G}_{2121}v_{1,2}^2 + 2\mathbb{G}_{1221}v_{1,2}v_{2,1} + \mathbb{G}_{1212}v_{2,1}^2 > 0 \quad (2.18)$$

an expression coincident with the analogous equation by Hill and Hutchinson [1975, their eqn. (2.9)]<sup>3</sup>.

Since all components of the velocity gradient appearing in eqn. (2.18) are free parameters, the necessary and sufficient conditions for the positive definiteness to hold are

$$\mathbb{G}_{1111} - 2\mathbb{G}_{1122} + \mathbb{G}_{2222} > 0, \quad \mathbb{G}_{1212} > 0, \quad \mathbb{G}_{2121}\mathbb{G}_{1212} - \mathbb{G}_{1221}^2 > 0, \quad (2.19)$$

which, assuming  $\mu > 0$ , can be written in terms of dimensionless constants (2.5) as

$$0 < \eta < 2\xi, \quad \frac{k^2 + \eta^2}{2\eta} < 1, \quad (2.20)$$

which, in the  $k$ - $\xi$  plane and for  $\eta = k$ , is the region between the vertical axis and the lines  $\xi = k/2$  and  $k = 1$  (Fig. 2.5).

Since in the particular case  $0 < \eta = k < 1$  and  $\xi = 1$  conditions (2.20) are satisfied,

*bifurcation is always excluded for plane strain uniaxial tension of a Mooney-Rivlin material.*

For uniaxial plane strain tension  $\eta = k > 0$  parallel to the  $x_1$ -axis of a  $J_2$ -deformation theory material, a substitution of eqns. (2.15) into conditions (2.20) yields

$$0 < \varepsilon_1 < N, \quad \text{with } T_2 = 0, \quad (2.21)$$

while  $T_1$  is obviously positive.

---

<sup>3</sup>There is a misprint in that equation, their term  $+1/2(\sigma_1 + \sigma_2)$  reads  $+1/2(\sigma_1 - \sigma_2)$ .

## 2.4 Strong ellipticity and ellipticity

In the two-dimensional context and under the incompressibility constraint, strong ellipticity [or ellipticity] condition, can be written as

$$g_j n_i \mathbb{G}_{ijkl} n_k g_l > 0, \quad [\text{or } \neq 0], \quad (2.22)$$

where the two unit vectors  $\mathbf{n}$  and  $\mathbf{g}$  are orthogonal to each other [so that the incompressibility constraint is automatically satisfied] and given in components by

$$\{\mathbf{n}\} = \{\cos \gamma, \sin \gamma\}, \quad \{\mathbf{g}\} = \{-\sin \gamma, \cos \gamma\}, \quad (2.23)$$

so that  $\gamma$  is the angle between  $\mathbf{n}$  and the  $x_1$ -axis, see Fig. 2.3.

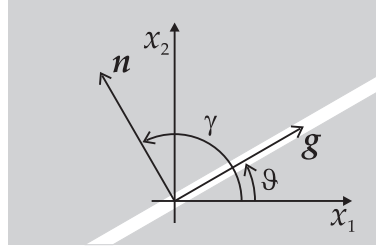


Figure 2.3: Unit vectors  $\mathbf{n}$  (normal to the shear band) and  $\mathbf{g}$  (parallel to the shear band) in the  $x_1$ - $x_2$  plane.

Condition (2.22) yields

$$\begin{aligned} & \mathbb{G}_{1212} \cos^4 \gamma + \mathbb{G}_{2121} \sin^4 \gamma + (\mathbb{G}_{1111} - 2\mathbb{G}_{1122} - 2\mathbb{G}_{1221} \\ & + \mathbb{G}_{2222}) \cos^2 \gamma \sin^2 \gamma > 0, \quad [\text{or } \neq 0], \quad \forall \gamma, \end{aligned} \quad (2.24)$$

which, keeping into account the definition (2.3) of coefficients  $\mathbb{G}_{ijkl}$ , becomes

$$\mu \sin^4 \gamma [(1+k) \cot^4 \gamma + 2(2\xi - 1) \cot^2 \gamma + 1 - k] > 0, \quad [\text{or } \neq 0], \quad \forall \gamma, \quad (2.25)$$

equivalent<sup>4</sup> to the three following inequalities

$$\mu > 0, \quad [\text{or } \mu \neq 0], \quad k^2 < 1, \quad 2\xi > 1 - \sqrt{1 - k^2}. \quad (2.27)$$

<sup>4</sup>Note that eqn. (2.25) can be rewritten as

$$\mu \cos^4 \gamma [(1-k) \tan^4 \gamma + 2(2\xi - 1) \tan^2 \gamma + 1 + k] > 0, \quad [\text{or } \neq 0], \quad \forall \gamma. \quad (2.26)$$

For the material model under consideration, we conclude that, *assuming*  $\mu > 0$ , *ellipticity and strong ellipticity are equivalent criteria.*

Outside the elliptic boundary, localized solutions in terms of shear bands become possible. A discussion on these is presented in §2.6.

## 2.5 Regime classification

In the absence of body forces, incremental equilibrium,

$$\dot{t}_{ij,i} = 0, \quad (2.28)$$

yields for a *uniformly prestressed solid* the following two equations

$$\begin{aligned} \dot{p}_{,1} &= \mu[(1+k-2\xi)v_{1,11} - (1-k)v_{1,22}], \\ \dot{p}_{,2} &= \mu[(1-k-2\xi)v_{2,22} - (1+k)v_{2,11}], \end{aligned} \quad (2.29)$$

that, together with the incompressibility constraint (2.1), provide a system of partial differential equations for  $v_1, v_2$  and  $\dot{p}$ .

Since the material is incompressible, we can introduce a typical expedient of two-dimensional Fluid Mechanics (Ladyzhenskaya, 1963), namely, a *stream function*  $\psi(x_1, x_2)$  with the property

$$v_1 = \psi_{,2}, \quad v_2 = -\psi_{,1}, \quad (2.30)$$

so that the incompressibility constraint is automatically satisfied, while the elimination of  $\dot{p}$  in eqns. (2.29) gives the fourth-order partial differential equation

$$(1+k)\psi_{,1111} + 2(2\xi-1)\psi_{,1122} + (1-k)\psi_{,2222} = 0, \quad (2.31)$$

derived by Biot [1965, pp. 193, his eqn. (3.7), see also Hill and Hutchinson, 1975, their eqn. (3.3)].

Following Lekhnitskii (1981), a solution of (2.31) can be represented in terms of the analytic function  $F$

$$\psi(x_1, x_2) = F(x_1 + \Omega x_2), \quad (2.32)$$

where  $\Omega$  is a complex constant satisfying the biquadratic equation obtained inserting representation (2.32) in eqn. (2.31),

$$1 + k + 2(2\xi - 1)\Omega^2 + (1 - k)\Omega^4 = 0. \quad (2.33)$$

The four roots  $\Omega_j$  ( $j = 1, \dots, 4$ ) of eqn. (2.33) satisfy<sup>5</sup>

$$\Omega_j^2 = \frac{1 - 2\xi + (-1)^j \sqrt{4\xi^2 - 4\xi + k^2}}{1 - k}, \quad (2.34)$$

and are real or complex depending on the values of  $\xi$  and  $k$ . In compact form, we write

$$\Omega_j = \alpha_j + i\beta_j, \quad j = 1, \dots, 4, \quad (2.35)$$

and define the four complex variables

$$z_j = x_1 + \Omega_j x_2 = x_1 + \alpha_j x_2 + i\beta_j x_2, \quad j = 1, \dots, 4, \quad (2.36)$$

where  $i = \sqrt{-1}$  is the imaginary unit and  $\alpha_j = \text{Re}[\Omega_j]$  and  $\beta_j = \text{Im}[\Omega_j]$ .

Through eqns. (2.32) and (2.36), the general solution of the differential eqn. (2.31) can be written as

$$\psi(x_1, x_2) = \sum_{j=1}^4 F_j(z_j). \quad (2.37)$$

The roots  $\Omega_j$ , defined by eqn. (2.34) and changing their nature according to the values taken by parameters  $\xi$  and  $k$ , can be classified as follows.

- In the *elliptic imaginary regime* (EI), defined as

$$k^2 < 1 \quad \text{and} \quad 2\xi > 1 + \sqrt{1 - k^2}, \quad (2.38)$$

we have *four imaginary conjugate roots*

$$\Omega_1 = i\beta_1, \quad \Omega_2 = i\beta_2, \quad \Omega_3 = \bar{\Omega}_1, \quad \Omega_4 = \bar{\Omega}_2, \quad (2.39)$$

where

$$\left. \begin{array}{l} \beta_1 \\ \beta_2 \end{array} \right\} = \sqrt{\frac{2\xi - 1 \pm \sqrt{4\xi^2 - 4\xi + k^2}}{1 - k}} > 0. \quad (2.40)$$

- In the *elliptic complex regime* (EC), defined as

$$k^2 < 1 \quad \text{and} \quad 1 - \sqrt{1 - k^2} < 2\xi < 1 + \sqrt{1 - k^2}, \quad (2.41)$$

we have *four complex conjugate roots*

$$\Omega_1 = -\alpha + i\beta, \quad \Omega_2 = \alpha + i\beta, \quad \Omega_3 = \bar{\Omega}_1, \quad \Omega_4 = \bar{\Omega}_2, \quad (2.42)$$

---

<sup>5</sup>It may be instructive to compare eqns. (2.33) and (2.25).

where

$$\left. \begin{array}{l} \beta \\ \alpha \end{array} \right\} = \sqrt{\frac{\sqrt{1-k^2} \pm (2\xi - 1)}{2(1-k)}} > 0. \quad (2.43)$$

- In the *hyperbolic regime* (H), defined as

$$k^2 < 1 \quad \text{and} \quad 2\xi < 1 - \sqrt{1-k^2}, \quad (2.44)$$

we have *four real roots*

$$\Omega_1 = \alpha_1, \quad \Omega_2 = \alpha_2, \quad \Omega_3 = -\Omega_1, \quad \Omega_4 = -\Omega_2, \quad (2.45)$$

where

$$\left. \begin{array}{l} \alpha_1 \\ \alpha_2 \end{array} \right\} = \sqrt{\frac{1 - 2\xi \pm \sqrt{4\xi^2 - 4\xi + k^2}}{1-k}} > 0. \quad (2.46)$$

- In the *parabolic regime* (P), defined as

$$k^2 > 1, \quad (2.47)$$

we have *two real and two imaginary roots*

$$\Omega_1 = \alpha, \quad \Omega_2 = i\beta, \quad \Omega_3 = -\Omega_1, \quad \Omega_4 = -\Omega_2, \quad (2.48)$$

where

$$\left. \begin{array}{l} \alpha \\ \beta \end{array} \right\} = \sqrt{\frac{\sqrt{4\xi^2 - 4\xi + k^2} \pm (1 - 2\xi)}{1-k}} > 0 \quad \text{if} \quad k < -1, \quad (2.49)$$

and

$$\left. \begin{array}{l} \alpha \\ \beta \end{array} \right\} = \sqrt{\frac{-\sqrt{4\xi^2 - 4\xi + k^2} \pm (1 - 2\xi)}{1-k}} > 0 \quad \text{if} \quad k > 1. \quad (2.50)$$

A sketch of geometrical representation of the roots  $\Omega_j$  in the complex plane is given in Fig. 2.4, with respect to the different regimes.

The regime classification in the  $k - \xi$  plane has been given by Radi et al. (2002, their Fig. 2) and is now reported in Fig. 2.5. The assumption of a specific material model (§2.2) determines the relation between  $\xi$  and  $k$ , which is graphically represented by a curve in the  $k - \xi$  plane of Fig. 2.1.

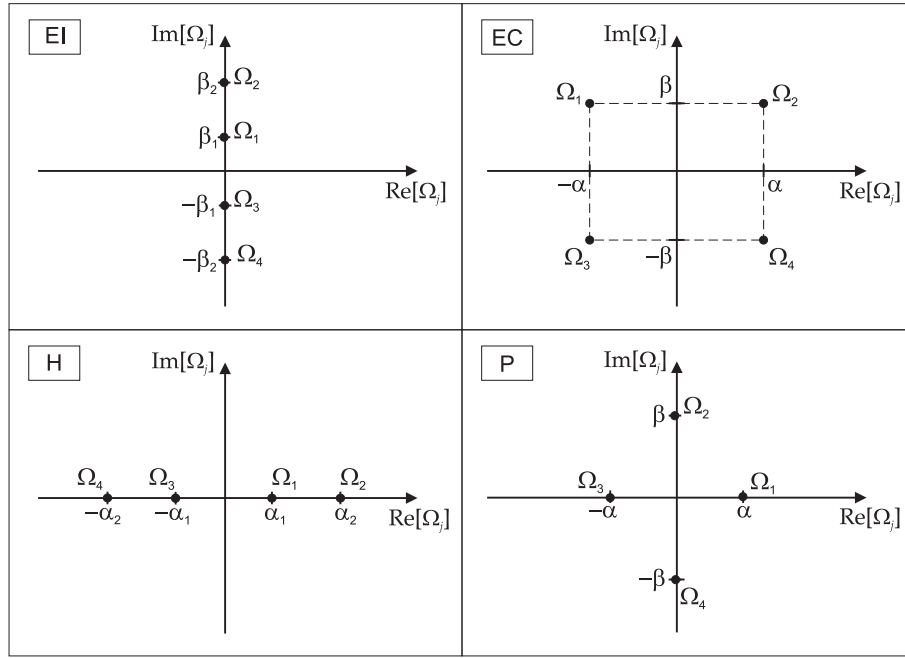


Figure 2.4: Roots  $\Omega_j$  in the complex plane within the different regimes: elliptic imaginary (EI), elliptic complex (EC), hyperbolic (H), and parabolic (P).

## 2.6 Shear band inclinations

The analysis of shear band inclinations can be easily obtained from eqn. (2.25), with the following results.

- Within the hyperbolic regime (H), ellipticity is always lost at (assuming for the moment  $\gamma^{SB} \neq 0$ )

$$\cot^2 \gamma^{SB} = \frac{1 - 2\xi \pm \sqrt{4\xi^2 - 4\xi + k^2}}{1 + k}, \quad (2.51)$$

or equivalently,

$$\tan^2 \gamma^{SB} = \frac{1 - 2\xi \pm \sqrt{4\xi^2 - 4\xi + k^2}}{1 - k}, \quad (2.52)$$

where  $\gamma^{SB}$  is the angle between the shear band normal  $\mathbf{n}$  and the  $x_1$ -axis, see Fig. 2.3. Therefore, within the hyperbolic regime there are *four* shear bands.

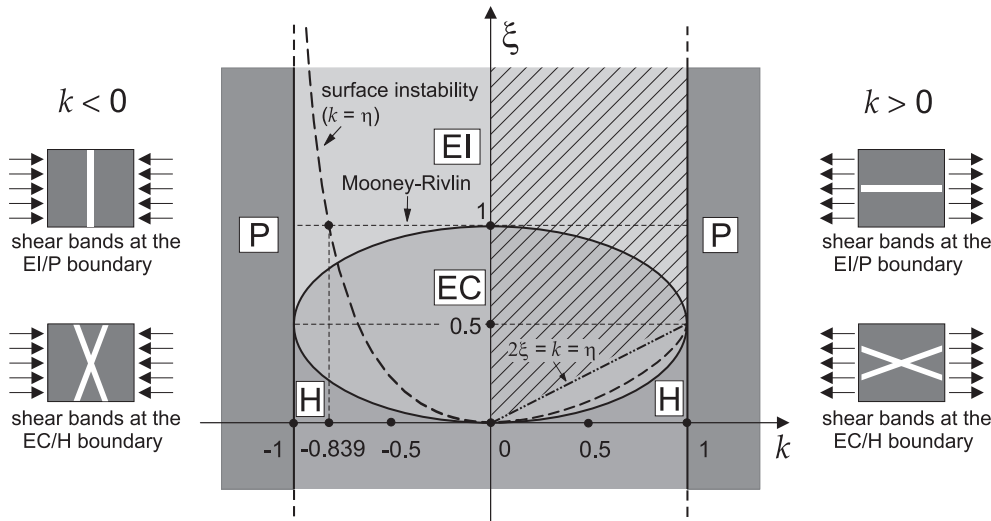


Figure 2.5: Regime classification in the  $k$ - $\xi$  plane. The surface instability condition is also indicated, in the particular case when  $k = \eta = T_1/2$ , corresponding to a uniaxial principal stress aligned parallel to a free surface. In the same case, the exclusion condition (2.20) implies that every bifurcation is excluded in the region bounded by the  $\xi$ -axis and the lines  $\xi = k/2$  and  $k = 1$ .

- At the elliptic complex/hyperbolic boundary (EC/H), the following relation holds true

$$k = \text{sign}(k) 2\sqrt{\xi(1-\xi)}, \quad (2.53)$$

and the shear band inclination formula, eqn. (2.51), gives (Hill and Hutchinson, 1975)

$$\tan^2 \gamma^{SB} = \frac{1 + \text{sign}(k) 2\sqrt{\xi(1-\xi)}}{1 - 2\xi}, \quad (2.54)$$

so that *two* shear bands become possible. For instance, in the special case of  $\xi = 0.25$ , eqn. (2.54) gives an inclination of the band normal  $\gamma^{SB} = \pm 62.632^\circ$  for  $k > 0$  and  $\gamma^{SB} = \pm 27.368^\circ$  for  $k < 0$ , with respect to the direction of the  $x_1$ -axis (note that the band is inclined at  $\pm(\pi/2 - \gamma^{SB})$  with respect to the  $x_1$ -axis). Note that, since  $\xi$  ranges between 0 and 1/2 in EC, for  $k > 0$  ( $k < 0$ ) the shear band is always inclined at an angle ranging between  $45^\circ$  and  $0^\circ$  ( $45^\circ$  and  $90^\circ$ ) with respect to the  $x_1$ -axis, see Fig. 2.6.

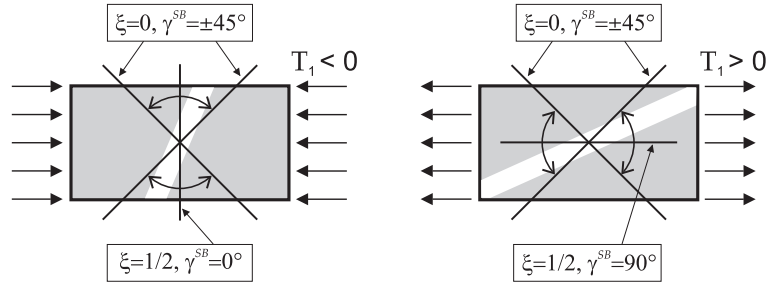


Figure 2.6: Possible shear band inclinations at the EC/H boundary, referred to a uniaxial compressive (tensile) state of stress  $T_1 < 0$  ( $T_1 > 0$ ) on the left (on the right).

- Within the parabolic regime (P), *two* shear bands become possible, which normal is oriented at an angle  $\gamma^{SB}$  solution of

$$\cot^2 \gamma^{SB} = \begin{cases} \frac{1 - 2\xi + \sqrt{4\xi^2 - 4\xi + k^2}}{1 + k}, & \text{if } k > 1, \\ \frac{1 - 2\xi - \sqrt{4\xi^2 - 4\xi + k^2}}{1 + k}, & \text{if } k < -1, \end{cases} \quad (2.55)$$

or equivalently,

$$\tan^2 \gamma^{SB} = \begin{cases} \frac{1 - 2\xi - \sqrt{4\xi^2 - 4\xi + k^2}}{1 - k}, & \text{if } k > 1, \\ \frac{1 - 2\xi + \sqrt{4\xi^2 - 4\xi + k^2}}{1 - k}, & \text{if } k < -1. \end{cases} \quad (2.56)$$

- At the elliptic imaginary/parabolic boundary (EI/P), where

$$k^2 = 1, \quad \text{and} \quad 2\xi > 1, \quad (2.57)$$

we have only *one* shear band possible, aligned parallel to the  $x_1$ -axis, when  $k = 1$ ,

$$\gamma^{SB} = \frac{\pi}{2}, \quad (2.58)$$

or parallel to the  $x_2$ -axis, when  $k = -1$ ,

$$\gamma^{SB} = 0. \quad (2.59)$$

- At the hyperbolic/parabolic boundary (H/P), where

$$k^2 = 1, \quad \text{and} \quad 2\xi < 1, \quad (2.60)$$

*three* shear bands become possible. One is aligned parallel to the  $x_1$ -axis ( $x_2$ -axis), when  $k = 1$  ( $k = -1$ ), while the other two, are the solutions of

$$\tan^2 \gamma^{SB} = \begin{cases} \frac{1}{1 - 2\xi}, & \text{if } k = 1, \\ 1 - 2\xi, & \text{if } k = -1. \end{cases} \quad (2.61)$$

For a Mooney–Rivlin material, eqn. (2.11), loss of ellipticity occurs for infinite value of stretch  $\lambda$  at the EI/P boundary, see eqn. (2.7).

For a  $J_2$ -deformation theory material, loss of ellipticity always occurs at the EC/H boundary, see eqns. (2.41), corresponding to the condition

$$2\xi = 1 - \sqrt{1 - k^2}, \quad (2.62)$$

which, using relations (2.15), yields for the critical logarithmic strain  $\varepsilon^{EL}$  at ellipticity loss

$$N = \varepsilon_1^{EL} \tanh \varepsilon_1^{EL}, \quad (2.63)$$

an equation equivalent to that given by Hutchinson and Tvergaard (1981, their eqn. (3.6)) and showing that the critical logarithmic deformation for ellipticity loss depends only on the hardening exponent  $N$ .

The inclination of the band normal  $\mathbf{n}$  with respect to the  $x_1$ -axis can be deduced by substituting condition (2.63) into (2.15)<sub>1</sub> and the resulting equation into eqn. (2.54), to obtain

$$\gamma^{SB} = \begin{cases} \arctan e^{\varepsilon_1^{EL}}, & \text{if } \varepsilon_1^{EL} > 0, \\ \frac{\pi}{2} - \arctan e^{\varepsilon_1^{EL}}, & \text{if } \varepsilon_1^{EL} < 0, \end{cases} \quad (2.64)$$

where it should be noted that since the inclination of the shear band (see Fig. 2.3) is

$$\vartheta^{SB} = \frac{\pi}{2} - \gamma^{SB}, \quad (2.65)$$

eqn. (2.64) coincides with Hutchinson and Tvergaard (1981, their eqn. (3.7)) and Radi et al. (2002, their eqn. (6.3)).

## 2.7 The situation when shear banding is an initial bifurcation mode

Shear banding is an extreme form of instability, usually occurring after infinite bifurcations are encountered in a loading path. One exception to this rule is when the problem corresponds to the van Hove conditions,<sup>6</sup> generalized by Ryzhak (1993; 1994), in which case shear banding is an initial<sup>7</sup> instability mode.

Other remarkable exceptions occur in the special, but important, case when the Hill (1958; 1959) exclusion condition (2.20) fails simultaneously with ellipticity loss. For instance, considering Fig. 2.5, we note that for uniaxial tension,  $\eta = k$ , the exclusion condition (2.20) implies that any bifurcation is excluded for positive  $k$  in the elliptic regime and values of  $\xi$  higher than the line  $\xi = k/2$  (drawn dashed in Fig. 2.5). Therefore, as noted by Hill and Hutchinson (1975, their appendix AII) for  $\xi \geq 0.5$  and  $k = \eta > 0$ , diffuse bifurcation modes are excluded in the elliptic regime for an elastic material (2.3) subject to uniaxial tension, so that shear bands occurs as a first instability.

More in general, taking  $\eta = tk$ , the Hill exclusion condition is satisfied within the region in the  $k$ - $\xi$  plane bounded by the vertical  $\xi$ -axis, by the inclined line  $\xi = tk/2$ , and by the vertical line at  $k = 2t/(1 + t^2)$ . These two lines intersect at the point of coordinates  $[k = 2t/(1 + t^2); \xi = t^2/(1 + t^2)]$ , see Fig. 2.7, which lies on the EC/H boundary for  $t < 1$  or on the EC/EI boundary for  $t > 1$ .

For a deformation path in the  $k$ - $\xi$  plane terminating at the intersection point between the two above lines, *shear bands are an initial bifurcation mode, so that diffuse modes do not occur previously.*

Situations where shear banding are an initial bifurcation mode have been analyzed in elastoplasticity by Bigoni and Hueckel (1991).

---

<sup>6</sup>van Hove (1947) shown that for a homogeneous and homogeneously deformed body, characterized by an incrementally linear constitutive operator (in our context  $\mathbb{G}$ ) and subject to prescribed velocity over the entire boundary, the strong ellipticity condition (2.22) for every unit vector  $\mathbf{n}$  and non-zero vector  $\mathbf{g}$ , implies that the velocity problem has at most one solution.

<sup>7</sup>We write ‘an initial’ and not ‘the initial’, since there can be contemporaneity of shear banding with other instability modes.



where  $\varepsilon_1^{sur}$  is the logarithmic strain parallel to the free surface and showing that it depends only on the hardening parameter  $N$ .

Eqn. (2.68) can be numerically solved, thus obtaining results reported in Table 2.1, where also the critical logarithmic strain for ellipticity loss  $\varepsilon_1^{EL}$ , eqn. (2.63), and the shear band inclination  $\vartheta^{SB}$  (in degrees, calculated from eqn. (2.64) providing the inclination of the band normal) with respect to the  $x_1$ -axis for positive strain are reported (note that the absolute value for loss of ellipticity remains the same for positive and negative logarithmic strain, while the band inclination changes is at  $\pi/2$  minus the value for positive  $\varepsilon_1^{EL}$ ).

Note that the critical logarithmic strain  $\varepsilon_1^{PD}$  for the Hill exclusion condition (2.20) to hold is (2.21), namely,  $\varepsilon_1^{PD} = 0$  (so that bifurcation is never excluded in compression) and  $\varepsilon_1^{PD} = N$  (so that bifurcation is excluded in tension for sufficiently small strain).

Table 2.1: Critical logarithmic strains for surface bifurcation  $\varepsilon_1^{sur}$  and for ellipticity loss  $\varepsilon_1^{EL}$  in a  $J_2$ -deformation theory material prestressed for uniaxial tension (positive sign) and compression (negative sign) parallel to the free surface (orthogonal to the  $x_2$ -axis) as a function of the hardening parameter  $N$ .

N	$\varepsilon_1^{EL}$	uniaxial tension		uniaxial compression	
		$\varepsilon_1^{sur}$	$\vartheta^{SB}$	$\varepsilon_1^{sur}$	$\vartheta^{SB}$
0.1	$\pm 0.322$	0.252	$\pm 35.94^\circ$	-0.201	$\pm 54.06^\circ$
0.2	$\pm 0.463$	0.377	$\pm 32.19^\circ$	-0.274	$\pm 57.81^\circ$
0.3	$\pm 0.577$	0.484	$\pm 29.33^\circ$	-0.326	$\pm 60.67^\circ$
0.4	$\pm 0.678$	0.582	$\pm 26.92^\circ$	-0.368	$\pm 63.08^\circ$
0.5	$\pm 0.772$	0.675	$\pm 24.81^\circ$	-0.403	$\pm 65.19^\circ$
0.6	$\pm 0.861$	0.766	$\pm 22.91^\circ$	-0.434	$\pm 67.09^\circ$
0.7	$\pm 0.948$	0.855	$\pm 21.19^\circ$	-0.461	$\pm 68.81^\circ$
0.8	$\pm 1.032$	0.943	$\pm 19.60^\circ$	-0.486	$\pm 70.40^\circ$
0.9	$\pm 1.116$	1.031	$\pm 18.13^\circ$	-0.509	$\pm 71.87^\circ$

It can be concluded from Table 2.1 that for a uniaxial state of stress of a  $J_2$ -deformation theory of plasticity, loss of ellipticity always occurs after surface bifurcation.

More in general than for the  $J_2$ -deformation theory of plasticity, eqn. (2.67), valid for  $k = \eta$ , is plotted dashed in Fig. 2.5, while the more general

condition (2.66) is reported dashed in Fig. 2.8. From these figures we can observe that

*surface instability is always possible (in EC and EI, at an appropriate prestress level) for compressive and tensile stresses parallel to the free surface, with one exception. This is the case of a state of uniaxial tensile prestress aligned parallel to the surface,  $k = \eta > 0$ , where surface instability can only occur in EC, while at the EI/P boundary surface instability degenerates into a shear band mode.*

Surface bifurcation, eqn. (2.66), and the Hill exclusion condition, eqn. (2.20), are reported in Figs. 2.5 and 2.8 for different values of  $\eta/k$ .

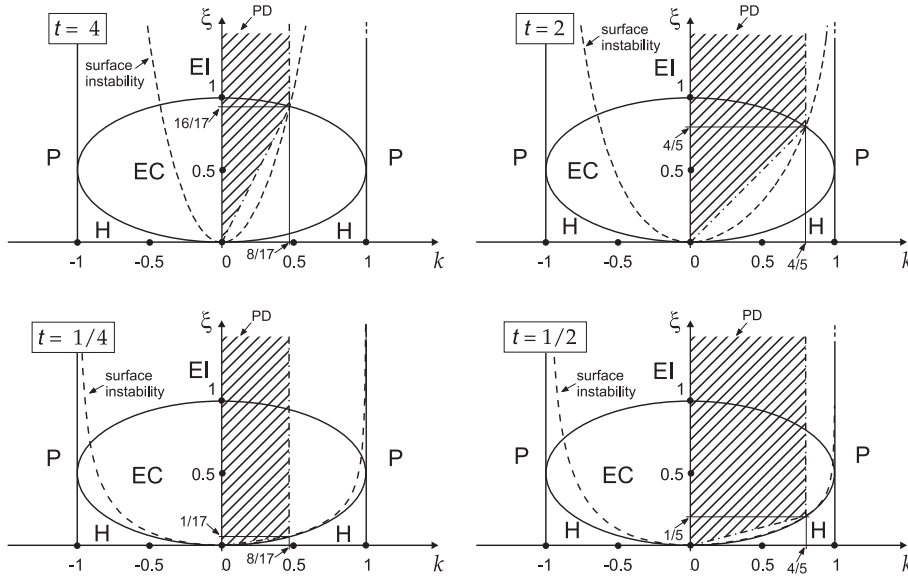


Figure 2.8: Surface bifurcation, eqn. (2.66), and the Hill exclusion condition, eqn. (2.20), for  $\eta = tk$  with  $t = \{4, 2, 1/4, 1/2\}$  in the  $k-\xi$  plane, reported with the regime classification.

## Chapter 3

---

### Crack in a prestressed material

*The full-field solution for a finite-length crack in a prestressed material incrementally loaded under mode I and mode II is provided. This solution is new in the case when the crack is inclined with respect to the material orthotropic axes and is fundamental to the understanding of the shear band problem treated in Chapter 5. Although based on the assumption that dead loading tractions are present inside the crack to equilibrate the assumed prestress state, this solution is interesting in itself since, when used near the boundary of ellipticity loss, it reveals features related to the interaction between shear bands and crack tip fields, so that it may explain experimental observations relative to crack growth in ductile materials.*

A homogeneously prestressed (or prestrained), incompressible elastic infinite plane is considered, characterized by the constitutive equations (2.6) of incremental, incompressible, orthotropic elasticity, containing a crack of current length  $2l$ , taken parallel to the  $\hat{x}_1$ -axis in the  $\hat{x}_1$ - $\hat{x}_2$  reference system, and loaded at infinity by a uniform nominal stress increment  $\hat{t}_{2n}^\infty$ , where  $n = 1$  corresponds to Mode II and  $n = 2$  to Mode I loading (Fig. 3.1). Obviously, the crack faces cannot be free of tractions, since a dead loading is required to ‘provide’ the prestress state (with principal Cauchy components  $T_1$  and  $T_2$ , assumed aligned parallel to the  $x_1$ - $x_2$  reference system, rotated at an angle  $\vartheta_0$  with respect to the  $\hat{x}_1$ - $\hat{x}_2$  system). An interesting exception to this rule occurs when the crack is aligned parallel to the  $x_1$ -axis and the prestress is aligned parallel to the crack surfaces, namely, when the  $\hat{x}_1$ - $\hat{x}_2$  and  $x_1$ - $x_2$  systems coincide, i.e.  $\vartheta_0 = 0$ , and  $T_2 = 0$ , corresponding to  $\eta = k$ . This situation has

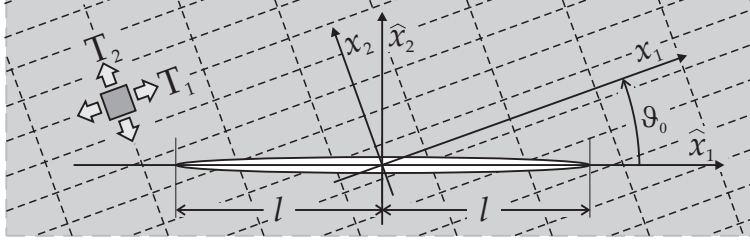


Figure 3.1: Crack of length  $2l$  in a prestressed, orthotropic material inclined at an angle  $\vartheta_0$  (positive when anticlockwise) with respect to the orthotropy axes  $x_1$  and  $x_2$ .  $T_1$  and  $T_2$  denote the prestress state, expressed through the two in-plane principal Cauchy stresses aligned parallel to the  $x_1$ - $x_2$  reference system.

been considered by Guz (1999, and references quoted therein), Cristescu et al. (2004) and Radi et al. (2002, in the near-tip asymptotic limit). The case of a generic inclination  $\vartheta_0$ , has never been treated in the case of a prestressed material, but it is well-known in linear, infinitesimal, anisotropic elasticity (Savin, 1961; see also Sih and Liebowitz, 1968). Although the assumption of an inclined crack in a prestressed material may seem rather artificial, the treatment will provide the key for the modelling of a shear band formation and its propagation conditions in §5.

Solution to the above-formulated crack problem is obtained by superimposing the trivial, unperturbed solution to the perturbation induced by the crack, the latter denoted with the apex  $\circ$ .

The unperturbed solutions are obtained defining the uniform nominal stress field in the  $\hat{x}_1$ - $\hat{x}_2$  reference system

$$\hat{t}_{22} = \hat{t}_{22}^\infty, \quad \hat{t}_{11} = 0, \quad \hat{t}_{12} = \hat{t}_{21} = \hat{t}_{21}^\infty, \quad (3.1)$$

so that  $\hat{t}_{21}^\infty = 0$  ( $\hat{t}_{22}^\infty = 0$ ) for Mode I (Mode II). The stress components in the  $\hat{x}_1$ - $\hat{x}_2$  reference system can be obtained through a rotation of the components in the prestress principal reference system  $x_1$ - $x_2$ , so that, since the two systems are rotated at an angle  $\vartheta_0$  (taken positive when anticlockwise), we have

$$\hat{\mathbf{x}} = \mathbf{Q}^T \mathbf{x}, \quad [\mathbf{Q}] = \begin{bmatrix} \cos \vartheta_0 & \sin \vartheta_0 \\ -\sin \vartheta_0 & \cos \vartheta_0 \end{bmatrix}, \quad (3.2)$$

so that the nominal stress increment, incremental displacement and its gradient can be expressed in the  $\hat{x}_1$ - $\hat{x}_2$  reference system as

$$\hat{\mathbf{t}} = \mathbf{Q}^T \mathbf{t} \mathbf{Q}, \quad \hat{\mathbf{v}} = \mathbf{Q}^T \mathbf{v}, \quad \hat{\nabla} \hat{\mathbf{v}} = \mathbf{Q}^T \nabla \mathbf{v} \mathbf{Q}, \quad (3.3)$$

while the constitutive equations (2.2) transform to

$$\hat{\mathbf{t}} = \hat{\mathbb{G}}[\hat{\nabla}\hat{\mathbf{v}}^T] + \dot{p}\mathbf{I}, \quad (3.4)$$

where the components of the transformed fourth-order tensor  $\hat{\mathbb{G}}$  are given by

$$\hat{\mathbb{G}}_{ijkl} = Q_{mi}Q_{nj}\mathbb{G}_{mnop}Q_{ok}Q_{pl}. \quad (3.5)$$

Note that the above definition (3.1) of Mode I and II loadings is fully meaningful only when the constitutive equations (2.6) are positive defined, so that the Hill exclusion condition (2.20) holds true. For a non-positive definite constitutive equation, definition (3.1) would be better changed to one concerning the components of the incremental displacement gradient.

Assuming that condition (2.20) holds true, we can directly obtain from eqns. (2.6) the components of the incremental displacement gradient and the incremental in-plane mean stress in the  $x_1$ - $x_2$  reference system

$$\begin{aligned} \dot{p} &= \frac{\hat{t}_{22}^\infty}{2} - \mu k v_{2,2}, \\ v_{2,2} = -v_{1,1} &= \frac{\hat{t}_{22}^\infty \cos 2\vartheta_0 - 2\hat{t}_{21}^\infty \sin 2\vartheta_0}{2\mu(2\xi - \eta)}, \\ v_{1,2} &= -\frac{(k + \eta)(\hat{t}_{22}^\infty \sin 2\vartheta_0 + 2\hat{t}_{21}^\infty \cos 2\vartheta_0)}{2\mu(k^2 - 2\eta + \eta^2)}, \\ v_{2,1} &= \frac{(k - \eta)(\hat{t}_{22}^\infty \sin 2\vartheta_0 + 2\hat{t}_{21}^\infty \cos 2\vartheta_0)}{2\mu(k^2 - 2\eta + \eta^2)}. \end{aligned} \quad (3.6)$$

The components of the incremental displacement gradient in the  $\hat{x}_1$ - $\hat{x}_2$  reference system can be obtained through a rotation of eqns. (3.6), by employing eqn. (3.3)<sub>3</sub>.

It should be noticed from eqns. (3.6) that in the absence of prestress,  $k = \eta = 0$ , eqns. (3.6) fully determine the incremental displacement gradient. In this case, however, the incremental stress is only related to the symmetric part of the incremental displacement gradient, so that an arbitrary incremental rotation can be added without altering the state of stress, a circumstance not possible when the prestress is different from zero. In other words, when the prestress is present, loading (3.1) completely defines the incremental displacement gradient (and incremental mean stress) through eqns. (3.6), so that incremental rigid body rotations remains determined.

Finally, null incremental normal and shearing nominal tractions are prescribed along the crack surface,

$$\hat{t}_{22}(\hat{x}_1, 0^\pm) = \hat{t}_{21}(\hat{x}_1, 0^\pm) = 0, \quad \forall |\hat{x}_1| < l, \quad (3.7)$$

where apices + and – denote the upper and lower crack surface, respectively.

### 3.1 Crack parallel to an orthotropy axis

Before to proceed with the solution of the inclined crack, it becomes instructive to begin with the simple case of null inclination, in which  $\vartheta_0 = 0$ , so that the prestress  $x_1$ – $x_2$  axes are coincident with the  $\hat{x}_1$ – $\hat{x}_2$  axes.

The perturbed solution is derived separately for the two EI and EC regimes (beginning with EI).

From representation (2.32), the stream function  $\psi^\circ$ , eqn. (2.30), can be given in the form

$$\psi^\circ(z_1, z_2) = \text{Re} \left[ \sum_{j=1}^2 F_j(z_j) \right], \quad (3.8)$$

(note that the summation ranges between 1 and 2, since the  $\Omega_j$ 's are in conjugated pairs in E) where  $z_j = x_1 + \Omega_j x_2$ , and with  $\Omega_j$  given by eqn. (2.34), so that the displacement field becomes

$$v_1^\circ(z_1, z_2) = \text{Re} \left[ \sum_{j=1}^2 \Omega_j F_j'(z_j) \right], \quad v_2^\circ(z_1, z_2) = -\text{Re} \left[ \sum_{j=1}^2 F_j'(z_j) \right], \quad (3.9)$$

and its gradient can be written as

$$\begin{aligned} v_{1,1}^\circ(z_1, z_2) &= -v_{2,2}^\circ(z_1, z_2) = \text{Re} \left[ \sum_{j=1}^2 \Omega_j F_j''(z_j) \right], \\ v_{1,2}^\circ(z_1, z_2) &= \text{Re} \left[ \sum_{j=1}^2 \Omega_j^2 F_j''(z_j) \right], \quad v_{2,1}^\circ(z_1, z_2) = -\text{Re} \left[ \sum_{j=1}^2 F_j''(z_j) \right]. \end{aligned} \quad (3.10)$$

The effects of the applied boundary conditions on the crack surfaces decay to zero at infinity, so that, from eqns. (3.10) and the constitutive relation (2.6) we obtain

$$\lim_{|z_j| \rightarrow +\infty} F_j''(z_j) = 0, \quad j = 1, 2. \quad (3.11)$$

### 3.1.1 Mode I

To recover traction-free crack faces using superposition, the incremental nominal stress component  $t_{22}^\infty$  of reversed sign has to be prescribed at crack surfaces in the perturbed problem, namely, for Mode I

$$\begin{aligned} t_{22}^\circ(x_1, 0^\pm) &= -t_{22}^\infty & \forall |x_1| < l, \\ t_{21}^\circ(x_1, 0^\pm) &= 0, & \forall x_1 \in \mathbb{R}. \end{aligned} \quad (3.12)$$

From eqns. (3.12)<sub>2</sub> and (3.10) the following relation can be obtained, holding at every point  $x_1$  of the real axis  $\mathbb{R}$

$$F_2''(x_1) = -\frac{2\xi - \eta + \Lambda}{2\xi - \eta - \Lambda} F_1''(x_1), \quad (3.13)$$

where

$$\Lambda = \sqrt{4\xi^2 - 4\xi + k^2}, \quad (3.14)$$

while from eqn. (3.12)<sub>1</sub> the condition

$$\begin{aligned} \frac{t_{22}^\infty}{\mu} &= \operatorname{Re} \left\{ \Omega_1 [4\xi - 1 - \eta + \Omega_1^2(1 - k)] F_1''(x_1) \right. \\ &\quad \left. + \Omega_2 [4\xi - 1 - \eta + \Omega_2^2(1 - k)] F_2''(x_1) \right\}, \end{aligned} \quad (3.15)$$

follows, to hold true along the crack line  $|x_1| < l$ .

#### Elliptic imaginary regime

Within the EI regime, eqns. (2.38), and for Mode I, the Riemann-Hilbert problem:

$$-\frac{\beta_2 \varepsilon_1^2 - \beta_1 \varepsilon_2^2}{\varepsilon_2} \operatorname{Re} [i F_1''(x_1)] = \frac{t_{22}^\infty}{\mu}, \quad \forall |x_1| < l, \quad (3.16)$$

where  $\beta_1$  and  $\beta_2$  are defined by eqn. (2.40) and

$$\varepsilon_n = 1 - \eta + (1 - k)\beta_n^2, \quad n = 1, 2, \quad (3.17)$$

has the following solution

$$F_j''(z_j) = (-1)^k i \frac{t_{22}^\infty}{\mu} \frac{\varepsilon_k}{\beta_2 \varepsilon_1^2 - \beta_1 \varepsilon_2^2} \left( 1 - \frac{z_j}{\sqrt{z_j^2 - l^2}} \right), \quad j, k = 1, 2, \quad j \neq k, \quad (3.18)$$

where the function  $\sqrt{z_j^2 - l^2}$  is defined to have a unique branch cut ( $x_1 < |l|$ ,  $x_2 = 0$ ), chosen<sup>1</sup> in such a way that  $\sqrt{z_j^2 - l^2} = \sqrt{x_1^2 - l^2}$ , for  $x_1 > l$  and  $x_2 = 0$ .

The perturbed stream function becomes

$$\psi^\circ = -\frac{t_{22}^\infty}{2\mu} \frac{\varepsilon_2}{\beta_2\varepsilon_1^2 - \beta_1\varepsilon_2^2} \sum_{j=1}^2 \left(-\frac{\varepsilon_1}{\varepsilon_2}\right)^{j-1} \operatorname{Im} \left[ z_j^2 - z_j \sqrt{z_j^2 - l^2} + l^2 \ln \left( z_j + \sqrt{z_j^2 - l^2} \right) \right], \quad (3.19)$$

and the incremental displacements take the form

$$\begin{aligned} v_1^\circ &= -\frac{t_{22}^\infty}{\mu} \frac{\varepsilon_2}{\beta_2\varepsilon_1^2 - \beta_1\varepsilon_2^2} \operatorname{Re} \left[ \beta_1 \left( z_1 - \sqrt{z_1^2 - l^2} \right) - \frac{\beta_2\varepsilon_1}{\varepsilon_2} \left( z_2 - \sqrt{z_2^2 - l^2} \right) \right], \\ v_2^\circ &= \frac{t_{22}^\infty}{\mu} \frac{\varepsilon_2}{\beta_2\varepsilon_1^2 - \beta_1\varepsilon_2^2} \operatorname{Im} \left[ \left( z_1 - \sqrt{z_1^2 - l^2} \right) - \frac{\varepsilon_1}{\varepsilon_2} \left( z_2 - \sqrt{z_2^2 - l^2} \right) \right]. \end{aligned} \quad (3.20)$$

Finally, for Mode I in the EI regime, the incremental in-plane mean stress is given by

$$\dot{p}^\circ = \frac{t_{22}^\infty \varepsilon_2}{\beta_2\varepsilon_1^2 - \beta_1\varepsilon_2^2} \left\{ \frac{\varepsilon_2\beta_1\delta_1 - \varepsilon_1\beta_2\delta_2}{\varepsilon_2} - \operatorname{Re} \left[ \beta_1\delta_1 \frac{z_1}{\sqrt{z_1^2 - l^2}} - \frac{\varepsilon_1\beta_2\delta_2}{\varepsilon_2} \frac{z_2}{\sqrt{z_2^2 - l^2}} \right] \right\}, \quad (3.21)$$

where

$$\delta_n = 2\xi - 1 - k - (1 - k)\beta_n^2, \quad n = 1, 2, \quad (3.22)$$

---

<sup>1</sup>Note that function  $\sqrt{z_j^2 - l^2}$  has been taken equal to  $\sqrt{z_j - l}\sqrt{z_j + l}$ , with the usual branch cut definition for the latter square root functions. Therefore, on the real axis

$$x_2 = 0, \quad \sqrt{z_j^2 - l^2} = \pm \sqrt{x_1^2 - l^2},$$

with the upper (lower) sign for  $x_1 > l$  ( $x_1 < -l$ ), while along the branch cut when  $\operatorname{Im}[\Omega_j] > 0$ ,

$$-l < x_1 < l \quad \sqrt{z_j^2 - l^2} = \pm i \sqrt{l^2 - x_1^2},$$

with the upper (lower) sign for  $x_2 = 0^+$  ( $x_2 = 0^-$ ).

while the incremental nominal stress components are

$$\begin{aligned}
t_{11}^{\circ} &= -i_{22}^{\infty} \frac{\varepsilon_1 \varepsilon_2}{\beta_2 \varepsilon_1^2 - \beta_1 \varepsilon_2^2} \left\{ \beta_1 - \beta_2 - \operatorname{Re} \left[ \beta_1 \frac{z_1}{\sqrt{z_1^2 - l^2}} - \beta_2 \frac{z_2}{\sqrt{z_2^2 - l^2}} \right] \right\}, \\
t_{22}^{\circ} &= -i_{22}^{\infty} \left\{ 1 + \frac{\varepsilon_2}{\beta_2 \varepsilon_1^2 - \beta_1 \varepsilon_2^2} \operatorname{Re} \left[ \beta_1 \varepsilon_2 \frac{z_1}{\sqrt{z_1^2 - l^2}} - \frac{\varepsilon_1^2 \beta_2}{\varepsilon_2} \frac{z_2}{\sqrt{z_2^2 - l^2}} \right] \right\}, \\
t_{12}^{\circ} &= -i_{22}^{\infty} \frac{\varepsilon_2}{\beta_2 \varepsilon_1^2 - \beta_1 \varepsilon_2^2} \operatorname{Im} \left[ \beta_1^2 \varepsilon_2 \frac{z_1}{\sqrt{z_1^2 - l^2}} - \frac{\varepsilon_1^2 \beta_2^2}{\varepsilon_2} \frac{z_2}{\sqrt{z_2^2 - l^2}} \right], \\
t_{21}^{\circ} &= -i_{22}^{\infty} \frac{\varepsilon_1 \varepsilon_2}{\beta_2 \varepsilon_1^2 - \beta_1 \varepsilon_2^2} \operatorname{Im} \left[ \frac{z_1}{\sqrt{z_1^2 - l^2}} - \frac{z_2}{\sqrt{z_2^2 - l^2}} \right].
\end{aligned} \tag{3.23}$$

### Elliptic complex regime

Within the EC regime, eqns. (2.41), and for Mode I, the Riemann-Hilbert problem:

$$2 [\alpha(\delta^2 - \chi^2) + 2\beta\delta\chi] \operatorname{Re} \left[ \frac{F_1''(x_1)}{\chi - i\delta} \right] = \frac{i_{22}^{\infty}}{\mu}, \quad \forall |x_1| < l, \tag{3.24}$$

where  $\alpha$  and  $\beta$  are defined by eqn. (2.43) and

$$\chi = 2\xi - \eta, \quad \delta = 2(1 - k)\alpha\beta = \sqrt{4\xi - 4\xi^2 - k^2}, \tag{3.25}$$

has the following solution:

$$F_j''(z_j) = (-1)^k \frac{i_{22}^{\infty}}{2\mu} \frac{\chi + (-1)^j i\delta}{\alpha(\delta^2 - \chi^2) + 2\beta\delta\chi} \left( 1 - \frac{z_j}{\sqrt{z_j^2 - l^2}} \right), \quad j, k = 1, 2, \quad j \neq k, \tag{3.26}$$

where function  $\sqrt{z_j^2 - l^2}$  has been defined as in eqn. (3.18). Note from eqns. (2.40) and (2.43) that  $z_j = x_1 + i\beta_j x_2$ , with  $\beta_j > 0$  in EI, and  $z_j = x_1 + (-1)^j \alpha x_2 + i\beta x_2$ , with  $\beta > 0$  in EC, so that, for both regimes,  $\operatorname{Im}[z_j] = 0 \iff x_2 = 0$ .

The perturbed stream function becomes

$$\begin{aligned} \psi^\circ &= -\frac{i_{22}^\infty}{4\mu[\alpha(\delta^2 - \chi^2) + 2\beta\delta\chi]} \sum_{j=1}^2 \operatorname{Re} \left\{ [(-1)^j \chi + i\delta] \right. \\ &\quad \left. \times \left[ z_j^2 - z_j \sqrt{z_j^2 - l^2} + l^2 \ln \left( z_j + \sqrt{z_j^2 - l^2} \right) \right] \right\}, \end{aligned} \quad (3.27)$$

and the incremental displacements take the form

$$\begin{aligned} v_1^\circ &= -\frac{i_{22}^\infty}{2\mu \alpha(\delta^2 - \chi^2) + 2\beta\delta\chi} \left\{ (\alpha\chi - \beta\delta) \operatorname{Re} \left[ \left( z_1 - \sqrt{z_1^2 - l^2} \right) + \left( z_2 - \sqrt{z_2^2 - l^2} \right) \right] \right. \\ &\quad \left. + (\alpha\delta + \beta\chi) \operatorname{Im} \left[ \left( z_1 - \sqrt{z_1^2 - l^2} \right) - \left( z_2 - \sqrt{z_2^2 - l^2} \right) \right] \right\}, \\ v_2^\circ &= -\frac{i_{22}^\infty}{2\mu \alpha(\delta^2 - \chi^2) + 2\beta\delta\chi} \left\{ \chi \operatorname{Re} \left[ \left( z_1 - \sqrt{z_1^2 - l^2} \right) - \left( z_2 - \sqrt{z_2^2 - l^2} \right) \right] \right. \\ &\quad \left. + \delta \operatorname{Im} \left[ \left( z_1 - \sqrt{z_1^2 - l^2} \right) + \left( z_2 - \sqrt{z_2^2 - l^2} \right) \right] \right\}. \end{aligned} \quad (3.28)$$

Finally, for Mode I in the EC regime, the incremental in-plane mean stress is given by

$$\begin{aligned} \dot{p}^\circ &= -\frac{i_{22}^\infty}{2} \frac{1}{\alpha(\delta^2 - \chi^2) + 2\beta\delta\chi} \\ &\quad \times \left\{ [(\beta\chi + \alpha\delta)\delta + (\alpha\chi - \beta\delta)k] \left( 2 - \operatorname{Re} \left[ \frac{z_1}{\sqrt{z_1^2 - l^2}} + \frac{z_2}{\sqrt{z_2^2 - l^2}} \right] \right) \right. \\ &\quad \left. - [(\beta\chi + \alpha\delta)k - (\alpha\chi - \beta\delta)\delta] \operatorname{Im} \left[ \frac{z_1}{\sqrt{z_1^2 - l^2}} - \frac{z_2}{\sqrt{z_2^2 - l^2}} \right] \right\}, \end{aligned} \quad (3.29)$$

while the incremental nominal stress components are

$$\begin{aligned} \dot{t}_{11}^\circ &= -\frac{i_{22}^\infty}{2} \frac{\delta^2 + \chi^2}{\alpha(\delta^2 - \chi^2) + 2\beta\delta\chi} \left\{ 2\alpha - \alpha \operatorname{Re} \left[ \frac{z_1}{\sqrt{z_1^2 - l^2}} + \frac{z_2}{\sqrt{z_2^2 - l^2}} \right] \right. \\ &\quad \left. - \beta \operatorname{Im} \left[ \frac{z_1}{\sqrt{z_1^2 - l^2}} - \frac{z_2}{\sqrt{z_2^2 - l^2}} \right] \right\}, \end{aligned} \quad (3.30)$$

$$\begin{aligned}
t_{22}^{\circ} &= -\frac{i_{22}^{\infty}}{2} \left\{ 2 - \operatorname{Re} \left[ \frac{z_1}{\sqrt{z_1^2 - l^2}} + \frac{z_2}{\sqrt{z_2^2 - l^2}} \right] \right. \\
&\quad \left. - \frac{\beta(\delta^2 - \chi^2) - 2\alpha\delta\chi}{\alpha(\delta^2 - \chi^2) + 2\beta\delta\chi} \operatorname{Im} \left[ \frac{z_1}{\sqrt{z_1^2 - l^2}} - \frac{z_2}{\sqrt{z_2^2 - l^2}} \right] \right\}, \\
t_{12}^{\circ} &= \frac{i_{22}^{\infty}}{2} \left\{ \frac{(\alpha^2 - \beta^2)(\delta^2 - \chi^2) + 4\alpha\beta\delta\chi}{\alpha(\delta^2 - \chi^2) + 2\beta\delta\chi} \operatorname{Re} \left[ \frac{z_1}{\sqrt{z_1^2 - l^2}} - \frac{z_2}{\sqrt{z_2^2 - l^2}} \right] \right. \\
&\quad \left. + \frac{2\alpha\beta(\delta^2 - \chi^2) - 2\delta\chi(\alpha^2 - \beta^2)}{\alpha(\delta^2 - \chi^2) + 2\beta\delta\chi} \operatorname{Im} \left[ \frac{z_1}{\sqrt{z_1^2 - l^2}} + \frac{z_2}{\sqrt{z_2^2 - l^2}} \right] \right\}, \\
t_{21}^{\circ} &= \frac{i_{22}^{\infty}}{2} \frac{\delta^2 + \chi^2}{\alpha(\delta^2 - \chi^2) + 2\beta\delta\chi} \operatorname{Re} \left[ \frac{z_1}{\sqrt{z_1^2 - l^2}} - \frac{z_2}{\sqrt{z_2^2 - l^2}} \right].
\end{aligned}$$

### 3.1.2 Mode II

The reverse of the incremental nominal stress component  $t_{21}^{\circ}$  has to be applied at the crack surfaces in the perturbed Mode II solution, namely,

$$\begin{aligned}
t_{22}^{\circ}(x_1, 0^{\pm}) &= 0, & \forall x_1 \in \mathbb{R}, \\
t_{21}^{\circ}(x_1, 0^{\pm}) &= -t_{21}^{\circ}, & \forall |x_1| < l.
\end{aligned} \tag{3.31}$$

Eqns. (3.31)<sub>1</sub>, (3.9)<sub>4</sub> and eqn. (3.31)<sub>2</sub> provide the following two conditions,

$$F_2''(x_1) = -\frac{\Omega_1}{\Omega_2} \frac{2\xi - \eta - \Lambda}{2\xi - \eta + \Lambda} F_1''(x_1), \tag{3.32}$$

holding at every point  $x_1$  of the real axis  $\mathbb{R}$ , where  $\Lambda$  is defined by eqn. (3.14), and

$$\frac{t_{21}^{\circ}}{\mu} = \operatorname{Re} \left\{ [1 - \eta - \Omega_1^2(1 - k)] F_1''(x_1) + [1 - \eta - \Omega_2^2(1 - k)] F_2''(x_1) \right\}, \tag{3.33}$$

holding for  $|x_1| < l$ .

### Elliptic imaginary regime

Within the EI regime, eqns. (2.38), and for Mode II, the Riemann-Hilbert problem:

$$\frac{\beta_2 \varepsilon_1^2 - \beta_1 \varepsilon_2^2}{\beta_2 \varepsilon_1} \operatorname{Re} [F_1''(x_1)] = \frac{i_{21}^\infty}{\mu}, \quad \forall |x_1| < l, \quad (3.34)$$

has the following solution:

$$F_j''(z_j) = (-1)^k \frac{i_{21}^\infty}{\mu} \frac{\beta_k \varepsilon_j}{\beta_2 \varepsilon_1^2 - \beta_1 \varepsilon_2^2} \left( 1 - \frac{z_j}{\sqrt{z_j^2 - l^2}} \right), \quad j, k = 1, 2, \quad j \neq k, \quad (3.35)$$

so that the perturbed stream function becomes

$$\psi^\circ = \frac{i_{21}^\infty}{2\mu} \frac{\beta_2 \varepsilon_1}{\beta_2 \varepsilon_1^2 - \beta_1 \varepsilon_2^2} \sum_{j=1}^2 \left( -\frac{\varepsilon_2 \beta_1}{\varepsilon_1 \beta_2} \right)^{j-1} \operatorname{Re} \left[ z_j^2 - z_j \sqrt{z_j^2 - l^2} + l^2 \ln \left( z_j + \sqrt{z_j^2 - l^2} \right) \right], \quad (3.36)$$

and the incremental displacements take the form

$$v_1^\circ = -\frac{i_{21}^\infty}{\mu} \frac{\beta_1 \beta_2 \varepsilon_1}{\beta_2 \varepsilon_1^2 - \beta_1 \varepsilon_2^2} \operatorname{Im} \left[ \left( z_1 - \sqrt{z_1^2 - l^2} \right) - \frac{\varepsilon_2}{\varepsilon_1} \left( z_2 - \sqrt{z_2^2 - l^2} \right) \right],$$

$$v_2^\circ = -\frac{i_{21}^\infty}{\mu} \frac{\beta_2 \varepsilon_1}{\beta_2 \varepsilon_1^2 - \beta_1 \varepsilon_2^2} \operatorname{Re} \left[ \left( z_1 - \sqrt{z_1^2 - l^2} \right) - \frac{\beta_1 \varepsilon_2}{\beta_2 \varepsilon_1} \left( z_2 - \sqrt{z_2^2 - l^2} \right) \right]. \quad (3.37)$$

Finally, for Mode II in the EI regime, the incremental in-plane mean stress and the incremental nominal stress components are given by

$$\dot{p}^\circ = -i_{21}^\infty \frac{\beta_1 \beta_2 \varepsilon_1}{\beta_2 \varepsilon_1^2 - \beta_1 \varepsilon_2^2} \operatorname{Im} \left[ \delta_1 \frac{z_1}{\sqrt{z_1^2 - l^2}} - \frac{\varepsilon_2 \delta_2}{\varepsilon_1} \frac{z_2}{\sqrt{z_2^2 - l^2}} \right], \quad (3.38)$$

$$i_{11}^\circ = i_{21}^\infty \frac{\beta_1 \beta_2 \varepsilon_1}{\beta_2 \varepsilon_1^2 - \beta_1 \varepsilon_2^2} \operatorname{Im} \left[ \varepsilon_1 \frac{z_1}{\sqrt{z_1^2 - l^2}} - \frac{\varepsilon_2^2}{\varepsilon_1} \frac{z_2}{\sqrt{z_2^2 - l^2}} \right],$$

$$\begin{aligned}
t_{22}^{\circ} &= -i_{21}^{\infty} \frac{\beta_1 \beta_2 \varepsilon_1 \varepsilon_2}{\beta_2 \varepsilon_1^2 - \beta_1 \varepsilon_2^2} \operatorname{Im} \left[ \frac{z_1}{\sqrt{z_1^2 - l^2}} - \frac{z_2}{\sqrt{z_2^2 - l^2}} \right], \\
t_{12}^{\circ} &= -i_{21}^{\infty} \frac{\beta_1 \beta_2 \varepsilon_1 \varepsilon_2}{\beta_2 \varepsilon_1^2 - \beta_1 \varepsilon_2^2} \left\{ \beta_1 - \beta_2 - \operatorname{Re} \left[ \beta_1 \frac{z_1}{\sqrt{z_1^2 - l^2}} - \beta_2 \frac{z_2}{\sqrt{z_2^2 - l^2}} \right] \right\}, \\
t_{21}^{\circ} &= -i_{21}^{\infty} \left\{ 1 - \frac{\beta_2 \varepsilon_1}{\beta_2 \varepsilon_1^2 - \beta_1 \varepsilon_2^2} \operatorname{Re} \left[ \varepsilon_1 \frac{z_1}{\sqrt{z_1^2 - l^2}} - \frac{\beta_1 \varepsilon_2^2}{\beta_2 \varepsilon_1} \frac{z_2}{\sqrt{z_2^2 - l^2}} \right] \right\}.
\end{aligned}$$

### Elliptic complex regime

Within the EC regime, eqns. (2.41), and for Mode II, the Riemann-Hilbert problem:

$$-2 [\alpha(\delta^2 - \chi^2) + 2\beta\delta\chi] \operatorname{Re} \left[ \frac{F_1''(x_1)}{(\alpha + i\beta)(\chi + i\delta)} \right] = \frac{i_{21}^{\infty}}{\mu}, \quad \forall |x_1| < l, \quad (3.39)$$

has the following solution:

$$F_j''(z_j) = -\frac{i_{21}^{\infty}}{2\mu} \frac{[\alpha - (-1)^j i\beta][\chi - (-1)^j i\delta]}{\alpha(\delta^2 - \chi^2) + 2\beta\delta\chi} \left( 1 - \frac{z_j}{\sqrt{z_j^2 - l^2}} \right), \quad j = 1, 2, \quad (3.40)$$

so that the perturbed stream function becomes

$$\begin{aligned}
\psi^{\circ} &= -\frac{i_{21}^{\infty}}{4\mu} \frac{1}{\alpha(\delta^2 - \chi^2) + 2\beta\delta\chi} \sum_{j=1}^2 \operatorname{Re} \left\{ [\alpha - (-1)^j i\beta][\chi - (-1)^j i\delta] \right. \\
&\quad \left. \times \left[ z_j^2 - z_j \sqrt{z_j^2 - l^2} + l^2 \ln \left( z_j + \sqrt{z_j^2 - l^2} \right) \right] \right\}, \quad (3.41)
\end{aligned}$$

and the incremental displacements take the form

$$\begin{aligned}
v_1^{\circ} &= \frac{i_{21}^{\infty}}{2\mu} \frac{\alpha^2 + \beta^2}{\alpha(\delta^2 - \chi^2) + 2\beta\delta\chi} \left\{ \chi \operatorname{Re} \left[ \left( z_1 - \sqrt{z_1^2 - l^2} \right) - \left( z_2 - \sqrt{z_2^2 - l^2} \right) \right] \right. \\
&\quad \left. - \delta \operatorname{Im} \left[ \left( z_1 - \sqrt{z_1^2 - l^2} \right) + \left( z_2 - \sqrt{z_2^2 - l^2} \right) \right] \right\}, \quad (3.42)
\end{aligned}$$

$$v_2^\circ = \frac{t_{21}^\infty}{2\mu} \frac{1}{\alpha(\delta^2 - \chi^2) + 2\beta\delta\chi} \left\{ (\alpha\chi - \beta\delta) \operatorname{Re} \left[ \left( z_1 - \sqrt{z_1^2 - l^2} \right) + \left( z_2 - \sqrt{z_2^2 - l^2} \right) \right] \right. \\ \left. - (\beta\chi + \alpha\delta) \operatorname{Im} \left[ \left( z_1 - \sqrt{z_1^2 - l^2} \right) - \left( z_2 - \sqrt{z_2^2 - l^2} \right) \right] \right\}.$$

Finally, for Mode II in the EC regime, the incremental in-plane mean stress and the incremental nominal stress components are given by

$$\begin{aligned} \dot{p}^\circ &= \frac{t_{21}^\infty}{2} \frac{\alpha^2 + \beta^2}{\alpha(\delta^2 - \chi^2) + 2\beta\delta\chi} \left\{ (\delta^2 - k\chi) \operatorname{Re} \left[ \frac{z_1}{\sqrt{z_1^2 - l^2}} - \frac{z_2}{\sqrt{z_2^2 - l^2}} \right] \right. \\ &\quad \left. + \delta(\chi + k) \operatorname{Im} \left[ \frac{z_1}{\sqrt{z_1^2 - l^2}} + \frac{z_2}{\sqrt{z_2^2 - l^2}} \right] \right\}, \\ \dot{t}_{11}^\circ &= \frac{t_{21}^\infty}{2} \frac{\alpha^2 + \beta^2}{\alpha(\delta^2 - \chi^2) + 2\beta\delta\chi} \left\{ (\delta^2 - \chi^2) \operatorname{Re} \left[ \frac{z_1}{\sqrt{z_1^2 - l^2}} - \frac{z_2}{\sqrt{z_2^2 - l^2}} \right] \right. \\ &\quad \left. + 2\delta\chi \operatorname{Im} \left[ \frac{z_1}{\sqrt{z_1^2 - l^2}} + \frac{z_2}{\sqrt{z_2^2 - l^2}} \right] \right\}, \\ \dot{t}_{22}^\circ &= \frac{t_{21}^\infty}{2} \frac{(\alpha^2 + \beta^2)(\delta^2 + \chi^2)}{\alpha(\delta^2 - \chi^2) + 2\beta\delta\chi} \operatorname{Re} \left[ \frac{z_1}{\sqrt{z_1^2 - l^2}} - \frac{z_2}{\sqrt{z_2^2 - l^2}} \right], \\ \dot{t}_{12}^\circ &= -\frac{t_{21}^\infty}{2} \frac{(\alpha^2 + \beta^2)(\delta^2 + \chi^2)}{\alpha(\delta^2 - \chi^2) + 2\beta\delta\chi} \left\{ 2\alpha - \alpha \operatorname{Re} \left[ \frac{z_1}{\sqrt{z_1^2 - l^2}} + \frac{z_2}{\sqrt{z_2^2 - l^2}} \right] \right. \\ &\quad \left. - \beta \operatorname{Im} \left[ \frac{z_1}{\sqrt{z_1^2 - l^2}} - \frac{z_2}{\sqrt{z_2^2 - l^2}} \right] \right\}, \\ \dot{t}_{21}^\circ &= \frac{t_{21}^\infty}{2} \left\{ -2 + \operatorname{Re} \left[ \frac{z_1}{\sqrt{z_1^2 - l^2}} + \frac{z_2}{\sqrt{z_2^2 - l^2}} \right] \right. \\ &\quad \left. - \frac{\beta(\delta^2 - \chi^2) - 2\alpha\delta\chi}{\alpha(\delta^2 - \chi^2) + 2\beta\delta\chi} \operatorname{Im} \left[ \frac{z_1}{\sqrt{z_1^2 - l^2}} - \frac{z_2}{\sqrt{z_2^2 - l^2}} \right] \right\}. \end{aligned} \tag{3.43}$$

### 3.1.3 Incremental stress intensity factors

Similarly to the problem of fracture in small-strain elasticity, Radi et al. (2002) have defined

$$\dot{K}_I = \lim_{r \rightarrow 0} \sqrt{2\pi r} \dot{t}_{22}(r, \vartheta = 0), \quad \dot{K}_{II} = \lim_{r \rightarrow 0} \sqrt{2\pi r} \dot{t}_{21}(r, \vartheta = 0), \quad (3.44)$$

for Mode I and Mode II incremental loading, respectively, in the polar coordinate system  $(r, \vartheta)$  centered at the crack tip  $(\hat{x}_1 = l, \hat{x}_2 = 0)$ , so that  $r$  denotes the radial distance from the crack tip and  $\vartheta$  indicates values of the polar coordinate (anti-clockwise) angle singling out  $r$  from the  $\hat{x}_1$  axis (so that  $\vartheta=0$  corresponds to points ahead of the crack tip, see Fig. 3.2 with  $\vartheta_0 = 0$ ). From the above full-field solution (for uniform incremental loading at infinity), they result

$$\dot{K}_I = \dot{t}_{22}^\infty \sqrt{\pi l}, \quad \dot{K}_{II} = \dot{t}_{21}^\infty \sqrt{\pi l}, \quad (3.45)$$

for Mode I and Mode II loading, respectively. Note that, eqns. (3.45) coincide with their counterpart in elasticity without prestress, except that now the incremental nominal stress  $\dot{t}_{ij}$  replaces the Cauchy stress  $T_{ij}$ .

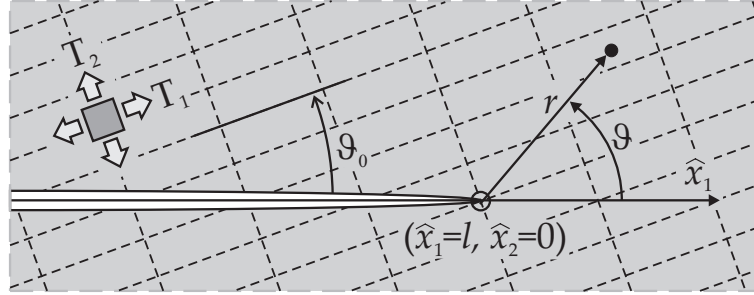


Figure 3.2: Polar coordinate system  $(r, \vartheta)$  centered at the crack tip  $(\hat{x}_1 = l, \hat{x}_2 = 0)$ . The prestress axes  $x_1 - x_2$  are inclined at an angle  $\vartheta_0$  with respect to the crack axis  $\hat{x}_1$ .

### 3.1.4 Crack solution and surface bifurcation condition

The previously obtained crack solution remains valid except when the surface bifurcation condition, eqn. (2.66), is met. This condition corresponds to the two conditions

$$\beta_2 \varepsilon_1^2 - \beta_1 \varepsilon_2^2 = 0, \quad \alpha(\delta^2 - \chi^2) + 2\beta\delta\chi = 0, \quad (3.46)$$

valid in EI and EC, respectively. When the surface bifurcation condition is approached, the fields, solution of the crack problem, tend to blow up, a peculiarity first noticed by Guz (1999, and references quoted therein).

For values of parameters  $\xi$ ,  $k$ , and  $\eta$  beyond the surface instability threshold, the obtained solution still works, from a purely mathematical point of view. However, the crack faces cannot be maintained straight after a surface bifurcation point has been passed, so that the solution loses its physical meaning (the incremental energy release rate, that will be obtained in §3.4, becomes negative in this situation).

### 3.2 Crack inclined with respect to the orthotropy axes

We consider now a crack inclined with respect to the  $x_1$ - $x_2$  axes defining the prestress directions and the orthotropy axes. Therefore, the  $x_1$ - $x_2$  reference system has to be distinguished from the system  $\hat{x}_1$ - $\hat{x}_2$ , where the  $\hat{x}_1$  axis is aligned parallel to the crack. The transformation between the two systems is expressed by eqn. (3.2), while the transformations between incremental displacement, its gradient, nominal stress and constitutive tensor are given by eqns. (3.3)–(3.5).

The trick to solve the inclined crack problem can be deduced from Savin (1961, see also Sih and Liebowitz, 1968) and consists in the introduction of a function analogous to (3.19) [see also eqns. (3.27), (3.36), and (3.41)], but now defined in the  $\hat{x}_1$ - $\hat{x}_2$  reference system, namely,

$$\hat{\psi}_M^\circ(\hat{x}_1, \hat{x}_2) = \frac{\hat{t}_{2n}^\infty}{2\mu} \sum_{j=1}^2 \operatorname{Re} \left\{ A_j^M \left[ \hat{z}_j^2 - \hat{z}_j \sqrt{\hat{z}_j^2 - l^2} + l^2 \ln \left( \hat{z}_j + \sqrt{\hat{z}_j^2 - l^2} \right) \right] \right\}, \quad (3.47)$$

(which automatically satisfies the decaying conditions of fields at infinity) where  $n = 1$  and  $M = II$  for Mode II ( $n = 2$  and  $M = I$  for Mode I), so that  $\hat{t}_{21}^\infty$  ( $\hat{t}_{22}^\infty$ ) is the traction component parallel (orthogonal) to the crack line. Moreover, a new variable, replacing  $z_j$  (2.36), is introduced

$$\hat{z}_j = \hat{x}_1 + W_j \hat{x}_2, \quad (3.48)$$

where

$$W_j = \frac{\sin \vartheta_0 + \Omega_j \cos \vartheta_0}{\cos \vartheta_0 - \Omega_j \sin \vartheta_0}, \quad (3.49)$$

and the roots  $\Omega_j$  are defined by eqn. (2.34).

Complex constants  $A_j^M$  in eqn. (3.47) can be obtained by imposing the boundary conditions on the crack faces, which are

$$\text{for Mode I} \quad \begin{cases} \hat{t}_{21}^\circ(\hat{x}_1, 0^\pm) = 0, \\ \hat{t}_{22}^\circ(\hat{x}_1, 0^\pm) = \hat{t}_{22}^\circ = -\hat{t}_{22}^\infty, \end{cases} \quad \forall |\hat{x}_1| < l; \quad (3.50)$$

$$\text{for Mode II} \quad \begin{cases} \hat{t}_{21}^\circ(\hat{x}_1, 0^\pm) = \hat{t}_{21}^\circ = -\hat{t}_{21}^\infty, \\ \hat{t}_{22}^\circ(\hat{x}_1, 0^\pm) = 0, \end{cases} \quad \forall |\hat{x}_1| < l. \quad (3.51)$$

Imposing conditions (3.50) or (3.51) yields a linear algebraic system for the real and imaginary parts of constants  $A_j^M$

$$\begin{bmatrix} c_{11} & c_{21} & c_{12} & c_{22} \\ -c_{21} & c_{11} & -c_{22} & c_{12} \\ c_{31} & c_{41} & c_{32} & c_{42} \\ -c_{41} & c_{31} & -c_{42} & c_{32} \end{bmatrix} \begin{bmatrix} \text{Re}[A_1^M] \\ \text{Im}[A_1^M] \\ \text{Re}[A_2^M] \\ \text{Im}[A_2^M] \end{bmatrix} = \underbrace{\begin{bmatrix} -1 \\ 0 \\ 0 \\ 0 \end{bmatrix}}_{\text{for Mode I}} \quad \text{or} \quad \underbrace{\begin{bmatrix} 0 \\ 0 \\ -1 \\ 0 \end{bmatrix}}_{\text{for Mode II}}, \quad (3.52)$$

where  $M = I$  for Mode I ( $M = II$  for Mode II) and coefficients  $c_{ij}$  are

$$\begin{aligned} 2\mu c_{1j} &= \hat{\mathbb{G}}_{1112} - \hat{\mathbb{G}}_{1222} - \text{Re}[W_j] \left[ \hat{\mathbb{G}}_{1111} - 2\hat{\mathbb{G}}_{1122} - \hat{\mathbb{G}}_{1221} + \hat{\mathbb{G}}_{2222} \right. \\ &\quad \left. + \text{Re}[W_j] \left( 2\hat{\mathbb{G}}_{1121} - 2\hat{\mathbb{G}}_{2122} + \text{Re}[W_j]\hat{\mathbb{G}}_{2121} \right) \right] \\ &\quad + \text{Im}[W_j]^2 \left( 2\hat{\mathbb{G}}_{1121} - 2\hat{\mathbb{G}}_{2122} + 3\text{Re}[W_j]\hat{\mathbb{G}}_{2121} \right), \\ 2\mu c_{2j} &= \text{Im}[W_j] \left[ \hat{\mathbb{G}}_{1111} - 2\hat{\mathbb{G}}_{1122} - \hat{\mathbb{G}}_{1221} + \hat{\mathbb{G}}_{2222} \right. \\ &\quad \left. + \text{Re}[W_j] \left( 4\hat{\mathbb{G}}_{1121} - 4\hat{\mathbb{G}}_{2122} + 3\text{Re}[W_j]\hat{\mathbb{G}}_{2121} \right) - \text{Im}[W_j]^2\hat{\mathbb{G}}_{2121} \right], \\ 2\mu c_{3j} &= -\hat{\mathbb{G}}_{1221} + \text{Re}[W_j] \left[ \hat{\mathbb{G}}_{1121} - \hat{\mathbb{G}}_{2122} + \text{Re}[W_j]\hat{\mathbb{G}}_{2121} \right] - \text{Im}[W_j]^2\hat{\mathbb{G}}_{2121}, \\ 2\mu c_{4j} &= \text{Im}[W_j] \left( -\hat{\mathbb{G}}_{1121} + \hat{\mathbb{G}}_{2122} - 2\text{Re}[W_j]\hat{\mathbb{G}}_{2121} \right), \quad j = 1, \dots, 4, \end{aligned} \quad (3.53)$$

and depend on the crack inclination  $\vartheta_0$  and on the prestress and orthotropy parameters  $\xi$ ,  $k$ , and  $\eta$ .

The determinant of the coefficient matrix in eqn. (3.52) is null only when the surface instability condition, eqn. (2.66), is met, so that in all other cases, system (3.52) can be solved and the solution of the inclined crack follows.

The perturbed incremental displacement along the crack faces can be obtained in the form

$$\begin{aligned}\hat{v}_1^{\circ M}(\hat{x}_1, \hat{x}_2 = 0^\pm) &= \frac{\hat{t}_{2n}^\infty}{2\mu} \operatorname{Re} \left[ (W_1 A_1^M + W_2 A_2^M) \left( \hat{x}_1 \mp i \sqrt{l^2 - \hat{x}_1^2} \right) \right], \\ \hat{v}_2^{\circ M}(\hat{x}_1, \hat{x}_2 = 0^\pm) &= -\frac{\hat{t}_{2n}^\infty}{2\mu} \operatorname{Re} \left[ (A_1^M + A_2^M) \left( \hat{x}_1 \mp i \sqrt{l^2 - \hat{x}_1^2} \right) \right],\end{aligned}\tag{3.54}$$

so that the jump in incremental displacements across the crack surfaces ( $|\hat{x}_1| < l$ ,  $\hat{x}_2 = 0$ ), denoted with the brackets  $[[\cdot]]$ , takes the form

$$\begin{aligned}[[\hat{v}_1^M]] &= \frac{\hat{t}_{2n}^\infty}{\mu} \operatorname{Im}[W_1 A_1^M + W_2 A_2^M] \sqrt{l^2 - \hat{x}_1^2}, \\ [[\hat{v}_2^M]] &= -\frac{\hat{t}_{2n}^\infty}{\mu} \operatorname{Im}[A_1^M + A_2^M] \sqrt{l^2 - \hat{x}_1^2},\end{aligned}\tag{3.55}$$

where  $n = 1$  and  $M = II$  ( $n = 2$  and  $M = I$ ) for Mode II (Mode I).

It is worth noting that the following conditions, proven in the particular cases of null prestress ( $k = \eta = 0$ ) or crack parallel to the orthotropy axes ( $\vartheta_0 = 0$ ), have been in general verified numerically to hold

$$\operatorname{Re}[A_1^I + A_2^I] = 0, \quad \operatorname{Re}[W_1 A_1^{II} + W_2 A_2^{II}] = 0,\tag{3.56}$$

showing that the incremental perturbed displacement along the  $x_1$ -axis outside the crack is only longitudinal, i.e.  $\hat{v}_2^\circ = 0$ , (transversal, i.e.  $\hat{v}_1^\circ = 0$ ), for Mode I (for Mode II), a circumstance noticed also by Broberg (1999, §4.14) for infinitesimal anisotropic elasticity.

In addition to eqns. (3.56), the following conditions are obtained in the particular case of a crack parallel to the orthotropy  $x_1$ -axis ( $\vartheta_0 = 0$ ),

$$\operatorname{Im}[W_1 A_1^I + W_2 A_2^I] = 0, \quad \operatorname{Im}[A_1^{II} + A_2^{II}] = 0,\tag{3.57}$$

from which the solution obtained in §3.1 can be easily recovered.

Finally, *the incremental stress intensity factors for an inclined crack can be calculated and again result in the form (3.45), found for a crack parallel to the orthotropy axes.*

The inclined crack solution becomes particularly simple in the case when the prestress is null,  $k = \eta = 0$ . In particular, for Mode I we have:

$$A_j^I = -(-1)^j \frac{\cos 2\vartheta_0}{2\sqrt{1-\xi}} - i \frac{1-\xi - (-1)^j \sqrt{1-\xi} \sin 2\vartheta_0}{2(1-\xi)\sqrt{\xi}}, \quad j = 1, 2, \quad (3.58)$$

while for Mode II:

$$A_j^{II} = (-1)^j \left[ \frac{\sin 2\vartheta_0}{2\sqrt{1-\xi}} + i \frac{\cos 2\vartheta_0}{2\sqrt{(1-\xi)\xi}} \right], \quad j = 1, 2. \quad (3.59)$$

The following properties can also be proven

$$W_1 A_1^I + W_2 A_2^I = 0, \quad A_1^{II} + A_2^{II} = 0. \quad (3.60)$$

An interesting feature that does not hold when the prestress is present and the crack is inclined can be deduced from eqns. (3.55), (3.60)<sub>1</sub> and (3.59), namely, that a Mode I (Mode II) loading does not produce longitudinal,  $v_1$ , (transversal,  $v_2$ ,) incremental displacements along the crack line, so that for ( $|\hat{x}_1| < l$ ,  $\hat{x}_2 = 0$ ) we have

$$[[\hat{v}]] = \left\{ \frac{\hat{t}_{21}^\infty}{\mu\sqrt{\xi}} \sqrt{l^2 - \hat{x}_1^2}, \quad \frac{\hat{t}_{22}^\infty}{\mu\sqrt{\xi}} \sqrt{l^2 - \hat{x}_1^2} \right\}, \quad (3.61)$$

which is independent of the crack inclination  $\vartheta_0$ .

As an example of the previous calculations, the deformed crack line and surfaces (incremental displacement components, reported on the vertical axis for  $\hat{v}_2$  and on the horizontal axis for  $\hat{x}_1 + \hat{v}_1$ , are normalized through division by  $l$ ) for Mode I (left) and Mode II (right) loading at infinity are illustrated in Fig. 3.3 for a Mooney-Rivlin material ( $\xi = 1$ ) at null prestress  $k = 0$  and at  $k = 0.8$  for a crack parallel to the orthotropy  $x_1$ -axis, i.e.  $\vartheta_0 = 0$ , and inclined at  $\vartheta_0 = \pi/6$ . Note that the Mode II deformation at null prestress,  $k = 0$  coincides with the horizontal axis and is therefore not visible.

Interesting features emerging from Fig. 3.3 are:

- i) the crack faces result displaced to the shape of an ellipse;*
- ii) this ellipse degenerates into a segment for Mode II and null prestress;*
- iii) the prestress introduces an incremental rigid-body rotation in the Mode I and Mode II solutions.*

### 3.3 Shear bands interacting with a finite-length crack

In the spirit of the perturbative approach proposed by Bigoni and Capuani (2002), the role of shear banding in the incremental deformation fields around

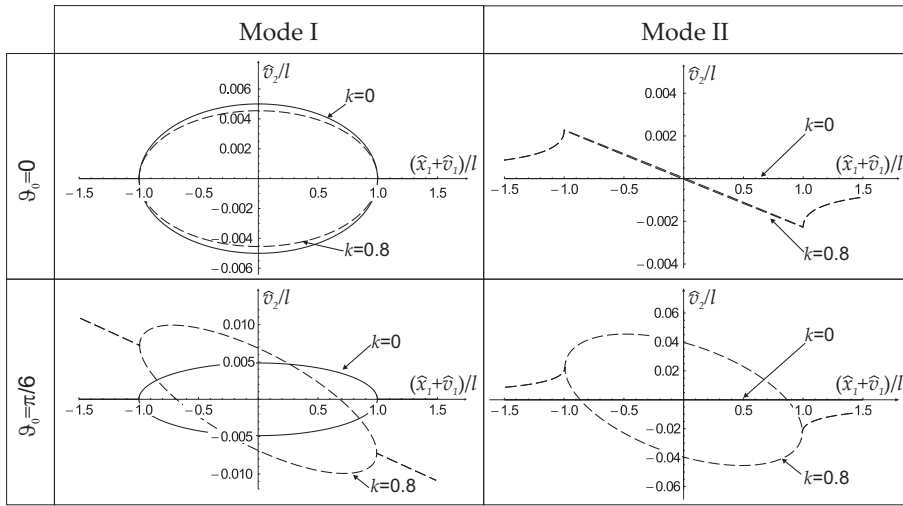


Figure 3.3: Deformed shape of a crack of length  $2l$ , subject to Mode I (left) and Mode II (right) incremental loading ( $\hat{t}_{22}^\infty/\mu = 0.01$  and  $\hat{t}_{21}^\infty/\mu = 0.01$ ). A Mooney-Rivlin material is considered with null prestress  $k = 0$  (continuous curve) and a prestress defined by  $k = 0.8$  (reported dashed). A crack is parallel to the  $x_1$ -orthotropy axis,  $\vartheta_0 = 0$  (upper part), while a second crack is inclined at an angle  $\vartheta_0 = \pi/6$  (lower part).

a crack of length  $2l$  is investigated. This crack is assumed to be present in the material with a dead loading on its surfaces to maintain the state of prestress, before the incremental Mode I and Mode II loading is assigned.

The crack is considered in a  $J_2$ -deformation theory material, inclined at an angle  $\vartheta_0$  corresponding to the shear band inclination  $\vartheta^{SB}$  at the EC/H boundary, eqn. (2.64). In particular, for the two values of hardening exponent  $N = 0.1$  and  $N = 0.8$ , the critical logarithmic strain for localization (and the shear band inclination with respect to  $x_1$ -axis) are  $\varepsilon^{EL} \simeq 0.322$  ( $\vartheta^{SB} \simeq 35.95^\circ$ ) and  $\varepsilon^{EL} \simeq 1.032$  ( $\vartheta^{SB} \simeq 19.60^\circ$ ), respectively (note that for a  $J_2$ -deformation theory material the prestrain, instead than the prestress, is used as the parameter controlling the current state).

The level sets of the modulus of incremental deviatoric strain have been mapped in Figs. 3.4 and 3.5, for low strain hardening  $N = 0.1$  and high strain hardening  $N = 0.8$ , respectively.

The investigation has been carried out with a choice of  $\eta$ , namely,  $\eta/k = 0.311$  for  $N = 0.1$  and  $\eta/k = 0.775$  for  $N = 0.8$ , such that the Hill exclusion condition (2.20) is satisfied.

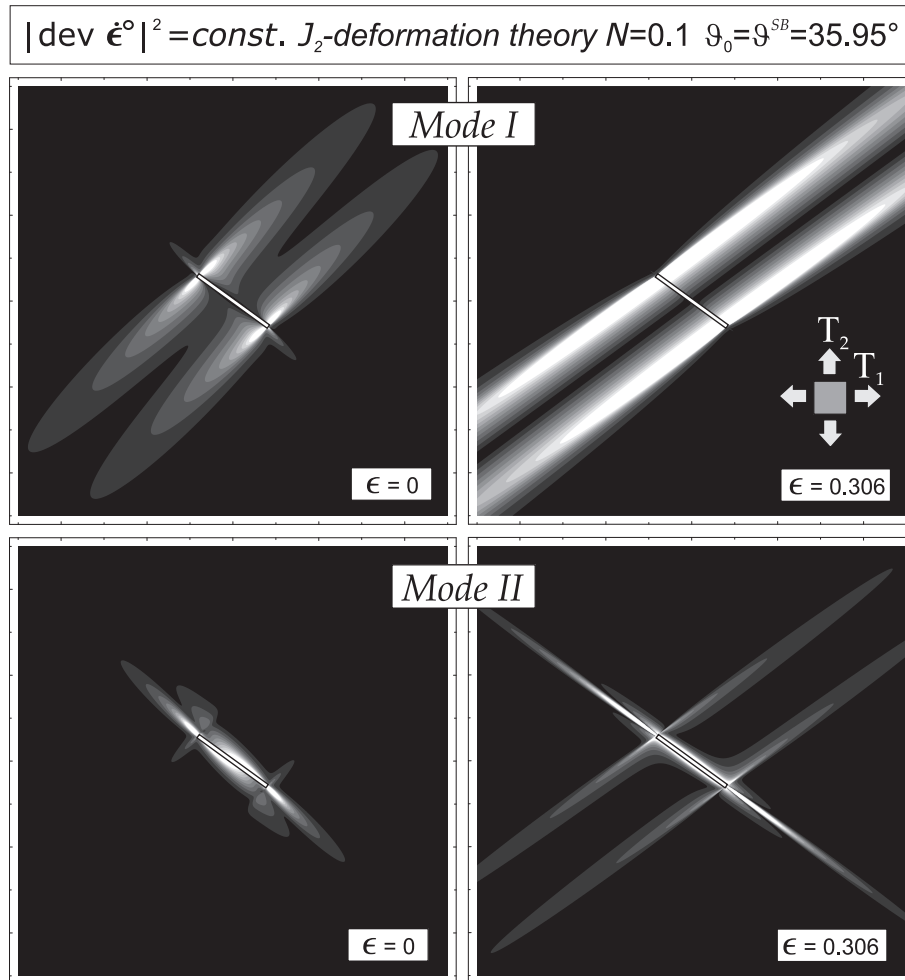


Figure 3.4: Interaction of shear bands and mechanical fields near a crack of length  $2l$  (evidenced with a thin rectangle, providing the scale bar of the representation). A  $J_2$ -deformation theory material has been considered at low strain hardening  $N = 0.1$ , at null prestrain  $\varepsilon = 0$  (on the left) and prestrained near the elliptic border  $\varepsilon = 0.306$  (on the right). The crack is aligned parallel to a shear band direction,  $\vartheta_0 = \vartheta^{SB} = 35.95^\circ$ . Two parallel bands emerge for Mode I incremental loading, while for Mode II two conjugate band directions are visible.

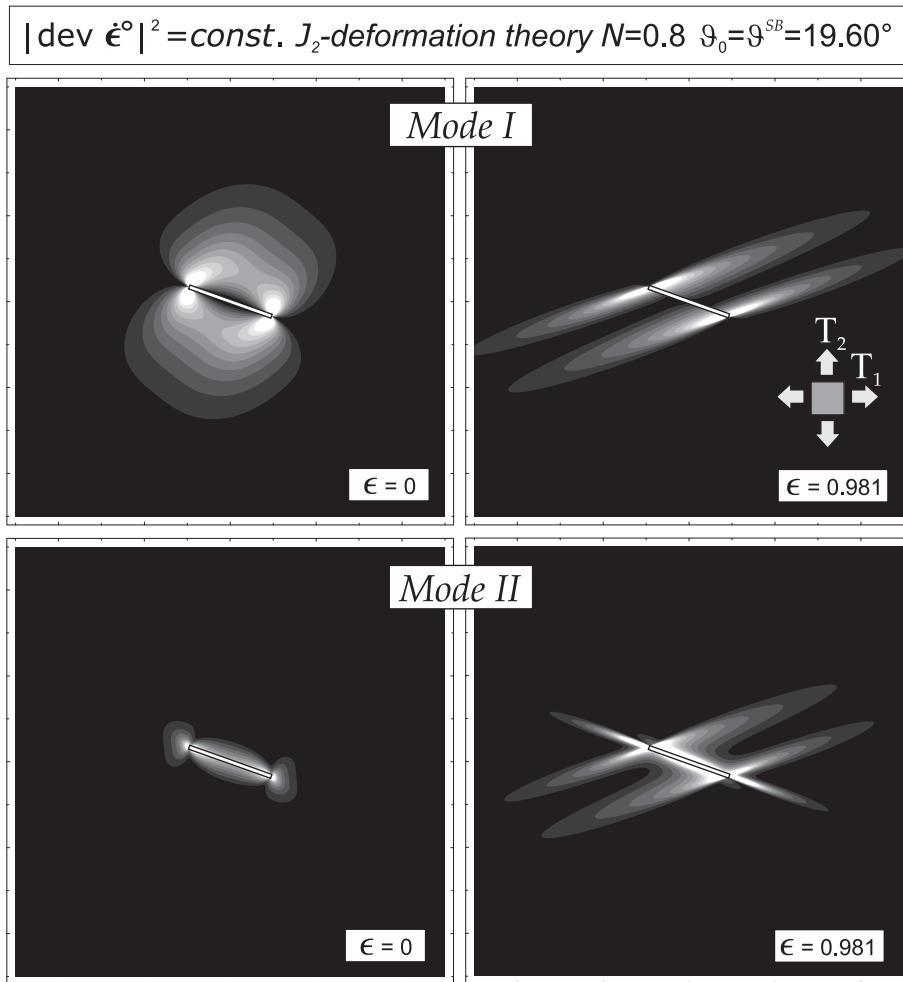


Figure 3.5: Interaction of shear bands and mechanical fields near a crack of length  $2l$  (evidenced with a thin rectangle, providing the scale bar of the representation). A  $J_2$ -deformation theory material has been considered at high strain hardening  $N = 0.8$ , at null prestrain  $\epsilon = 0$  (on the left) and prestrained near the elliptic border  $\epsilon = 0.981$  (on the right). The crack is aligned parallel to a shear band direction,  $\vartheta_0 = \vartheta^{SB} = 19.60^\circ$ . Two parallel bands emerge for Mode I incremental loading, while for Mode II two conjugate band directions are visible.

It can be easily concluded from Figs. 3.4 and 3.5 that:

*near the elliptic border the deformation fields become highly focussed and aligned parallel to the shear band conjugate directions.*

An analysis of the figures reveals that it becomes difficult to predict how the fracture will grow when loaded near the elliptic border. However, we have to keep in mind that the analyzed crack has been taken aligned parallel to one shear band direction. It becomes instructive now to analyze the case of a horizontal crack (lying therefore in a symmetry axis with respect to the conjugate band directions), reported in Fig. 3.6, for a  $J_2$ -deformation theory material at high strain hardening  $N = 0.8$ , near the EC/H boundary, and loaded under incremental Mode I. Results are qualitatively analogous for dif-

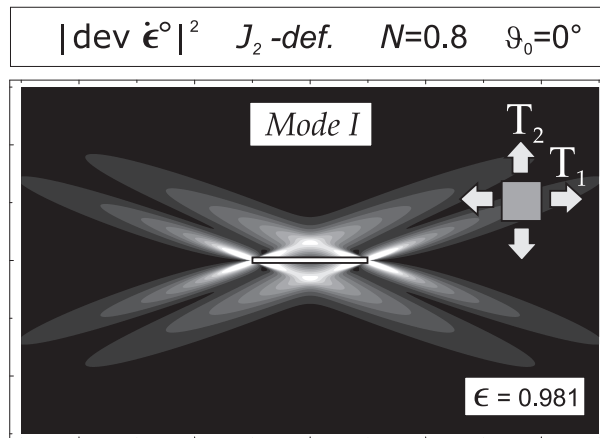


Figure 3.6: Interaction of shear bands and mechanical fields near a crack of length  $2l$  (evidenced with a thin rectangle, providing the scale bar of the representation) under Mode I incremental loading. A  $J_2$ -deformation theory material has been considered at high strain hardening  $N = 0.8$ , prestrained near the elliptic border  $\varepsilon = 0.981$ . The crack is horizontal  $\vartheta_0 = 0$ , while the shear bands are inclined at  $\vartheta^{SB} = \pm 19.60^\circ$ . Note that four shear bands emerge.

ferent values of strain hardening and for Mode II loading, in particular, the Mode II incremental deformation fields are dominated near the elliptic border by localized deformations aligned parallel to the two shear bands conjugate directions, in a way quite similar to Fig. 3.6.

We can observe that:

*two symmetric shear bands emerge near the crack tip,*

and their interaction may lead to failure of the material under shear in front of the crack, a situation compatible with Mode I growth, to be interpreted as a sort of ‘alternating sliding off and cracking’, as suggested by McClintock (1971), Kardomateas (1986) and Kardomateas and McClintock (1989). The situation is more complicated for Mode II loading, but our results agree with the consideration made by and Hallbäck and Nilsson (1994), that ‘Mode II failure results when the direction of the prospective shear band coincides with the crack surface direction, while Mode I type failure occurs when the shear bands are inclined to the direction of crack surfaces.’

### 3.4 Incremental energy release rate for crack growth

We slightly generalize Rice (1968) and start referring to Fig. 3.7 and comparing two incremental boundary value problems (for finite bodies subject to identical conditions on the external boundaries  $S_\sigma \cup S_v$ , namely, prescribed incremental nominal tractions  $\dot{\sigma}^0$  on  $S_\sigma$  and incremental displacements  $\mathbf{v} = \bar{\mathbf{v}}$  on  $S_v$ ) only differing in the sizes of the void that they contain. Note that we are addressing an incremental problem, so that the surface of the void can be loaded by dead loading. In particular, the void in the body on the right

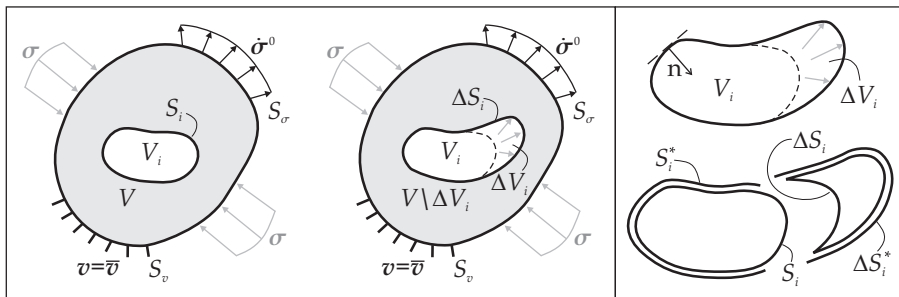


Figure 3.7: Two elastic, prestressed bodies are compared (left), having identical shape, boundary conditions, elastic properties, prestress, and prestrain, but voids of different size. The detail of the void and its surface is reported on the right; note the unit normal vector, defined to point outward the elastic body and toward the void. Incremental deformation of prestressed solids are considered, so that the surface of the void can be subject to finite dead loading and surface  $\Delta S_i^*$  must be subject to the nominal tractions present on the same surface embedded in the material in the configuration on the left.

(of volume  $V_i \cup \Delta V_i$ , enclosed by surface  $S_i^* \cup \Delta S_i^*$ ) has been obtained by increasing the size of the void in the body on the left (of volume  $V_i$ , enclosed

by surface  $S_i$ ).

Since we want to include prestress in an incremental formulation, nominal (finite) dead tractions identical to those existing within the material containing the void  $V_i$  must be applied on the surface  $\Delta S_i^*$  of the material containing the void  $V_i \cup \Delta V_i$ .

We define the incremental displacement and nominal traction fields, solutions to the two problems, as  $\mathbf{v}^0$  and  $\dot{\mathbf{t}}^0$  for the problem on the left and  $\mathbf{v} = \mathbf{v}^0 + \tilde{\mathbf{v}}$  and  $\dot{\mathbf{t}} = \dot{\mathbf{t}}^0 + \tilde{\mathbf{t}}$  for the problem on the right. Since the void surfaces are subject to dead loading,  $\dot{\mathbf{t}}^{0T} \mathbf{n} = \mathbf{0}$  and  $\dot{\mathbf{t}}^T \mathbf{n} = \mathbf{0}$ , within  $V_i$  and  $V_i \cup \Delta V_i$ , respectively.

The two bodies are assumed to be identically prestressed and prestrained, although not necessarily in a homogeneous way. If the expedient of prescribing ‘ad hoc’ dead tractions on  $\Delta S_i^*$  is not considered and the void surface is free of tractions, in order to have identical prestress and prestrain, the two current configurations shown in Fig. 3.7 must have special geometries and loadings, as will be the case of a crack aligned parallel to a principal stress direction with the other principal stress to be null and, more important, of a shear band model (§5.1).

The incremental potential energy decrease for a void growth in an elastic (incompressible or compressible, generically anisotropic and prestressed) body, takes an expression analogous to that reported by Rice [1968, his eqn. (55), pp. 207], namely,

$$-\Delta \dot{P} = \int_{\Delta V_i} \phi(\nabla \mathbf{v}^0) dV - \frac{1}{2} \int_{\Delta S_i^*} \mathbf{n} \cdot \dot{\mathbf{t}}^0 \tilde{\mathbf{v}} dS, \quad (3.62)$$

a quantity which when positive, implies void *growth*. Note that the scalar function  $\phi$  is the incremental gradient potential defined as

$$\dot{t}_{ij} = \frac{\partial \phi(\nabla \mathbf{v})}{\partial v_{j,i}} + \dot{p} \delta_{ij}, \quad \phi(\nabla \mathbf{v}) = \frac{1}{2} v_{j,i} \mathbb{G}_{ijhk} v_{k,h}. \quad (3.63)$$

Turning now the attention to a thin void inclusion, namely, a crack aligned parallel to the  $\hat{x}_1$ -axis (Fig. 3.1), the volume integral in eqn. (3.62) vanishes, so that taking the limit of the length increase  $\Delta l \rightarrow 0$  at fixed incremental stress intensity factor  $\hat{K}$ , eqn. (3.62) becomes

$$\dot{G} = -\frac{d\dot{P}}{dl} = \lim_{\Delta l \rightarrow 0} \frac{1}{2\Delta l} \int_0^{\Delta l} \hat{t}_{2i}(r, 0) [[\hat{v}_i(\Delta l - r, \pi)]] dr, \quad (3.64)$$

where the symbol  $\hat{\cdot}$  denotes that we are using the inclined crack solution, the repeated index is summed, the brackets  $[[\cdot]]$  denote the jump in the relevant

argument across the crack,  $r$  denotes the radial distance from the crack tip and 0 and  $\pi$  indicate values of the polar coordinate (anticlockwise) angle singling out  $r$  from the  $\hat{x}_1$  axis (so that  $\vartheta = 0$  corresponds to points ahead of the crack tip, see Fig. 3.2). Eqn. (3.64) defines

*the incremental energy release rate for a mixed mode growth of a crack in an elastic, incompressible or compressible body, generically anisotropic and prestressed.*

The proof that the incremental energy release rate (3.64) coincides with the path-independent incremental  $\dot{J}$ -integral

$$\dot{J} = \int_{\Gamma} \left( \hat{\phi} \hat{n}_1 - \hat{n}_j \hat{t}_{ji} \frac{\partial \hat{v}_i}{\partial \hat{x}_1} \right) d\Gamma, \quad (3.65)$$

has not yet been explicitly obtained, but the validity of  $\dot{G} = \dot{J}$  has been numerically verified.

The incremental energy release rate (3.64) can be developed making use of the asymptotic near-tip incremental nominal stress ahead of the crack

$$\hat{t}_{22}(r, 0) = \frac{\dot{K}_I}{\sqrt{2\pi r}}, \quad \hat{t}_{21}(r, 0) = \frac{\dot{K}_{II}}{\sqrt{2\pi r}}, \quad (3.66)$$

and incremental displacement on the crack faces (where constants have been neglected)

$$\begin{aligned} \hat{v}_1(\Delta l - r, \pm\pi) &= \pm \frac{\sqrt{2l}\sqrt{\Delta l - r}}{2\mu} \text{Im} \left[ \hat{t}_{22}^{\infty}(W_1 A_1^I + W_2 A_2^I) + \hat{t}_{21}^{\infty}(W_1 A_1^{II} + W_2 A_2^{II}) \right], \\ \hat{v}_2(\Delta l - r, \pm\pi) &= \mp \frac{\sqrt{2l}\sqrt{\Delta l - r}}{2\mu} \text{Im} \left[ \hat{t}_{22}^{\infty}(A_1^I + A_2^I) + \hat{t}_{21}^{\infty}(A_1^{II} + A_2^{II}) \right], \end{aligned} \quad (3.67)$$

holding for ‘small’  $\Delta l$ .

Employing the asymptotic near-tip representations (3.66) and (3.67) in eqn. (3.64) we obtain

$$\begin{aligned} \dot{G} &= -\dot{K}_I^2 \frac{\text{Im} [A_1^I + A_2^I]}{4\mu} + \dot{K}_{II}^2 \frac{\text{Im} [W_1 A_1^{II} + W_2 A_2^{II}]}{4\mu} \\ &\quad + \dot{K}_I \dot{K}_{II} \frac{\text{Im} [W_1 A_1^I + W_2 A_2^I - A_1^{II} - A_2^{II}]}{4\mu}, \end{aligned} \quad (3.68)$$

*the incremental energy release rate for an inclined crack loaded in mixed mode in a prestressed, orthotropic and incompressible material.*

From eqn. (3.68) the incremental energy release rate for a mixed mode loading of a crack parallel to the orthotropy axes (i.e.  $\vartheta_0 = 0$ ) can be made explicit

$$\dot{G} = \frac{\Lambda}{\mu} \frac{\dot{K}_I^2 \sqrt{1-k} + \dot{K}_{II}^2 \sqrt{1+k}}{(2\xi - \eta + \Lambda)^2 \sqrt{2\xi - 1 - \Lambda} - (2\xi - \eta - \Lambda)^2 \sqrt{2\xi - 1 + \Lambda}}, \quad (3.69)$$

where there is no coupling between the two Modes I and II.

Another interesting special case is that of null prestress ( $k = \eta = 0$ ), in which for an inclined crack ( $\vartheta_0 \neq 0$ ) the following expression of the incremental energy release rate can be obtained

$$\dot{G} = \frac{\dot{K}_I^2 + \dot{K}_{II}^2}{4\mu\sqrt{\xi}}, \quad (3.70)$$

which agrees with the known isotropic elasticity solution in the incompressible limit, recovered for  $\xi = 1$ .

Note that both incremental energy release rates (3.69) and (3.68) generally (an exception to this rule will be shown in Fig. 3.8) blow up to infinity when the surface bifurcation, eqn. (2.66) or (3.46), is approached, as in the case of the crack aligned parallel to one of the orthotropy axes. This feature is evident in the example reported below.

An example of calculation of incremental energy release rate for inclined (at  $\vartheta_0 = \{0, \pi/4, \pi/2\}$ ) Mode I and a Mode II cracks in an incrementally isotropic material ( $\xi = 1$ ) as a function of the prestress parameter  $k$  is reported in Fig. 3.8, where  $\dot{G}$  has been normalized through division by  $\dot{K}_M^2$  and multiplication by  $4\mu$ . In order to explore the incremental energy release rate until close to the elliptic boundary (more precisely, to the EI/P boundary), we have taken  $\eta = k > 0$ , so that the Hill condition (2.20) excludes all possible bifurcations within EI (Fig. 2.5). It may be interesting to observe from Fig. 3.8 that, with the exceptions of  $\vartheta_0 = 0$  for Mode I and  $\vartheta_0 = \pi/2$  for Mode II, the incremental energy release rate blows up to infinity when  $k$  approaches 1. These exceptions can be motivated by the circumstance that at the EI/P boundary only one shear band forms aligned parallel to the major principal (tensile in this case) stress component,  $T_1$ . Therefore, for Mode I (Mode II) a crack parallel (orthogonal) to the shear band is not influenced by the progressive weakening in the shear band direction occurring when the elliptic boundary is approached.

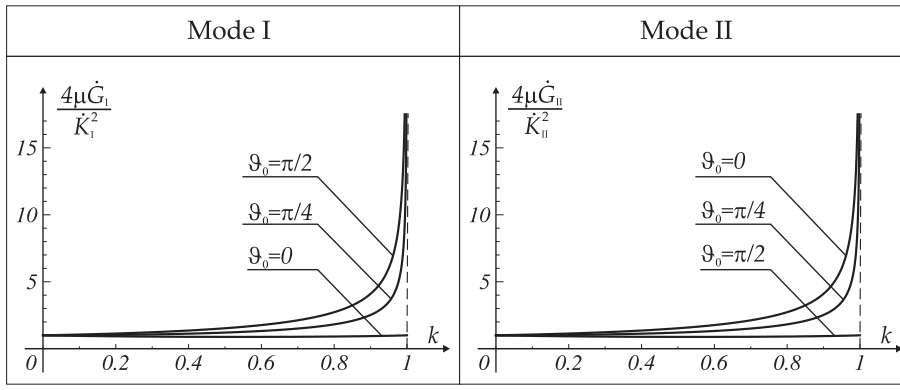


Figure 3.8: Incremental stress release rate for a Mode I and Mode II cracks of length  $2l$  inclined at  $\vartheta_0 = \{0, \pi/4, \pi/2\}$  with respect to the principal stress axes in an incrementally isotropic material ( $\xi = 1$ ) as a function of the prestress parameter  $k$ , taken positive and equal to  $\eta$ , so that the Hill exclusion criterion (2.20) is satisfied.

Note that for a Mooney-Rivlin material  $\mu$  is a function of  $k$ , blowing up to infinity, when the EI/P boundary ( $k = 1$ ) is approached. As a consequence, for a Mooney-Rivlin material the energy release rate remains finite when  $k$  tends to 1.

Note that for null prestress,  $\eta = k = 0$ , eqn. (3.70) shows that the incremental energy release rate blows up to infinity when  $\xi$  tends to zero, which corresponds to the EC/H boundary and to the appearance of the two shear bands inclined at  $\pi/4$  with respect to the principal stress direction, typical of Mises plasticity.

Fig. 3.8 reveals another interesting feature, namely, that the curves corresponding to  $\vartheta_0 = \{0, \pi/4, \pi/2\}$  in Mode I are identical to the curves corresponding, respectively, to  $\vartheta_0 = \{\pi/2, \pi/4, 0\}$  in Mode II. More in general, the following relation can be proven in the absence of prestress using eqns. (3.58) and (3.59)

$$\frac{\dot{G}_I(\vartheta_0)}{\dot{K}_I^2} = \frac{\dot{G}_{II}(\pi/2 - \vartheta_0)}{\dot{K}_{II}^2}, \quad (3.71)$$

and has been numerically found to hold also when the prestress is different from zero.

## Chapter 4

---

### Stiffener in a prestressed material

*A rigid line inclusion, a so-called ‘stiffener’, embedded in a prestressed material incrementally loaded is considered. The obtained analytical solutions explain the experimentally observed localized deformation patterns in highly deformed soft materials containing thin, stiff inclusions. For null prestress, the full-field solution is shown to match correctly with photoelastic experiments, confirming also the fracture patterns for a brittle material containing a stiffener, which do not obey a hoop-stress criterion and result completely different from those found for cracks. Moreover, the incremental energy release rate and incremental  $J$ -integral are derived, related to a reduction (or growth inhibition) of the stiffener. It is shown that this is always negative, but tends to zero approaching the ellipticity boundary, which implies that reduction of the lamellar inclusion dies out and, simultaneously, shear bands develop.*

Imposing large deformation to a soft, ductile metal matrix containing a thin lamellar hard phase is a well-established industrial process for the production of ultra high strength materials (Öztürk et al. 1994, Michler et al. 2004). Experiments on these materials show that localized deformations in the form of shear bands nucleate at inclusion boundaries, where they grow and subsequently develop complex interactions between themselves and the second phase. Therefore, the presence of defects is crucially important in the understanding of failure in ductile matrix composites, particularly when defects involve stress concentrations, as is the case of the lamellar suspensions experimentally investigated in metals (Öztürk et al., 1991), plastics (Fig. 1.1), and rocks (Misra and Mandal, 2007).

The availability of an analytical solution for a thin, rigid inclusion, a so-called ‘stiffener’, embedded in a remotely-loaded, infinite medium –in which stress and displacement fields can be obtained for an incremental perturbation superimposed upon a stress state near the boundary of ellipticity loss– is important for understanding the mechanical behaviour of the above-mentioned composite materials. Moreover, we also notice that (even for linearly elastic isotropic materials) a stiffener determines a singular solution that poses a number of questions, not arising in other situations (particularly, in the case of a crack, which induces the same singularity). In fact, it can be observed that:

- i) While cracks can ‘naturally’ exist in ordinary materials, can a stiffener –which necessarily is something artificial– be in practice introduced in a real material?
- ii) Due to several possible discrepancies (not arising in the crack problem) between model and reality (a stiff, thin inclusion has a finite thickness and stiffness, and adhesion at the stiffener/matrix contact is necessarily imperfect), will the real stress state correspond to the elastic solution?
- iii) Unlike cracks, stiffeners can produce a singular, nontrivial stress even when they are subject to compressive stresses or when they are pulled in uniaxial tension parallelly to them. Will a material in these cases fail due to the presence of the singularity?
- iv) For tensile (or compressive) loading parallel (or orthogonal) to the stiffener, the material is predicted to fail through the generation of a fracture orthogonal to the stiffener at its end and not following the hoop-stress criterion valid for cracks. Will this prediction be in practice true?

Having found nothing on these issues in the literature, we have designed and realized stiffeners in a real material and produced and tested samples (details are reported in appendix A).<sup>1</sup> Results of two experiments are shown in Figs. 1.2 and 1.3.

In particular, the isochromatic fringe pattern recorded in a transmission photoelastic test performed with a plane polariscope is reported in Fig. 1.2, strikingly confirming the analytical solution for the in-plane principal stress difference contours (an incompressible, isotropic material initially unstressed has been considered).

---

<sup>1</sup>Additional experimental results are available on:

[http://www.ing.unitn.it/dims/laboratories/structural\\_modeling\\_photoelasticity.php](http://www.ing.unitn.it/dims/laboratories/structural_modeling_photoelasticity.php)

The fracture growth sequence for tensile loading parallel to the stiffener is reported in Fig. 1.3, which –according to the linear elastic theory (with null prestress)– develops orthogonally to the stiffener end. Therefore, our experiments provide positive answers to the questions listed above, so that the stiffener model may be considered a sound model in elasticity<sup>2</sup> (a systematic discussion on Mode I fracture modes at a stiffener tip is reported in §4.1.2).

Going back now to the main goal of this Chapter, a homogeneously prestressed (or prestrained), incompressible elastic infinite plane is considered, characterized by the constitutive equations (2.6) of incremental, incompressible, orthotropic elasticity, containing a stiffener of length  $2l$ , taken parallel to the  $\hat{x}_1$ -axis in the  $\hat{x}_1$ - $\hat{x}_2$  reference system (Fig. 4.1). The fact that a stiff-

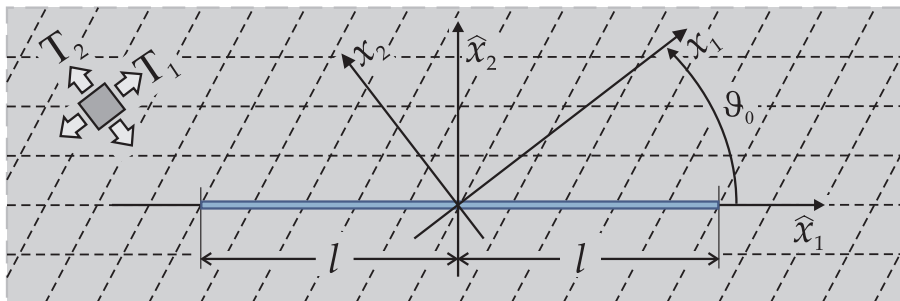


Figure 4.1: The rigid line inclusion (of length  $2l$ ) in an infinite, incompressible, homogeneously prestressed material. The state of stress has the principal axes  $x_1$ - $x_2$  inclined with respect to the  $\hat{x}_1$ - $\hat{x}_2$  reference system at an angle  $\vartheta_0$  (positive when anticlockwise).

ener can only suffer an incremental rigid-body motion is expressed by the kinematical boundary conditions

$$\begin{cases} \hat{v}_1(\hat{x}_1, 0) = \hat{v}_1(0, 0), \\ \hat{v}_2(\hat{x}_1, 0) = \hat{v}_2(0, 0) + \omega_S x_1, \end{cases} \quad \forall |\hat{x}_1| < l, \quad (4.1)$$

so that  $\hat{v}_1(0, 0)$ ,  $\hat{v}_2(0, 0)$  and  $\omega_S$  represent unknown quantities to be deter-

<sup>2</sup>It may be worth noting that our photoelastic and failure experiments show that the hypotheses of plane strain and incompressibility do not alter results qualitatively. Regarding the former assumption, since a stiffener imposes null deformation on his surface, any sufficiently wide platelet embedded in a material will have a state of plane strain prevailing near its centre (see also the discussion reported in appendix A). Regarding the latter assumption, extension of our results to compressible orthotropic, incremental elasticity is straightforward and does not change qualitatively results for shear band emergence.

mined as a part of the solution,<sup>3</sup> by imposing boundary conditions to ensure equilibrium of the stiffener in terms of incremental ‘global’ axial and shearing forces, and incremental moment, respectively

$$\begin{cases} \dot{\mathcal{N}} = \int_{-l}^l [[\hat{t}_{21}(y, 0)]] dy = 0, \\ \dot{\mathcal{T}} = \int_{-l}^l [[\hat{t}_{22}(y, 0)]] dy = 0, \\ \dot{\mathcal{M}} = \int_{-l}^l [[\hat{t}_{22}(y, 0)]] y dy = 0, \end{cases} \quad (4.3)$$

where the brackets  $[[\cdot]]$  denote the jump in the relevant argument, taken across the stiffener.

The Mode I and Mode II asymptotic fields when the  $x_1$ – $x_2$  axes, defining the prestress directions, coincide with the  $\hat{x}_1$ – $\hat{x}_2$  axes are obtained in §4.1.1, revealing a stress singularity  $\sim 1/\sqrt{r}$ , as in the case when the prestress is absent. Moreover, a perturbation in the form of a uniform Eulerian strain increment field is considered at infinity (§4.1.3). In this case, only the perturbation stress fields satisfying Mode I symmetry are non-trivial (for incremental shear deformation at infinity the stiffener leaves the fields unperturbed) and their determination represents the solution of a Riemann-Hilbert problem, which is already known in the absence of prestress for isotropic or anisotropic (compressible) elasticity (Wang et al. 1985; Ballarini, 1987; Wu, 1990; Hurtado et al. 1996; Dascalu and Homentcovschi, 1999; Homentcovschi and Dascalu, 2000; see also Koiter, 1955; Erdogan and Gupta, 1972; Atkinson, 1973 where an elastic lamellar inclusion has been considered), but has never been considered for a prestressed material.<sup>4</sup>

These solutions can be exploited until near the boundary of ellipticity loss to investigate shear band nucleation and growth. Shear bands are shown (§4.1.5):

- i) to be strongly promoted by the near-tip singularity;

---

<sup>3</sup>The kinematical boundary conditions (4.1) imply

$$\hat{v}_{1,1}(\hat{x}_1, 0) = \hat{v}_{2,11}(\hat{x}_1, 0) = 0, \quad \forall |\hat{x}_1| < l, \quad (4.2)$$

<sup>4</sup>A.N. Guz and co-workers (see Guz, 1999 and references quoted therein) and E. Soós and co-workers (see Cristescu et al. 2004 and references quoted therein) have solved a number of problems for prestressed elastic materials, but they have never considered stiffeners.

- ii) to *emanate radially* from the tip of the stiffener;
- iii) to have an inclination independent of the perturbing agent;
- iv) to form patterns sharing a strict similarity (results obtained with our solution are shown in Figs. 4.2, right, and 1.1, right, lower part) with those experimentally investigated:
  - by Öztürk et al. (1991) in a ductile Cu matrix containing stiff W platelets, see Fig. 4.2, left;
  - by us on a two-component epoxy resin square plate (sample S3, see appendix A) containing an aluminum platelet and subject to uniaxial in-plane compression orthogonal to the long edge of the platelet, see Fig. 1.1, left and right (upper part).

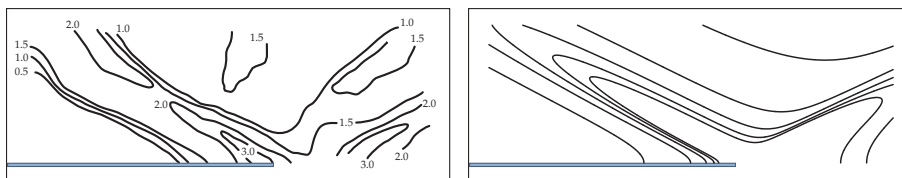


Figure 4.2: Deformation near a thin and stiff inclusion: experimental results, deformation map in a Cu matrix near a W platelet (adapted from Öztürk et al. 1991), left, versus analytical solution for a  $J_2$ -material, prestrained until close to the boundary of ellipticity loss ( $\epsilon = 0.675$  and  $N = 0.4$ ), right.

Moreover, the full-field solution for a uniform Mode I perturbation is also obtained in the generic case of a stiffener inclined with respect to the prestress directions (§4.2).<sup>5</sup> Considering a  $J_2$ -deformation theory material the obtained solution shows the development of two shear bands, with, for low hardening, the one closest in alignment with the stiffener being the more pronounced.<sup>6</sup> Therefore, a stiffener embedded in a low hardening matrix tends to focus the deformation parallel to its line, a finding substantiated by the experimental

<sup>5</sup>Note that Mode I loading is defined with respect to the axes parallel and orthogonal to the stiffener.

<sup>6</sup>Differently from the case of a stiffener parallel to prestress axis, now the two axial-symmetries are lost, so that the shear bands are not symmetrical with respect to the stiffener line and one of the two becomes a preferential failure mode.

results by Misra and Mandal (2007), referred to geological formations and to models prepared with PMMA containing metal inclusions.<sup>7</sup>

Accepting the fact that decay of the incremental fields does not occur and incremental strain and stress becomes infinite along certain shear band directions, the obtained solution is extended and investigated outside ellipticity, namely, in the parabolic and hyperbolic regimes in §4.3. Here it is shown that the solution is not unique, so that one, two, three or four (one or two) differently inclined shear bands are predicted to become possible in the hyperbolic (parabolic) range. This result substantiates with an analytical solution the well-known difficulties connected to the numerical treatment of ill-posed (i.e. non-elliptic) boundary value problems.

Finally, analogously to the akin crack problem (Rice, 1968), it is possible to analyze the energy release rate involved with a growth of the stiffener. This problem has never been considered (even for linear isotropic elasticity without prestress) and can be more effectively understood in relation to a *reduction* than to a growth of a stiffener. In fact, *reduction can model the situation in which an intact, thin and finite-length material layer is present within a (uniformly) damaged material and progressively reduces its length, due to damage growth.*<sup>8</sup> This situation can be related to damage progression, which may under special circumstances spread through solids evidencing a fingering, similar in a sense to the fingering flow phenomena observable in porous systems or to the adhesion-induced instability in thin films (Saffman and Taylor, 1958; Ghatak and Chaudhury, 2003). Therefore, investigation of energy release rate for a stiffener changing in length may shed light on the problem of damage growth in solids.

The incremental energy release rate for stiffener growth (we refer to growth to keep contact with the analogous problem of fracture mechanics, so that reduction is simply understood as a negative growth) is solved in §4.4 for incremental deformation superimposed upon a given state of stress and strain (initially assumed generic, but later uniform in the applications) of an incompressible elastic solid. However, since these results are new, we remark

---

<sup>7</sup>We include in appendix D the solution where for a stiffener forced to incrementally rotate (through application of an external incremental bending moment) of a given amount, a problem modelling the mechanical fields generated through the so-called ‘vane test’ in soil mechanics. Differently from the case when the inclusion is embedded in a matrix and loaded at infinity, in this situation we show that the two shear bands more inclined with respect to the stiffener become the preferred failure modes.

<sup>8</sup>In a different setting, stiffener and matrix could be the two (the former much stiff than the latter) phases of a material, so that stiffener growth or reduction would be related to a progression or regression of a phase transformation.

that the small strain theory and the compressible prestressed elasticity can be immediately obtained from our formulation.

It will be shown that, differently from the well-known formulae of fracture mechanics, the incremental energy release rate is always negative (so that reduction is always predicted and growth never occurs). Moreover, the incremental energy release rate is shown to vanish when the elliptic boundary is approached (more precisely, there may be exceptions to this rule at the EI/P boundary, a circumstance that will be detailed later). This finding implies that the reduction of the stiffener dies out when the boundary of ellipticity is approached and, at the same time, our previous results show that shear bands begin to emerge at the stiffener tip. We therefore find an intriguing interplaying between shear band nucleation and slowing down of stiffener reduction process.

## 4.1 Stiffener parallel to an orthotropy axis

The solutions obtained in this Section are strictly valid when the state of prestress upon which the perturbations are superimposed is uniform and has principal axes aligned with respect to stiffener line (Fig. 4.1 with  $\vartheta_0 = 0$ ). When a perturbation through an incremental Mode I or II loading is applied, the incremental displacement field satisfy the symmetry conditions, which are

$$\text{for Mode I} \quad \begin{cases} v_1(x_1, x_2) = v_1(x_1, -x_2), \\ v_2(x_1, x_2) = -v_2(x_1, -x_2); \end{cases} \quad (4.4)$$

$$\text{for Mode II} \quad \begin{cases} v_1(x_1, x_2) = -v_1(x_1, -x_2), \\ v_2(x_1, x_2) = v_2(x_1, -x_2). \end{cases} \quad (4.5)$$

Obviously, such a uniform prestress state cannot result from uniform remote loading of a homogeneous material containing a stiffener. Therefore, our calculations are strictly applicable to a model problem, which describes a situation in which a uniform stress is generated, for instance, through a constrained transformation strain (such a uniform temperature variation or phase transformation of a specimen with prevented displacements at the boundary, see Li et al. 2003 and Zheng et al. 2000), or in which a rigid thin layer is ‘welded’ subsequently to a uniform prestrain of a material. However, direct comparison of our solutions with experimental results performed by Öztürk et al. (1991) and by us shows that our model is able to correctly predict the shear

band patterns evidenced near the tip of the stiffener when the surrounding field is inhomogeneously deformed (a circumstance also confirmed by numerical solutions not reported for conciseness). The explanation for this is that the incremental deformation found near the elliptic boundary in a homogeneously prestressed material is a sort of ‘ultimate deformation mode’, sweeping the previously accumulated strain and dominating the near-failure fields. Something similar is occurring for perfectly plastic solids, where slip line solutions, obtained without consideration of the previous stress/strain evolution, are in pretty close agreement with shear bands visible in experiments.

#### 4.1.1 Asymptotic solution

Near the tip of the rigid line inclusion the kinematic and static fields may be approximated by their asymptotic expansions. Let us focus on the tip of coordinates  $(l, 0)$ . The complex variables  $z_j$  ( $j = 1, \dots, 4$ ) defined in (2.36) admit the polar representation

$$z_j = l + r_j e^{i\vartheta_j}, \quad j = 1, \dots, 4; \quad \text{no sum on index } j, \quad (4.6)$$

with

$$r_j = r \sqrt{(\cos \vartheta + \alpha_j \sin \vartheta)^2 + \beta_j^2 \sin^2 \vartheta}, \quad (4.7)$$

$$\tan \vartheta_j = \frac{\beta_j \sin \vartheta}{\cos \vartheta + \alpha_j \sin \vartheta}, \quad j = 1, \dots, 4; \quad \text{no sum on index } j,$$

where  $r$  and  $\vartheta$  are the polar coordinates of a generic point (see Fig. 3.2, in which the crack should be thought to represent a stiffener and  $\vartheta_0 = 0$ ).

In the neighbourhood of the tip  $(l, 0)$  the stream function can be now expressed in the power-expansion form

$$\psi(x_1, x_2) = \frac{2\dot{K}}{3\mu\sqrt{\pi}} \sum_{j=1}^4 A_j (z_j - l)^\gamma = \frac{4\dot{K}}{3\mu\sqrt{\pi}} \sum_{n=1}^2 \text{Re}[A_n w_n^\gamma], \quad (4.8)$$

where the notation,

$$w_j = z_j - l = r_j e^{i\vartheta_j}, \quad j = 1, \dots, 4, \quad (4.9)$$

has been introduced. The last term is a two-term summation because  $\overline{w_j^\gamma} = \overline{w_j}^\gamma$  and, as the stream function must be real-valued, the complex constants  $A_j$  satisfy the property,

$$A_3 = \overline{A_1}, \quad A_4 = \overline{A_2}. \quad (4.10)$$

Constants  $A_n$  ( $n = 1, 2$ ) may be represented as

$$A_n = a_n + ib_n \quad n = 1, 2, \quad (4.11)$$

with  $a_n$  and  $b_n$  real constants. The parameter  $\dot{K}$  plays the role of an incremental intensity factor, remains undetermined in an asymptotic analysis and will be discussed in detail later in this Section.

### Elliptic complex regime

In the EC regime the roots  $\Omega_j$  ( $j = 1, \dots, 4$ ) assume the form (2.43). The asymptotic expansions of the incremental quantities may be obtained by substituting the expression of the stream function (4.8)<sub>2</sub> in (2.30), (2.6), and (2.29) (see Radi et al. 2002 for details) to yield

$$\begin{aligned} v_1 &= \frac{4\gamma\dot{K}}{3\mu\sqrt{\pi}} \sum_{n=1}^2 \{(-1)^n \alpha \operatorname{Re}[A_n w_n^{\gamma-1}] - \beta \operatorname{Im}[A_n w_n^{\gamma-1}]\}, \\ v_2 &= -\frac{4\gamma\dot{K}}{3\mu\sqrt{\pi}} \sum_{n=1}^2 \operatorname{Re}[A_n w_n^{\gamma-1}], \\ t_{11} &= \frac{4\gamma\dot{K}}{3\sqrt{\pi}} (\gamma - 1) \sum_{n=1}^2 \{(-1)^n (\beta\delta + \chi\alpha) \operatorname{Re}[A_n w_n^{\gamma-2}] + (\alpha\delta - \chi\beta) \operatorname{Im}[A_n w_n^{\gamma-2}]\}, \\ t_{22} &= \frac{4\gamma\dot{K}}{3\sqrt{\pi}} (\gamma - 1) \sum_{n=1}^2 \{(-1)^n (\beta\delta - \chi\alpha) \operatorname{Re}[A_n w_n^{\gamma-2}] + (\alpha\delta + \chi\beta) \operatorname{Im}[A_n w_n^{\gamma-2}]\}, \\ t_{12} &= -\frac{4\gamma\dot{K}}{3\sqrt{\pi}} (\gamma - 1) \sum_{n=1}^2 \{(\chi\beta^2 - \chi\alpha^2 + 2\alpha\beta\delta) \operatorname{Re}[A_n w_n^{\gamma-2}] \\ &\quad + (-1)^n (\delta\alpha^2 - \delta\beta^2 + 2\chi\alpha\beta) \operatorname{Im}[A_n w_n^{\gamma-2}]\}, \\ t_{21} &= -\frac{4\gamma\dot{K}}{3\sqrt{\pi}} (\gamma - 1) \sum_{n=1}^2 \{\chi \operatorname{Re}[A_n w_n^{\gamma-2}] + (-1)^n \delta \operatorname{Im}[A_n w_n^{\gamma-2}]\}, \\ \dot{p} &= \frac{4\gamma\dot{K}}{3\sqrt{\pi}} (\gamma - 1) \sum_{n=1}^2 \{(-1)^n \alpha [2(1-k)\beta^2 + k] \operatorname{Re}[A_n w_n^{\gamma-2}] \\ &\quad + \beta [2(1-k)\alpha^2 - k] \operatorname{Im}[A_n w_n^{\gamma-2}]\}, \end{aligned} \quad (4.12)$$

where coefficients  $\chi, \delta$  depend on the prestress and on the incremental moduli through the eqn. (3.25).

**Mode I** Through eqn. (2.43) and the definition (4.9) of  $w_j$ , Mode I symmetry conditions (4.4) write

$$v_1(w_1, w_2) = v_1(\bar{w}_2, \bar{w}_1), \quad v_2(w_1, w_2) = -v_2(\bar{w}_2, \bar{w}_1), \quad (4.13)$$

which imply

$$A_n = (-1)^n a + ib \quad n = 1, 2, \quad (4.14)$$

where  $a$  and  $b$  are real constants. The boundary conditions (4.2) on the rigid line inclusion ( $\vartheta = \pi$  or, equivalently,  $\vartheta_n = \pi$ ) lead to the following homogeneous system for the constants  $a$  and  $b$ ,

$$\begin{bmatrix} \alpha \cos \gamma\pi & -\beta \cos \gamma\pi \\ 0 & \sin \gamma\pi \end{bmatrix} \begin{bmatrix} a \\ b \end{bmatrix} = \begin{bmatrix} 0 \\ 0 \end{bmatrix}. \quad (4.15)$$

Non-trivial solution for  $a$  and  $b$  of the system (4.15) exists if and only if the determinant of the associated matrix vanishes,

$$\alpha \sin(2\gamma\pi) = 0. \quad (4.16)$$

Note that  $\alpha$  vanishes when

$$\xi = \frac{1}{2} \left( 1 + \sqrt{1 - k^2} \right), \quad (4.17)$$

which represents the boundary between EI and EC domains (see eqn. (2.38)<sub>2</sub>). Therefore, within the EC regime and assuming boundedness of incremental energy, we find

$$\gamma = 3/2, \quad \rightsquigarrow \quad \dot{t} \sim \frac{1}{\sqrt{r}}, \quad (4.18)$$

similarly to the stiffener problem in classical linear elasticity. For this value of  $\gamma$ , eqn. (4.15)<sub>2</sub> gives

$$b = 0. \quad (4.19)$$

The asymptotic analysis is completed by expressing each variable appearing in (4.12) as a product of a term depending on the radius  $r$  with that describing the angular dependence around the rigid-line tip (variable  $\vartheta$ )

$$\mathbf{v}(r, \vartheta) = \frac{\dot{K}}{\mu} \sqrt{\frac{r}{2\pi}} \boldsymbol{\omega}(\vartheta), \quad \dot{\mathbf{t}}(r, \vartheta) = \frac{\dot{K}}{\sqrt{2\pi r}} \boldsymbol{\tau}(\vartheta), \quad \dot{p}(r, \vartheta) = \frac{\dot{K}}{\sqrt{2\pi r}} \rho(\vartheta). \quad (4.20)$$

Since the constants  $\dot{K}$  remains undetermined in an asymptotic analysis, it is expedient now to introduce a normalization. The definition (3.44) of incremental stress intensity factors used for the crack problem becomes unpractical in the present context. In fact,  $\tau_{22}(0)$  (and  $\tau_{21}(0)$  for Mode II) vanishes for

$$\eta = 1 - \sqrt{1 - k^2}, \quad (4.21)$$

indicated by a dashed curve in Fig. 4.3 (note that  $\tau_{22}(0) = 0$  –and  $\tau_{21}(0) = 0$  for Mode II– even in the case when the prestress is zero).<sup>9</sup>

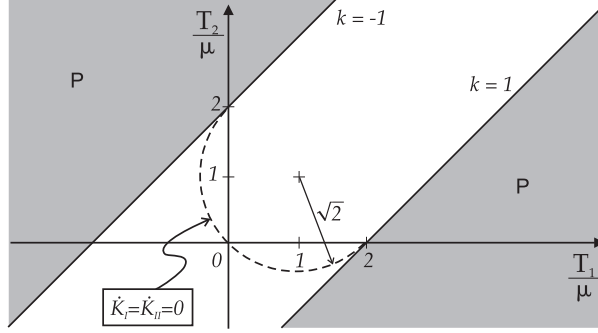


Figure 4.3: Line (dashed) of points, eqn. (4.21), where the incremental stress intensity factors (3.44) vanish simultaneously for Mode I and Mode II ( $\dot{K}_I = \dot{K}_{II} = 0$ ) in the prestress plane  $T_1/\mu - T_2/\mu$ . The white zone denotes the elliptic and the hyperbolic (EI  $\cup$  EC  $\cup$  H) regimes, while the grey zones refer to the parabolic (P) regime.

Therefore, since  $\omega_{2,2}$  (or  $\omega_{2,1}$ ) never vanishes (under the assumption that  $\alpha \neq 0$ ) for Mode I (or for Mode II), we follow the suggestion by Wu (1990) and introduce the definition

$$\dot{K}_{(\epsilon)I} = \lim_{r \rightarrow 0} 2\mu \sqrt{2\pi r} v_{2,2}(r, \vartheta = 0), \quad \dot{K}_{(\epsilon)II} = \lim_{r \rightarrow 0} 2\mu \sqrt{2\pi r} v_{2,1}(r, \vartheta = 0), \quad (4.23)$$

yielding for Mode I the representation

$$\mathbf{v}(r, \vartheta) = \frac{\dot{K}_{(\epsilon)I}}{\mu} \sqrt{\frac{r}{2\pi}} \boldsymbol{\omega}(\vartheta), \quad \mathbf{t}(r, \vartheta) = \frac{\dot{K}_{(\epsilon)I}}{\sqrt{2\pi r}} \boldsymbol{\tau}(\vartheta), \quad \dot{p}(r, \vartheta) = \frac{\dot{K}_{(\epsilon)I}}{\sqrt{2\pi r}} \rho(\vartheta). \quad (4.24)$$

<sup>9</sup>Note that condition (4.21) does not satisfy the Hill exclusion condition (2.20)<sub>2</sub>, in fact when (4.21) holds then

$$\frac{k^2 + \eta^2}{2\eta} = 1. \quad (4.22)$$

The relation between the definitions (4.23) of incremental stress intensity factors and the energy release rate is obtained in §4.4 and it is shown to be particularly convenient from a mathematical point of view.

The components of the angular functions defined in (4.24) for a generic Mode I symmetry assume the following analytical expressions valid for  $\vartheta \in [0, \pi]$ ,

$$\begin{aligned}
\omega_1(\vartheta) &= 2a \sum_{n=1}^2 [\alpha c_n(\vartheta) - (-1)^n \beta s_n(\vartheta)], \\
\omega_2(\vartheta) &= -2a \sum_{n=1}^2 (-1)^n c_n(\vartheta), \\
\tau_{11}(\vartheta) &= a \sum_{n=1}^2 [(\beta\delta + \chi\alpha)\hat{c}_n(\vartheta) - (-1)^n(\alpha\delta - \chi\beta)\hat{s}_n(\vartheta)], \\
\tau_{22}(\vartheta) &= a \sum_{n=1}^2 [(\beta\delta - \chi\alpha)\hat{c}_n(\vartheta) - (-1)^n(\alpha\delta + \chi\beta)\hat{s}_n(\vartheta)], \\
\tau_{12}(\vartheta) &= -a \sum_{n=1}^2 [(-1)^n(\chi\beta^2 - \chi\alpha^2 + 2\alpha\beta\delta)\hat{c}_n(\vartheta) \\
&\quad - (\delta\alpha^2 - \delta\beta^2 + 2\alpha\beta\chi)\hat{s}_n(\vartheta)], \\
\tau_{21}(\vartheta) &= -a \sum_{n=1}^2 [(-1)^n\chi\hat{c}_n(\vartheta) - \delta\hat{s}_n(\vartheta)], \\
\rho(\vartheta) &= a \sum_{n=1}^2 \{\alpha[2(1-k)\beta^2 + k]\hat{c}_n(\vartheta) - (-1)^n\beta[2(1-k)\alpha^2 - k]\hat{s}_n(\vartheta)\},
\end{aligned} \tag{4.25}$$

where the following angular functions have been introduced

$$\begin{aligned}
g_n(\vartheta) &= \sqrt{[\cos \vartheta + (-1)^n \alpha \sin \vartheta]^2 + \beta^2 \sin^2 \vartheta}, \\
c_n(\vartheta) &= \sqrt{g_n(\vartheta) + \cos \vartheta + (-1)^n \alpha \sin \vartheta}, & \hat{c}_n(\vartheta) &= \frac{c_n(\vartheta)}{g_n(\vartheta)}, \\
s_n(\vartheta) &= \sqrt{g_n(\vartheta) - \cos \vartheta - (-1)^n \alpha \sin \vartheta}, & \hat{s}_n(\vartheta) &= \frac{s_n(\vartheta)}{g_n(\vartheta)}.
\end{aligned} \tag{4.26}$$

The definition (4.23)<sub>1</sub> of  $\dot{K}_{(\epsilon)I}$  introduces the normalization condition

$$\left. \frac{d\omega_2(\vartheta)}{d\vartheta} \right|_{\vartheta=0} = 2, \quad (4.27)$$

leading to the following expression,

$$a = -\frac{1}{4\sqrt{2}\alpha}. \quad (4.28)$$

**Mode II** Through eqn. (2.43) and the definition (4.9) of  $w_j$ , Mode II symmetry conditions (4.5) write

$$v_1(w_1, w_2) = -v_1(\bar{w}_2, \bar{w}_1), \quad v_2(w_1, w_2) = v_2(\bar{w}_2, \bar{w}_1), \quad (4.29)$$

which imply

$$A_n = -a - (-1)^n i b \quad n = 1, 2, \quad (4.30)$$

being  $a$  and  $b$  real constants. The boundary conditions (4.2) yield the homogeneous linear problem

$$\begin{bmatrix} \beta \sin \gamma \pi & \alpha \sin \gamma \pi \\ \cos \gamma \pi & 0 \end{bmatrix} \begin{bmatrix} a \\ b \end{bmatrix} = \begin{bmatrix} 0 \\ 0 \end{bmatrix}, \quad (4.31)$$

that leads, again, to (4.16). For  $\gamma = 3/2$ , eqn. (4.31)<sub>1</sub> defines a constraint on the constants  $a$  and  $b$ ,

$$b = -\frac{\beta}{\alpha}a. \quad (4.32)$$

Analogously to Mode I, the asymptotic fields may be represented as a product between the Mode II incremental stress intensity factor  $\dot{K}_{(\epsilon)II}$  (eqn. (4.23)<sub>2</sub>) and two functions depending on  $r$  and  $\vartheta$ , respectively as

$$\mathbf{v}(r, \vartheta) = \frac{\dot{K}_{(\epsilon)II}}{\mu} \sqrt{\frac{r}{2\pi}} \boldsymbol{\omega}(\vartheta), \quad \mathbf{t}(r, \vartheta) = \frac{\dot{K}_{(\epsilon)II}}{\sqrt{2\pi r}} \boldsymbol{\tau}(\vartheta), \quad \dot{p}(r, \vartheta) = \frac{\dot{K}_{(\epsilon)II}}{\sqrt{2\pi r}} \rho(\vartheta), \quad (4.33)$$

where  $\omega(\vartheta)$ ,  $\tau(\vartheta)$  and  $\rho(\vartheta)$  assume, in the range  $\vartheta \in [0, \pi]$ , the form

$$\begin{aligned}
\omega_1(\vartheta) &= -2a \frac{\alpha^2 + \beta^2}{\alpha} \sum_{n=1}^2 (-1)^n c_n(\vartheta), \\
\omega_2(\vartheta) &= 2a \frac{1}{\alpha} \sum_{n=1}^2 [\alpha c_n(\vartheta) + (-1)^n \beta s_n(\vartheta)], \\
\tau_{11}(\vartheta) &= a \frac{\alpha^2 + \beta^2}{\alpha} \sum_{n=1}^2 [ -(-1)^n \chi \hat{c}_n(\vartheta) + \delta \hat{s}_n(\vartheta) ], \\
\tau_{22}(\vartheta) &= a \frac{\alpha^2 + \beta^2}{\alpha} \sum_{n=1}^2 [ (-1)^n \chi \hat{c}_n(\vartheta) + \delta \hat{s}_n(\vartheta) ], \\
\tau_{12}(\vartheta) &= -a \frac{\alpha^2 + \beta^2}{\alpha} \sum_{n=1}^2 [ (\alpha \chi - \beta \delta) \hat{c}_n(\vartheta) + (-1)^n (\alpha \delta + \beta \chi) \hat{s}_n(\vartheta) ], \\
\tau_{21}(\vartheta) &= -a \frac{1}{\alpha} \sum_{n=1}^2 [ -(\alpha \chi - \beta \delta) \hat{c}_n(\vartheta) + (-1)^n (\alpha \delta + \beta \chi) \hat{s}_n(\vartheta) ], \\
\rho(\vartheta) &= a \frac{\alpha^2 + \beta^2}{\alpha} \sum_{n=1}^2 [ -(-1)^n k \hat{c}_n(\vartheta) + \delta \hat{s}_n(\vartheta) ].
\end{aligned} \tag{4.34}$$

The normalization condition,

$$\omega_2(0) = 4, \tag{4.35}$$

now fixes the constant  $a$  to be

$$a = \frac{1}{4\sqrt{2}}. \tag{4.36}$$

### Elliptic imaginary regime

Roots  $\Omega_j$  ( $j = 1, \dots, 4$ ) take the form (2.40) in the EI regime. The asymptotic expansions of the incremental quantities may be obtained by substituting the expression of the stream function (4.8)<sub>2</sub> in eqns. (2.30), (2.6), and (2.29) (see

also Radi et al. 2002) to yield

$$\begin{aligned}
v_1 &= -\frac{4\gamma\dot{K}}{3\mu\sqrt{\pi}} \sum_{n=1}^2 \beta_n \operatorname{Im}[A_n w_n^{\gamma-1}], \\
v_2 &= -\frac{4\gamma\dot{K}}{3\mu\sqrt{\pi}} \sum_{n=1}^2 \operatorname{Re}[A_n w_n^{\gamma-1}], \\
t_{11} &= -\frac{4\gamma\dot{K}}{3\sqrt{\pi}} (\gamma-1) \sum_{n=1}^2 \varepsilon_n \beta_n \operatorname{Im}[A_n w_n^{\gamma-2}], \\
t_{22} &= \frac{4\gamma\dot{K}}{3\sqrt{\pi}} (\gamma-1) \sum_{n=1}^2 \chi_n \beta_n \operatorname{Im}[A_n w_n^{\gamma-2}], \\
t_{12} &= -\frac{4\gamma\dot{K}}{3\sqrt{\pi}} (\gamma-1) \sum_{n=1}^2 \chi_n \beta_n^2 \operatorname{Re}[A_n w_n^{\gamma-2}], \\
t_{21} &= -\frac{4\gamma\dot{K}}{3\sqrt{\pi}} (\gamma-1) \sum_{n=1}^2 \varepsilon_n \operatorname{Re}[A_n w_n^{\gamma-2}], \\
\dot{p} &= \frac{4\gamma\dot{K}}{3\sqrt{\pi}} (\gamma-1) \sum_{n=1}^2 \delta_n \beta_n \operatorname{Im}[A_n w_n^{\gamma-2}],
\end{aligned} \tag{4.37}$$

where  $\varepsilon_n$  and  $\delta_n$  are defined by eqns. (3.17) and (3.22), respectively, and

$$\chi_n = 4\xi - 1 - \eta - (1-k)\beta_n^2, \quad n = 1, 2. \tag{4.38}$$

**Mode I** Through eqn. (2.40) and the definition (4.9) of  $w_j$ , Mode I symmetry conditions (4.4) write

$$v_1(w_1, w_2) = v_1(\bar{w}_1, \bar{w}_2), \quad v_2(w_1, w_2) = -v_2(\bar{w}_1, \bar{w}_2), \tag{4.39}$$

which imply

$$a_1 = a_2 = 0, \tag{4.40}$$

so that

$$A_n = ib_n, \quad n = 1, 2. \tag{4.41}$$

The boundary conditions (4.2), applied for  $\vartheta_n = \pi$ , provide the homogeneous system,

$$\begin{bmatrix} \beta_1 \cos \gamma\pi & \beta_2 \cos \gamma\pi \\ \sin \gamma\pi & \sin \gamma\pi \end{bmatrix} \begin{bmatrix} b_1 \\ b_2 \end{bmatrix} = \begin{bmatrix} 0 \\ 0 \end{bmatrix}, \tag{4.42}$$

which (for  $\beta_1 \neq \beta_2$ ) admits a non-trivial solution if and only if  $\gamma$  is  $3/2$ . Note that the condition  $\beta_1 \neq \beta_2$  corresponds to eqn. (4.17), which sets the boundary between the two elliptic regimes (see eqn. (2.38)<sub>2</sub>). For  $\gamma = 3/2$ , the relation

$$b_1 + b_2 = 0, \quad (4.43)$$

is obtained from eqn. (4.42)<sub>2</sub>.

The components of the angular functions defined by eqns. (4.24) for a generic Mode I take the following analytic expressions, valid for  $\vartheta \in [0, \pi]$ ,

$$\begin{aligned} \omega_1(\vartheta) &= -2 \sum_{n=1}^2 b_n \beta_n \sqrt{g_n(\vartheta) + \cos \vartheta}, \\ \omega_2(\vartheta) &= 2 \sum_{n=1}^2 b_n \sqrt{g_n(\vartheta) - \cos \vartheta}, \\ \tau_{11}(\vartheta) &= - \sum_{n=1}^2 b_n \varepsilon_n \beta_n \sqrt{g_n(\vartheta) + \cos \vartheta} / g_n(\vartheta), \\ \tau_{22}(\vartheta) &= \sum_{n=1}^2 b_n \chi_n \beta_n \sqrt{g_n(\vartheta) + \cos \vartheta} / g_n(\vartheta), \\ \tau_{12}(\vartheta) &= - \sum_{n=1}^2 b_n \chi_n \beta_n^2 \sqrt{g_n(\vartheta) - \cos \vartheta} / g_n(\vartheta), \\ \tau_{21}(\vartheta) &= - \sum_{n=1}^2 b_n \varepsilon_n \sqrt{g_n(\vartheta) - \cos \vartheta} / g_n(\vartheta), \\ \rho(\vartheta) &= \sum_{n=1}^2 b_n \delta_n \beta_n \sqrt{g_n(\vartheta) + \cos \vartheta} / g_n(\vartheta), \end{aligned} \quad (4.44)$$

where

$$g_n(\vartheta) = \sqrt{\cos^2 \vartheta + \beta_n^2 \sin^2 \vartheta}. \quad (4.45)$$

The normalization condition (4.27) provides  $b_1$  and  $b_2$  as

$$b_n = \frac{1}{2\sqrt{2}(\beta_n - \beta_m)} \quad n, m = 1, 2, \quad m \neq n. \quad (4.46)$$

where the equalities

$$\varepsilon_n = \chi_m, \quad n, m = 1, 2, \quad m \neq n, \quad (4.47)$$

obtained from eqns. (3.17) and (4.38), have been used.

**Mode II** Through eqns. (2.40) and the definition (4.9) of  $w_j$ , Mode II symmetry conditions (4.5) write

$$v_1(w_1, w_2) = -v_1(\bar{w}_1, \bar{w}_2), \quad v_2(w_1, w_2) = v_2(\bar{w}_1, \bar{w}_2), \quad (4.48)$$

that imply

$$b_1 = b_2 = 0, \quad (4.49)$$

and, as a consequence,

$$A_n = a_n, \quad n = 1, 2. \quad (4.50)$$

The boundary conditions provide the homogeneous system

$$\begin{bmatrix} \beta_1 \sin \gamma\pi & \beta_2 \sin \gamma\pi \\ \cos \gamma\pi & \cos \gamma\pi \end{bmatrix} \begin{bmatrix} a_1 \\ a_2 \end{bmatrix} = \begin{bmatrix} 0 \\ 0 \end{bmatrix}, \quad (4.51)$$

which admits non-trivial solution for  $\gamma = 3/2$  and defines the constraint

$$a_1\beta_1 + a_2\beta_2 = 0. \quad (4.52)$$

The functions defined by eqns. (4.33), valid for  $\vartheta \in [0, \pi]$ , now become

$$\begin{aligned} \omega_1(\vartheta) &= -2 \sum_{n=1}^2 a_n \beta_n \sqrt{g_n(\vartheta) - \cos \vartheta}, \\ \omega_2(\vartheta) &= -2 \sum_{n=1}^2 a_n \sqrt{g_n(\vartheta) + \cos \vartheta}, \\ \tau_{11}(\vartheta) &= \sum_{n=1}^2 a_n \varepsilon_n \beta_n \sqrt{g_n(\vartheta) - \cos \vartheta} / g_n(\vartheta), \\ \tau_{22}(\vartheta) &= - \sum_{n=1}^2 a_n \chi_n \beta_n \sqrt{g_n(\vartheta) - \cos \vartheta} / g_n(\vartheta), \\ \tau_{12}(\vartheta) &= - \sum_{n=1}^2 a_n \chi_n \beta_n^2 \sqrt{g_n(\vartheta) + \cos \vartheta} / g_n(\vartheta), \\ \tau_{21}(\vartheta) &= - \sum_{n=1}^2 a_n \varepsilon_n \sqrt{g_n(\vartheta) + \cos \vartheta} / g_n(\vartheta), \\ \rho(\vartheta) &= - \sum_{n=1}^2 a_n \delta_n \beta_n \sqrt{g_n(\vartheta) - \cos \vartheta} / g_n(\vartheta). \end{aligned} \quad (4.53)$$

From the normalization condition (4.35) we obtain the following condition,

$$a_n = \frac{\beta_m}{2\sqrt{2}(\beta_n - \beta_m)} \quad n, m = 1, 2, \quad m \neq n. \quad (4.54)$$

### 4.1.2 The strange failure modes near a stiffener in a brittle material

The analysis of the near-tip asymptotic fields reveals interesting features, deserving a detailed description, confined here to Mode I loading, eqns. (4.44). In particular, let us start with the angular distribution of Mode I asymptotic near-tip fields, represented in Fig. 4.4 for a Mooney-Rivlin material,  $\xi = 1$  at different levels of prestress  $k = \{-0.4, 0, 0.4\}$ . The values  $k = \pm 0.4$  are sufficiently far from the EI/P boundary, which is attained by a Mooney-Rivlin material at an infinite stretch, when  $k = \pm 1$ . The value  $k = 0$  pertains to the case of the isotropic incompressible elasticity with null prestress.

The normalization (4.23) is used, so that the loading is given by an incremental dilatation orthogonal to the stiffener  $v_{2,2} > 0$  (which, due to incompressibility, is equivalent to a contraction parallel to the stiffener). We may note from the figure that the angular distribution is not affected much by prestress, except that the two nominal shear stresses separate and that the radial stress always remains negative for  $k = 0.4$ .

Interestingly, compressive stresses dominate and, in particular, the hoop stress is always negative for  $k > 0$ . Therefore, assuming that *the material is brittle, in the sense that it fails when the maximum principal tensile stress reaches a limit value*, we note that:

- *the maximum hoop-stress criterion (Erdogan and Sih, 1963) does not work;*
- *failure will not occur with a fracture aligned parallel to the stiffener, even when this is subject to a Mode I loading.*

For simplicity, let us focus on the situation without prestress ( $k = 0$ ) and assume that the matrix material is brittle, therefore failing in agreement with a maximum principal stress criterion (so that obviously the following considerations will depend on these assumptions). The maximum principal stress is attained at the stiffener line ( $\vartheta = \pi$ ) and is inclined at  $\pi/4$  (Fig. 4.5, left). In this case, the failure mode is not easy to be envisaged. Our interpretation is that:

*a crack starts on the surface of the inclusion inclined at  $\pi/4$  (orthogonal to the principal, near-tip tensile direction) and then immediately the stiffener delaminates and the crack propagates under opening mode (orthogonally to the loading direction);*

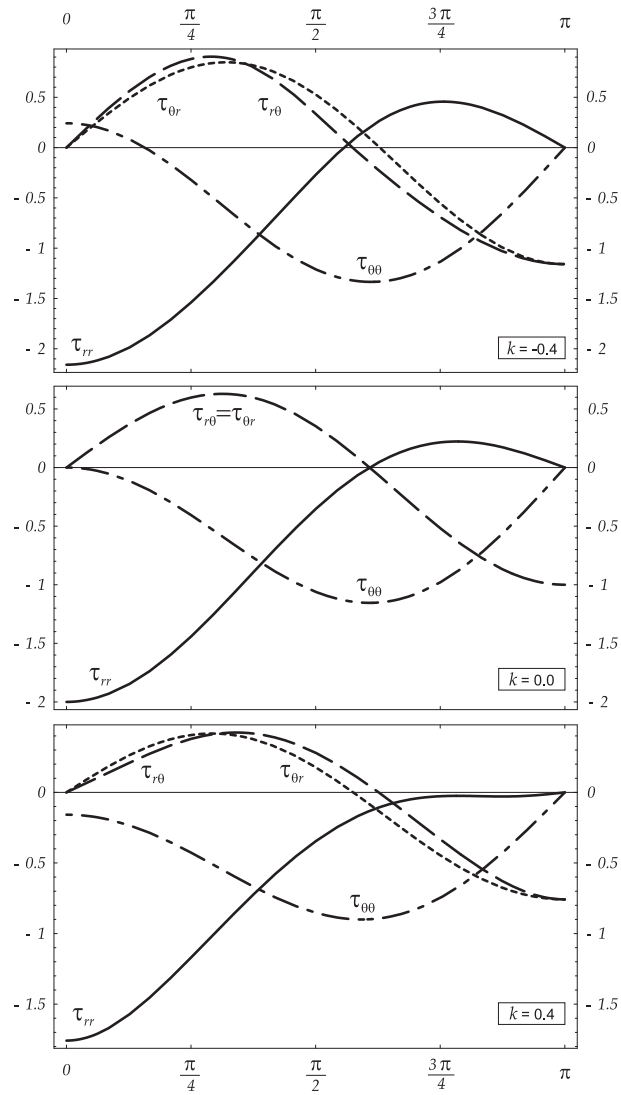


Figure 4.4: Angular representation of asymptotic Mode I stress field near the tip of a stiffener in an incompressible, elastic Mooney-Rivlin material at different levels of prestress  $k$ .

this situation has been in fact observed in one of our experiments, see appendix A and Fig. 4.7.

If now a dilatation parallel to the stiffener is considered,  $v_{1,1} > 0$  (Fig. 4.5,

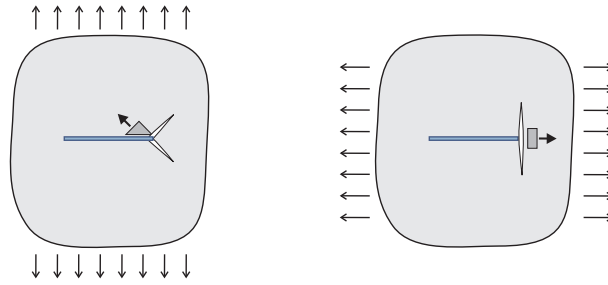


Figure 4.5: Sketch of the predicted fracture modes for a stiffener embedded in an isotropic, not prestressed, brittle matrix (where cracks develop orthogonally to the maximum tensile stress), subject to orthogonal (left) and parallel (right) dilatation. Compare the failure mode shown on the left with Fig. 4.7, that shown on the right with Fig. 1.3 and Fig. 4.6.

right), all signs of the stresses reverse in the graphs reported in Fig. 4.4 and we may understand that

*failure occurs due to the maximum radial stress,*

which is the maximum near-tip principal tensile stress.

The fracture patterns sketched in Fig. 4.5 have been confirmed by three experiments. In particular, fractures similar to that shown in Fig. 4.5 (right) have been found in samples S2, S1, reported in Figs. 1.3 and 4.6, respectively. Fractures similar to that shown in Fig. 4.5 (left) have been found in sample S4, see Fig. 4.7.

Until now we have investigated a brittle matrix material, so that a moderate prestress has been considered and its effects have been shown to be relatively limited. However, ductile materials can be subject to severe prestress and its effects become dramatic when the prestress parameter approaches the value for ellipticity loss and in this case near-tip localized deformations emerge, a situation that completely changes the failure modes (§4.1.5).

### 4.1.3 Full-field solution for a uniform incremental Mode I at infinity

The full-field solution is obtained for the problem where a uniformly prestressed, infinite plane containing a stiffener of length  $2l$  (aligned parallel to the principal stress directions) is subject to remote incremental loading, with prescribed incremental displacement gradient. In particular, the non-null far-field stress components  $t_{11}^{\infty}$  and  $t_{22}^{\infty}$  are prescribed (respectively, along

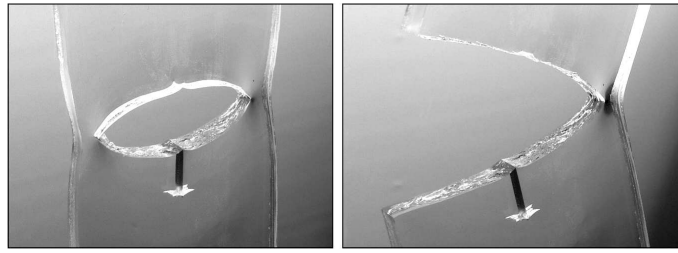


Figure 4.6: Progressive fracture of sample S1 subject to a tensile load directed parallel the inclusion (photo taken at the University of Trento, experiment performed by G. Noselli). Note that there are two fractures, one at the upper tip and another, much less developed, at the lower tip of the aluminum lamina.

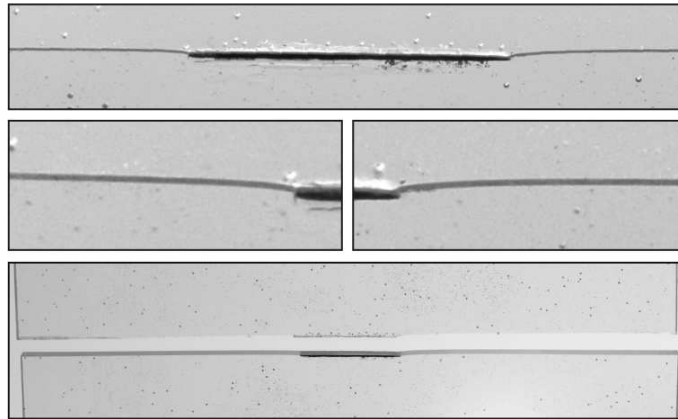


Figure 4.7: Fracture mode of sample S4 subject to a tensile load orthogonal to the inclusion. The aluminum lamina is visible in the upper part, while the two near-tip details are shown in the central part. A ‘post-mortem’ view of the fracture is shown in the lower part, where the two pieces of the sample have been separated. Note the initial inclinations (approximately  $\pi/4$ ) of the fractures near the aluminum lamina tips (photos taken at the University of Trento, experiment performed by G. Noselli).

directions  $x_1$  and  $x_2$ , Fig. 4.1 with  $\vartheta_0 = 0$ ), corresponding to a type of Mode I loading. Mode II will not be considered since a stiffener aligned parallel to axis  $x_1$  does not perturb a uniform incremental shear parallel to the axes (a fact that can be intuitively appreciated thinking about a shearing deformation of a deck of cards and its associated strain ellipses, see Appendix C.2).

Taking  $2\xi \neq \eta$  for simplicity, the constitutive equations (2.6) allow us to

relate the displacement gradient and the incremental pressure in the form

$$\begin{aligned} v_{1,1}^\infty = -v_{2,2}^\infty &= \frac{t_{11}^\infty - t_{22}^\infty}{2\mu(2\xi - \eta)}, & v_{1,2}^\infty = v_{2,1}^\infty &= 0, \\ \dot{p}^\infty &= \frac{t_{11}^\infty(2\xi + k - \eta) + t_{22}^\infty(2\xi - k - \eta)}{2(2\xi - \eta)}, \end{aligned} \quad (4.55)$$

so that we can equivalently prescribe remote incremental nominal stresses ( $t_{ij}^\infty$ ) instead of incremental displacement gradient components ( $v_{i,j}^\infty$ ).

Similarly to the crack problem (§3.1), we solve the perturbed problem introducing a stream function, eqn. (3.8), so that eqns. (3.9)-(3.11) follow.

To recover the constraint introduced by the stiffener, eqns. (4.2), the displacement gradient components  $v_{1,1}$  and  $v_{2,1}$ , of opposite sign to that imposed at infinity, are applied on the line representing the lamellar inclusion, namely<sup>10</sup>

$$\begin{aligned} (-v_{1,1}^\circ(x_1, 0^\pm) =) v_{2,2}^\circ(x_1, 0^\pm) &= -v_{2,2}^\infty \quad \forall |x_1| < l, \\ v_{2,1}^\circ(x_1, 0^\pm) = -v_{2,1}^\infty(x_1, 0^\pm) &= 0, \quad \forall x_1 \in \mathbb{R}, \end{aligned} \quad (4.56)$$

where apices + and - denote the upper and lower stiffener surface, respectively.

Moreover, eqns. (4.56)<sub>2</sub> and (3.9)<sub>2</sub> provide

$$v_{2,1}^\circ(x_1, 0) = -\frac{F_1^{\prime\prime+}(x_1) - F_1^{\prime\prime-}(x_1)}{2} - \frac{F_2^{\prime\prime+}(x_1) - F_2^{\prime\prime-}(x_1)}{2} = 0, \quad \forall x_1 \in \mathbb{R}, \quad (4.57)$$

which yields the key property

$$(F_1^{\prime\prime}(x_1) + F_2^{\prime\prime}(x_1))^+ = (F_1^{\prime\prime}(x_1) + F_2^{\prime\prime}(x_1))^- , \quad \forall x_1 \in \mathbb{R}. \quad (4.58)$$

Condition (4.58) implies that the function  $F_1^{\prime\prime}(x_1) + F_2^{\prime\prime}(x_1)$  is continuous across the branch cut ( $|x_1| < l, x_2 = 0$ ), so that it results analytic in the whole  $Ox_1x_2$  plane, and, assuming also boundedness, it results constant from Liouville's theorem. Such a constant is zero since at infinity the function must be zero, see eqn. (3.11). As a conclusion, we obtain

$$F_1^{\prime\prime}(x_1) = -F_2^{\prime\prime}(x_1), \quad \forall x_1 \in \mathbb{R}. \quad (4.59)$$

The set of equation (4.59), plus (2.40), (2.43), and (3.9) allow us to represent function  $v_{1,1}^\circ$  in the form

$$v_{1,1}^\circ(x_1, 0) = -2\alpha \operatorname{Re} [F_1^{\prime\prime}(x_1)] + (\beta_1 - \beta_2) \operatorname{Re} [iF_1^{\prime\prime}(x_1)], \quad \forall |x_1| < l, \quad (4.60)$$

<sup>10</sup>Note that, due to Mode I symmetry,  $v_{2,11} = 0$  is equivalent to  $v_{2,1} = \omega_S = 0$ .

so that condition (4.56)<sub>1</sub> takes the form

$$-2\alpha \operatorname{Re} [F_1''(x_1)] + (\beta_1 - \beta_2) \operatorname{Re} [iF_1''(x_1)] = v_{2,2}^{(\infty)}, \quad \forall |x_1| < l. \quad (4.61)$$

### Elliptic complex regime

In the elliptic complex regime,  $\beta_1 = \beta_2$ , so that eqn. (4.61) simplifies to

$$-2\alpha \operatorname{Re} [F_1''(x_1)] = v_{2,2}^{(\infty)} \quad \forall |x_1| < l. \quad (4.62)$$

The following Riemann-Hilbert problem can be formulated for function  $F_1''(z)$ , i.e.

$$F_1''^+(x_1) + F_1''^-(x_1) = -\frac{v_{2,2}^{(\infty)}}{\alpha} \quad \forall |x_1| < l, \quad (4.63)$$

whose solution is given by (Muskhelishvili, 1953, §110) in the form

$$F_1''(z_1) = -\frac{v_{2,2}^{(\infty)}}{2\alpha\sqrt{z_1^2 - l^2}} \left[ \frac{1}{2\pi i} \int_{-l}^l \frac{\sqrt{t^2 - l^2}}{t - z_1} dt + P(z_1) \right], \quad (4.64)$$

where  $P(z_1)$  is a polynomial that must be zero for the condition (3.11). The solution is

$$F_1''(z_1) = -\frac{v_{2,2}^{(\infty)}}{2\alpha} \left( 1 - \frac{z_1}{\sqrt{z_1^2 - l^2}} \right), \quad (4.65)$$

and through eqn. (4.59)

$$F_2''(z_2) = \frac{v_{2,2}^{(\infty)}}{2\alpha} \left( 1 - \frac{z_2}{\sqrt{z_2^2 - l^2}} \right). \quad (4.66)$$

By integration, eqn. (3.8)<sub>1</sub> provides  $\psi^{(\circ)}$  within the EC regime. In this regime, the stream function  $\psi$  writes

$$\begin{aligned} \psi = \psi^{(\circ)} + \psi^{(\infty)} &= -\frac{v_{2,2}^{(\infty)}}{4\alpha} \left\{ \operatorname{Re} \left[ \beta^2 \frac{z_1^2 - z_2^2}{\alpha^2 + \beta^2} - z_1 \sqrt{z_1^2 - l^2} + z_2 \sqrt{z_2^2 - l^2} \right. \right. \\ &\quad \left. \left. + l^2 \ln \left( \frac{z_1 + \sqrt{z_1^2 - l^2}}{z_2 + \sqrt{z_2^2 - l^2}} \right) \right] + \operatorname{Im} \left[ \alpha \beta \frac{z_1^2 + z_2^2}{\alpha^2 + \beta^2} \right] \right\}. \end{aligned} \quad (4.67)$$

The incremental displacement field and its gradient can be calculated from eqns. (2.30) and are

$$\begin{aligned}
v_1 &= -\frac{v_{2,2}^{(\infty)}}{2\alpha} \left\{ \alpha \operatorname{Re} \left[ \sqrt{z_1^2 - l^2} + \sqrt{z_2^2 - l^2} \right] \right. \\
&\quad \left. - \beta \operatorname{Im} \left[ z_1 - z_2 - \left( \sqrt{z_1^2 - l^2} - \sqrt{z_2^2 - l^2} \right) \right] \right\}, \\
v_2 &= \frac{v_{2,2}^{(\infty)}}{2\alpha} \left\{ \operatorname{Re} \left[ \beta^2 \frac{z_1 - z_2}{\alpha^2 + \beta^2} - \left( \sqrt{z_1^2 - l^2} - \sqrt{z_2^2 - l^2} \right) \right] + \alpha\beta \operatorname{Im} \left[ \frac{z_1 + z_2}{\alpha^2 + \beta^2} \right] \right\}, \\
v_{1,1} &= -\frac{v_{2,2}^{(\infty)}}{2\alpha} \left\{ \alpha \operatorname{Re} \left[ \frac{z_1}{\sqrt{z_1^2 - l^2}} + \frac{z_2}{\sqrt{z_2^2 - l^2}} \right] \right. \\
&\quad \left. + \beta \operatorname{Im} \left[ \frac{z_1}{\sqrt{z_1^2 - l^2}} - \frac{z_2}{\sqrt{z_2^2 - l^2}} \right] \right\} = -v_{2,2}, \\
v_{1,2} &= \frac{v_{2,2}^{(\infty)}}{2\alpha} \left\{ (\alpha^2 - \beta^2) \operatorname{Re} \left[ \frac{z_1}{\sqrt{z_1^2 - l^2}} - \frac{z_2}{\sqrt{z_2^2 - l^2}} \right] \right. \\
&\quad \left. + 2\alpha\beta \operatorname{Im} \left[ \frac{z_1}{\sqrt{z_1^2 - l^2}} + \frac{z_2}{\sqrt{z_2^2 - l^2}} \right] \right\}, \\
v_{2,1} &= -\frac{v_{2,2}^{(\infty)}}{2\alpha} \operatorname{Re} \left[ \frac{z_1}{\sqrt{z_1^2 - l^2}} - \frac{z_2}{\sqrt{z_2^2 - l^2}} \right].
\end{aligned} \tag{4.68}$$

Eqns. (2.6) and (2.29) provide the incremental nominal stress field in the form

$$\begin{aligned}
\dot{p} &= \dot{p}^{(\infty)} - \frac{\mu v_{2,2}^{(\infty)}}{2\alpha} \left\{ -\alpha[2(1-k)\beta^2 + k] \operatorname{Re} \left[ 2 - \frac{z_1}{\sqrt{z_1^2 - l^2}} - \frac{z_2}{\sqrt{z_2^2 - l^2}} \right] \right. \\
&\quad \left. - \beta[2(1-k)\alpha^2 - k] \operatorname{Im} \left[ \frac{z_1}{\sqrt{z_1^2 - l^2}} - \frac{z_2}{\sqrt{z_2^2 - l^2}} \right] \right\},
\end{aligned} \tag{4.69}$$

$$\begin{aligned}
t_{11} &= \dot{p}^{(\infty)} - \frac{\mu v_{2,2}^{(\infty)}}{2\alpha} \left\{ (\beta\delta + \chi\alpha) \operatorname{Re} \left[ \frac{z_1}{\sqrt{z_1^2 - l^2}} + \frac{z_2}{\sqrt{z_2^2 - l^2}} \right] \right. \\
&\quad \left. - (\alpha\delta - \chi\beta) \operatorname{Im} \left[ \frac{z_1}{\sqrt{z_1^2 - l^2}} - \frac{z_2}{\sqrt{z_2^2 - l^2}} \right] - 2\alpha[2(1-k)\beta^2 + k] \right\}, \\
t_{22} &= \dot{p}^{(\infty)} - \frac{\mu v_{2,2}^{(\infty)}}{2\alpha} \left\{ (\beta\delta - \chi\alpha) \operatorname{Re} \left[ \frac{z_1}{\sqrt{z_1^2 - l^2}} + \frac{z_2}{\sqrt{z_2^2 - l^2}} \right] \right. \\
&\quad \left. - (\alpha\delta + \chi\beta) \operatorname{Im} \left[ \frac{z_1}{\sqrt{z_1^2 - l^2}} - \frac{z_2}{\sqrt{z_2^2 - l^2}} \right] - 2\alpha[2(1-k)\beta^2 + k] \right\}, \\
t_{12} &= -\frac{\mu v_{2,2}^{(\infty)}}{2\alpha} \left\{ (\chi\beta^2 - \chi\alpha^2 + 2\alpha\beta\delta) \operatorname{Re} \left[ \frac{z_1}{\sqrt{z_1^2 - l^2}} - \frac{z_2}{\sqrt{z_2^2 - l^2}} \right] \right. \\
&\quad \left. - (\delta\alpha^2 - \delta\beta^2 + 2\alpha\beta\chi) \operatorname{Im} \left[ \frac{z_1}{\sqrt{z_1^2 - l^2}} + \frac{z_2}{\sqrt{z_2^2 - l^2}} \right] \right\}, \\
t_{21} &= -\frac{\mu v_{2,2}^{(\infty)}}{2\alpha} \left\{ \chi \operatorname{Re} \left[ \frac{z_1}{\sqrt{z_1^2 - l^2}} - \frac{z_2}{\sqrt{z_2^2 - l^2}} \right] - \delta \operatorname{Im} \left[ \frac{z_1}{\sqrt{z_1^2 - l^2}} + \frac{z_2}{\sqrt{z_2^2 - l^2}} \right] \right\},
\end{aligned}$$

where  $\dot{p}^{(\infty)}$  is given by eqn. (4.55)<sub>3</sub> and the parameters  $\chi$  and  $\delta$  are defined by eqns. (3.25).

### Elliptic imaginary regime

In the elliptic imaginary regime,  $\alpha = 0$ , so that eqn. (4.61) becomes

$$(\beta_1 - \beta_2) \operatorname{Re} [iF_1''(x_1)] = v_{2,2}^{(\infty)} \quad \text{if} \quad |x_1| < l, \quad (4.70)$$

providing the following Riemann-Hilbert problem in terms of  $F_1''(z)$

$$F_1''^+(x_1) + F_1''^-(x_1) = -i \frac{2v_{2,2}^{(\infty)}}{\beta_1 - \beta_2} \quad \text{if} \quad |x_1| < l. \quad (4.71)$$

The solution of eqn. (4.71) corresponds to

$$F_1''(z_1) = -i \frac{v_{2,2}^{(\infty)}}{\beta_1 - \beta_2} \left( 1 - \frac{z_1}{\sqrt{z_1^2 - l^2}} \right), \quad (4.72)$$

while eqn. (4.59) provides

$$F_2''(z_2) = i \frac{v_{2,2}^{(\infty)}}{\beta_1 - \beta_2} \left( 1 - \frac{z_2}{\sqrt{z_2^2 - l^2}} \right). \quad (4.73)$$

Analogously to the EC regime, the stream function  $\psi^{(\circ)}$  can be obtained integrating eqns. (4.72) and (4.73) and employing eqn. (3.8)<sub>2</sub>. This gives

$$\begin{aligned} \psi = \psi^{(\infty)} + \psi^{(\circ)} = & -\frac{v_{2,2}^{(\infty)}}{2(\beta_1 - \beta_2)} \operatorname{Im} \left[ (\beta_1 + \beta_2) \frac{\beta_1 z_2^2 - \beta_2 z_1^2}{2\beta_1 \beta_2} + z_1 \sqrt{z_1^2 - l^2} \right. \\ & \left. - z_2 \sqrt{z_2^2 - l^2} + l^2 \ln \left( \frac{z_2 + \sqrt{z_2^2 - l^2}}{z_1 + \sqrt{z_1^2 - l^2}} \right) \right]. \end{aligned} \quad (4.74)$$

The incremental displacement field and its gradient are

$$\begin{aligned} v_1 &= -\frac{v_{2,2}^{(\infty)}}{\beta_1 - \beta_2} \operatorname{Re} \left[ (\beta_1 + \beta_2) \frac{z_2 - z_1}{2} + \beta_1 \sqrt{z_1^2 - l^2} - \beta_2 \sqrt{z_2^2 - l^2} \right], \\ v_2 &= \frac{v_{2,2}^{(\infty)}}{\beta_1 - \beta_2} \operatorname{Im} \left[ (\beta_1 + \beta_2) \frac{\beta_1 z_2 - \beta_2 z_1}{2\beta_1 \beta_2} + \sqrt{z_1^2 - l^2} - \sqrt{z_2^2 - l^2} \right], \\ v_{1,1} &= -\frac{v_{2,2}^{(\infty)}}{\beta_1 - \beta_2} \operatorname{Re} \left[ \beta_1 \frac{z_1}{\sqrt{z_1^2 - l^2}} - \beta_2 \frac{z_2}{\sqrt{z_2^2 - l^2}} \right] = -v_{2,2}, \\ v_{1,2} &= \frac{v_{2,2}^{(\infty)}}{\beta_1 - \beta_2} \operatorname{Im} \left[ \beta_1^2 \frac{z_1}{\sqrt{z_1^2 - l^2}} - \beta_2^2 \frac{z_2}{\sqrt{z_2^2 - l^2}} \right], \\ v_{2,1} &= \frac{v_{2,2}^{(\infty)}}{\beta_1 - \beta_2} \operatorname{Im} \left[ \frac{z_1}{\sqrt{z_1^2 - l^2}} - \frac{z_2}{\sqrt{z_2^2 - l^2}} \right]. \end{aligned} \quad (4.75)$$

Eqns. (2.6) and (2.29) lead to the incremental nominal stress, whose components can be expressed in terms of parameters  $\varepsilon_n$  (3.17),  $\delta_n$  (3.22), and  $\chi_n$

(4.38) as

$$\begin{aligned}
\dot{p} &= \dot{p}^{(\infty)} - \frac{\mu v_{2,2}^{(\infty)}}{\beta_1 - \beta_2} \operatorname{Re} \left[ \delta_1 \beta_1 \left( 1 - \frac{z_1}{\sqrt{z_1^2 - l^2}} \right) - \delta_2 \beta_2 \left( 1 - \frac{z_2}{\sqrt{z_2^2 - l^2}} \right) \right], \\
\dot{i}_{11} &= \dot{p}^{(\infty)} - \frac{\mu v_{2,2}^{(\infty)}}{\beta_1 - \beta_2} \operatorname{Re} \left[ \delta_1 \beta_1 - \delta_2 \beta_2 + \varepsilon_1 \beta_1 \frac{z_1}{\sqrt{z_1^2 - l^2}} - \varepsilon_2 \beta_2 \frac{z_2}{\sqrt{z_2^2 - l^2}} \right], \\
\dot{i}_{22} &= \dot{p}^{(\infty)} - \frac{\mu v_{2,2}^{(\infty)}}{\beta_1 - \beta_2} \operatorname{Re} \left[ \delta_1 \beta_1 - \delta_2 \beta_2 - \chi_1 \beta_1 \frac{z_1}{\sqrt{z_1^2 - l^2}} + \chi_2 \beta_2 \frac{z_2}{\sqrt{z_2^2 - l^2}} \right], \\
\dot{i}_{12} &= \frac{\mu v_{2,2}^{(\infty)}}{\beta_1 - \beta_2} \operatorname{Im} \left[ \chi_1 \beta_1^2 \frac{z_1}{\sqrt{z_1^2 - l^2}} - \chi_2 \beta_2^2 \frac{z_2}{\sqrt{z_2^2 - l^2}} \right], \\
\dot{i}_{21} &= \frac{\mu v_{2,2}^{(\infty)}}{\beta_1 - \beta_2} \operatorname{Im} \left[ \varepsilon_1 \frac{z_1}{\sqrt{z_1^2 - l^2}} - \varepsilon_2 \frac{z_2}{\sqrt{z_2^2 - l^2}} \right].
\end{aligned} \tag{4.76}$$

#### 4.1.4 Incremental stress intensity factors

Employing the definition of  $\dot{K}_{(\epsilon)I}$  given by eqn. (4.23)<sub>1</sub> in the full-field solution in the EC regime, eqn. (4.68)<sub>3</sub>, or in the EI regime, eqn. (4.75)<sub>3</sub>, we obtain

$$\dot{K}_{(\epsilon)I} = 2 \mu v_{2,2}^{(\infty)} \sqrt{\pi l}, \tag{4.77}$$

while, if we use the definition (3.44)<sub>1</sub> of incremental stress intensity factor [instead of definition (4.23)<sub>1</sub>], we get

$$\dot{K}_I = -\mu v_{2,2}^{(\infty)} \sqrt{\pi l} \left[ \sqrt{1 - k^2} - 1 + \eta \right], \tag{4.78}$$

Note that, due to the different normalizations, both the definitions (4.77) and (4.78) differ from that employed by Cristescu et al. (2004) for cracks and by Ballarini (1990) for stiffeners in the infinitesimal theory. Interestingly, the incremental stress intensity factor (4.77) [differently from (4.78)] results independent of the prestress parameters  $\xi$ ,  $k$ ,  $\eta$  (but  $\mu$  may depend on the full set of current state variables). Moreover, the incremental stress intensity factor (4.78) vanishes for condition (4.21).

We note that the full-field solution (4.69) matches the asymptotic one (4.20), (4.25) when both  $z_1$  and  $z_2$  approach  $l$ . Moreover, all terms of the type  $z_n/\sqrt{z_n^2 - l^2}$  ( $n = 1, 2$ ) become leading order contributions, behaving as  $1/\sqrt{r}$  near the line tip.

### 4.1.5 Shear bands interacting with a stiffener

The analytical solutions found in §4.1.1 and §4.1.3 are now employed to investigate the incremental fields until near the boundary of ellipticity loss.

All cases have been investigated for simplicity with a horizontal tensile or compressive prestress  $T_1$ , while vertical prestress has been taken null,  $T_2 = 0$ , so that  $k = \eta$ .

We begin with the simple case of a Mooney-Rivlin ( $\xi = 1$ ), which results are presented in Fig. 4.8 for different values of the prestress dimensionless parameter  $k$ .

According to the Mooney-Rivlin material model, the response always lies in the EI regime and reaches the EI/P boundary at an infinite stretch. Would this boundary be attained, a shear band in terms of discontinuity of velocity gradient across a planar band would be predicted to occur aligned parallel to the maximum prestress (which can be positive or null for uniaxial tension and compression, respectively).

The figures are organized as follows. The case of null prestress ( $k = 0$ ) is on the upper part, while (the absolute value of) prestress increases from the top to the bottom of the figures, in particular  $k = \pm 0.7$  and  $k = \pm 0.985$  are considered. When the prestress is increased almost close to the boundary of ellipticity loss (which corresponds to  $k = \pm 1$ ), shear bands clearly emerge. In particular, two shear bands form aligned parallel (or orthogonal) to the stiffener for tensile  $k = 0.985$  (or compressive,  $k = -0.985$ ) prestress. The orthogonal bands nucleate as induced by a sort of ‘Poisson effect’. As already noticed by Bigoni and Capuani (2002; 2005), even in the present context we find that shear bands, which are excluded in terms of incremental displacement gradient discontinuity for a Mooney-Rivlin material, become visible, thanks to our perturbative approach, in which the stiffener plays the role of a perturbing agent.

Results reported in Figs. 4.9–4.10 refer to a  $J_2$ -deformation theory material. Here the prestrain is prescribed, in terms of the logarithmic strain  $\varepsilon = \ln \lambda$  (where  $\lambda$  is the in-plane maximum stretch). This parameter is used to ‘tune’ the distance to the elliptic boundary, in particular, EC/H is now approached. The critical logarithmic strain  $\varepsilon^{EL}$  for shear band formation in terms of incremental displacement gradient discontinuities and their inclination at the EC/H boundary can be calculated employing eqns. (2.63) and (2.64) respectively. In particular,  $\varepsilon^{EL} \simeq \pm 0.3216$  and  $\varepsilon^{EL} \simeq \pm 0.6778$  correspond to points at the EC/H boundary for the two values of the hardening parameter  $N$ , 0.1 and 0.4, assumed in the subsequent examples. The following

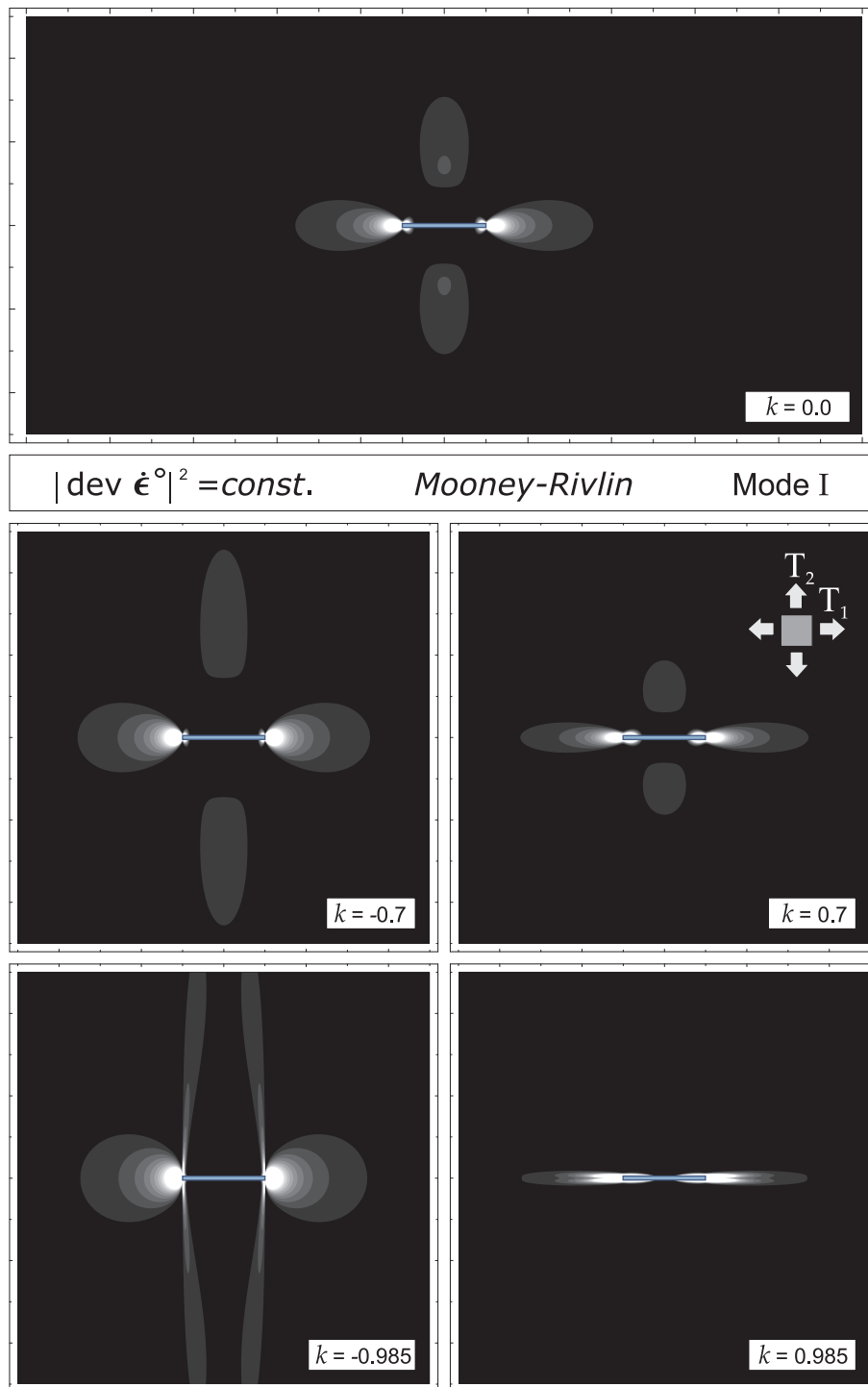


Figure 4.8: Interaction of shear bands and mechanical fields near a stiffener of length  $2l$  (evidenced with a thin rectangle, providing the scale bar of the representation). A Mooney-Rivlin material at different values of prestress parameter  $k$  (increasing from the top to the bottom of the figure) subject to a uniform incremental Mode I perturbation at infinity is considered. For  $k = 0.985$  a shear band emerges aligned parallel to the stiffener, while for  $k = -0.985$  two shear bands form orthogonally to the tips of the stiffener.

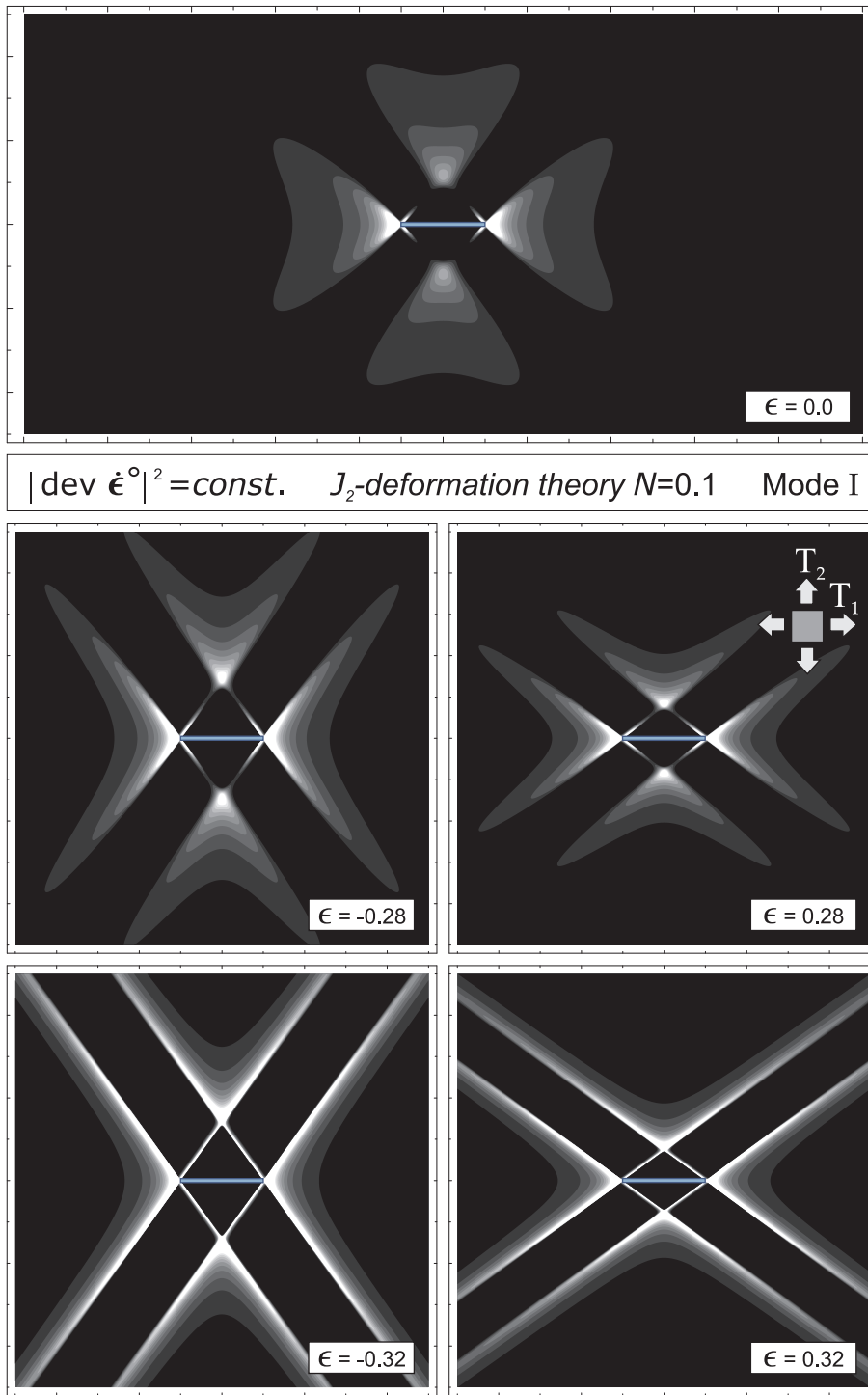


Figure 4.9: Interaction of shear bands and mechanical fields near a stiffener of length  $2l$  (evidenced with a thin rectangle, providing the scale bar of the representation). A  $J_2$ -deformation theory material with  $N = 0.1$  at different values of logarithmic prestrain  $\epsilon$  (increasing from the top to the bottom of the figure) subject to a uniform incremental Mode I perturbation at infinity is considered. For  $\epsilon = 0.32$  ( $-0.32$ ) shear bands emerge inclined at  $\vartheta^{SB} \simeq \pm 35.942^\circ$  ( $\pm 54.058^\circ$ ) with respect to the stiffener axis  $x_1$ .

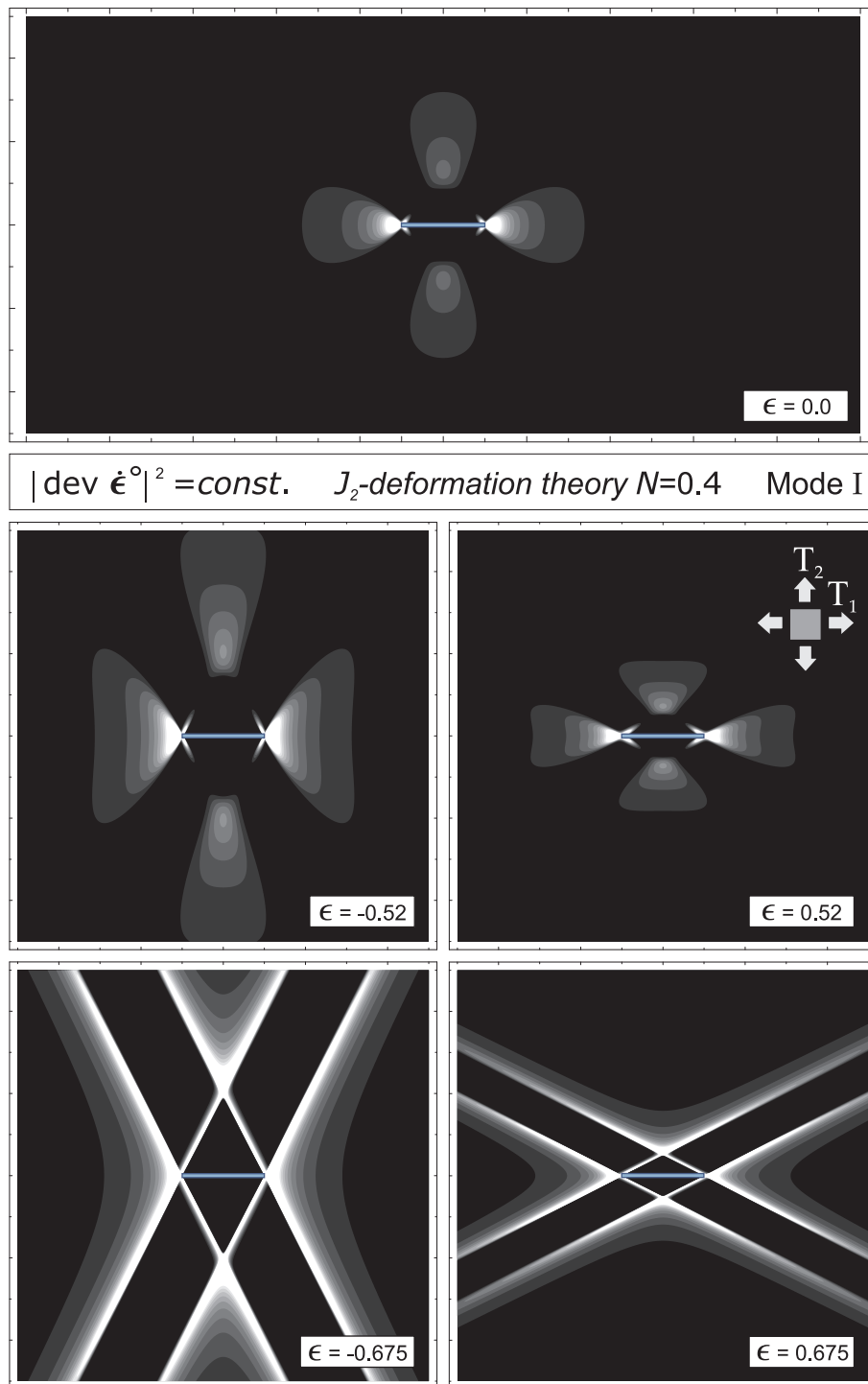


Figure 4.10: As for Fig. 4.9, but for higher hardening exponent  $N = 0.4$ . For  $\varepsilon = 0.675$  ( $-0.675$ ) shear bands emerge inclined at  $\vartheta^{SB} \simeq \pm 26.918^\circ$  ( $\pm 63.082^\circ$ ) with respect to the stiffener axis  $x_1$ . Note the difference with the shear band inclinations visible in that figure.

shear band inclinations  $\vartheta^{SB}$  (measured from the  $x_1$ -axis) can be calculated at the EC/H boundary:

$$\begin{aligned} \text{for } N = 0.1, \quad \vartheta^{SB} &\simeq \begin{cases} \pm 35.942^\circ, & \text{if } \varepsilon > 0, \\ \pm 54.058^\circ, & \text{if } \varepsilon < 0; \end{cases} \\ \text{for } N = 0.4, \quad \vartheta^{SB} &\simeq \begin{cases} \pm 26.918^\circ, & \text{if } \varepsilon > 0, \\ \pm 63.082^\circ, & \text{if } \varepsilon < 0. \end{cases} \end{aligned}$$

Results for  $N=0.1$  and  $0.4$  are reported in Figs. 4.9 and 4.10, respectively.

The striking difference between the Mooney-Rivlin case, Fig. 4.8, and the  $J_2$ -deformation theory of plasticity, Figs. 4.9 - 4.10, is the inclination of the shear bands, which, in the latter case, is similar to that typical of metals.

We end our investigation, reporting asymptotic results for Mode II loading in Figs. 4.11–4.13. In particular Fig. 4.11 pertains to a Mooney-Rivlin material, while Figs. 4.12–4.13 to a  $J_2$ -deformation theory material, both investigated at increasing values of prestress (for Mooney-Rivlin) or prestrain (for  $J_2$ -material).

As final comments, we remark that:

- i) the presence of a stiffener strongly promotes shear band formation;*
- ii) shear bands develop radially from the stiffener tip;*
- iii) shear bands maintain the inclination that can be calculated in terms of singularity of the acoustic tensor at the boundary of ellipticity;*
- iv) the band inclination is independent of the perturbation mode.*

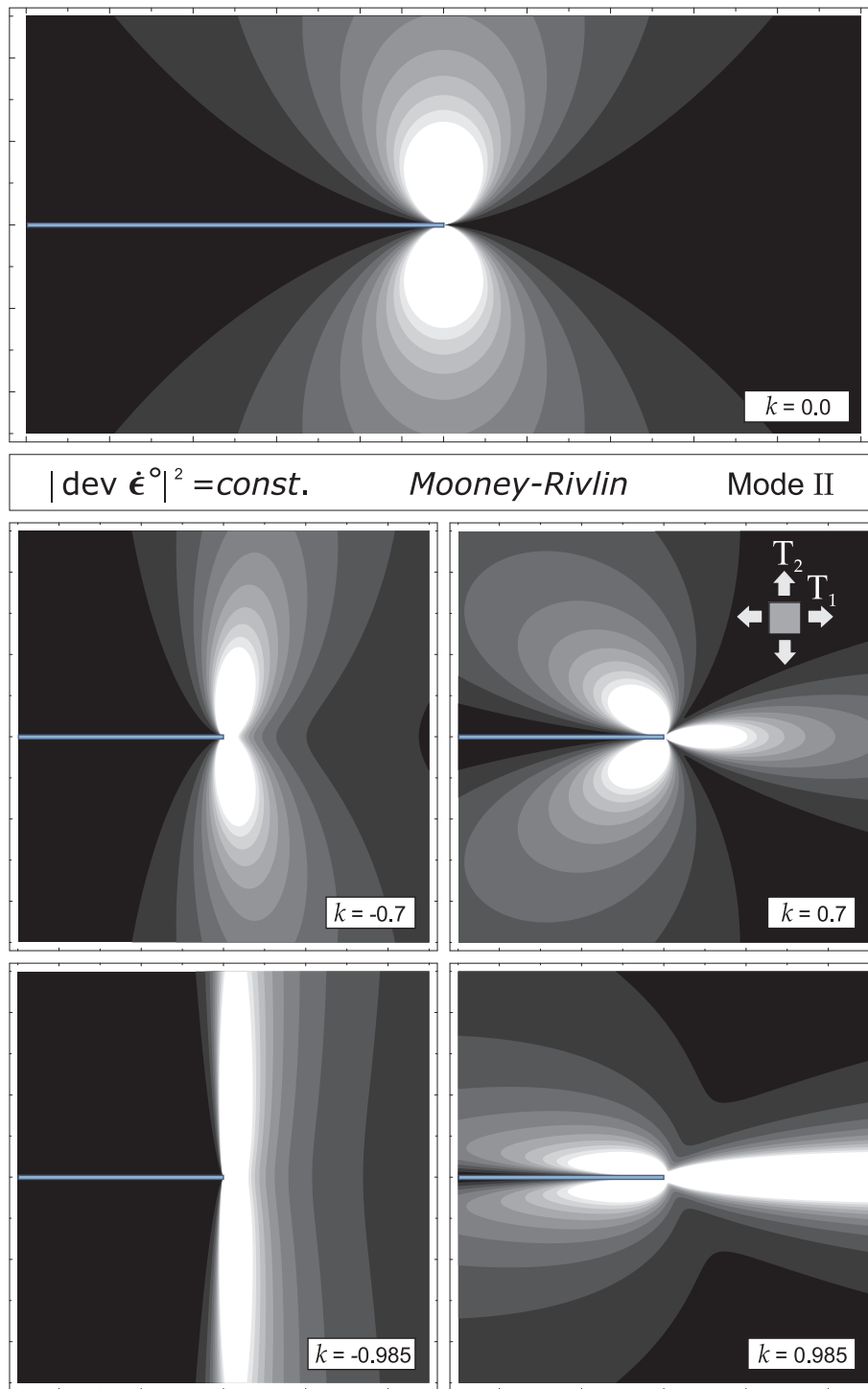


Figure 4.11: Interaction of shear bands and mechanical fields near the tip of a stiffener (asymptotic solution). A Mooney-Rivlin material at different values of prestress parameter  $k$  (increasing from the top to the bottom of the figure) subject to an incremental Mode II perturbation (asymptotic solution) is considered.

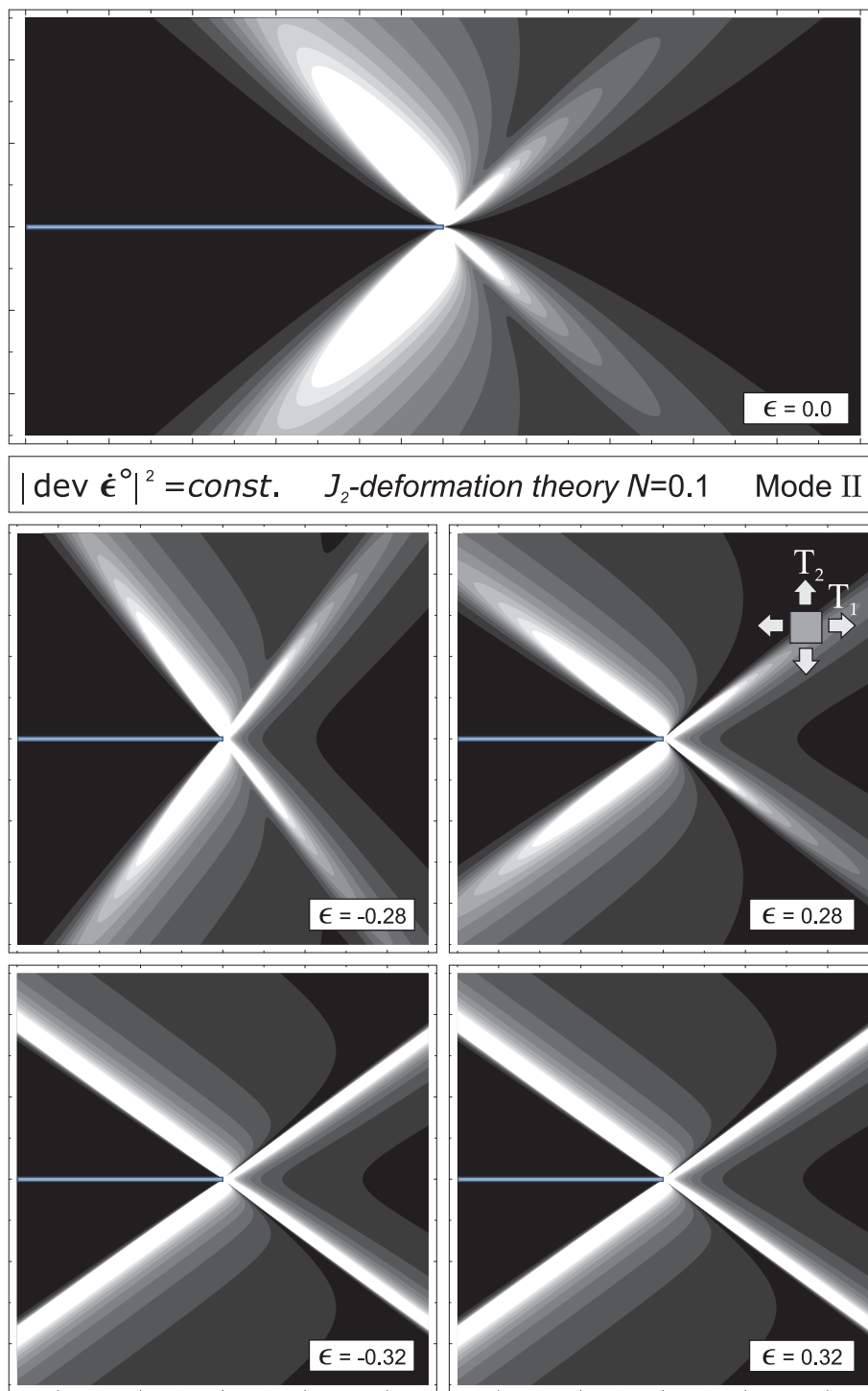
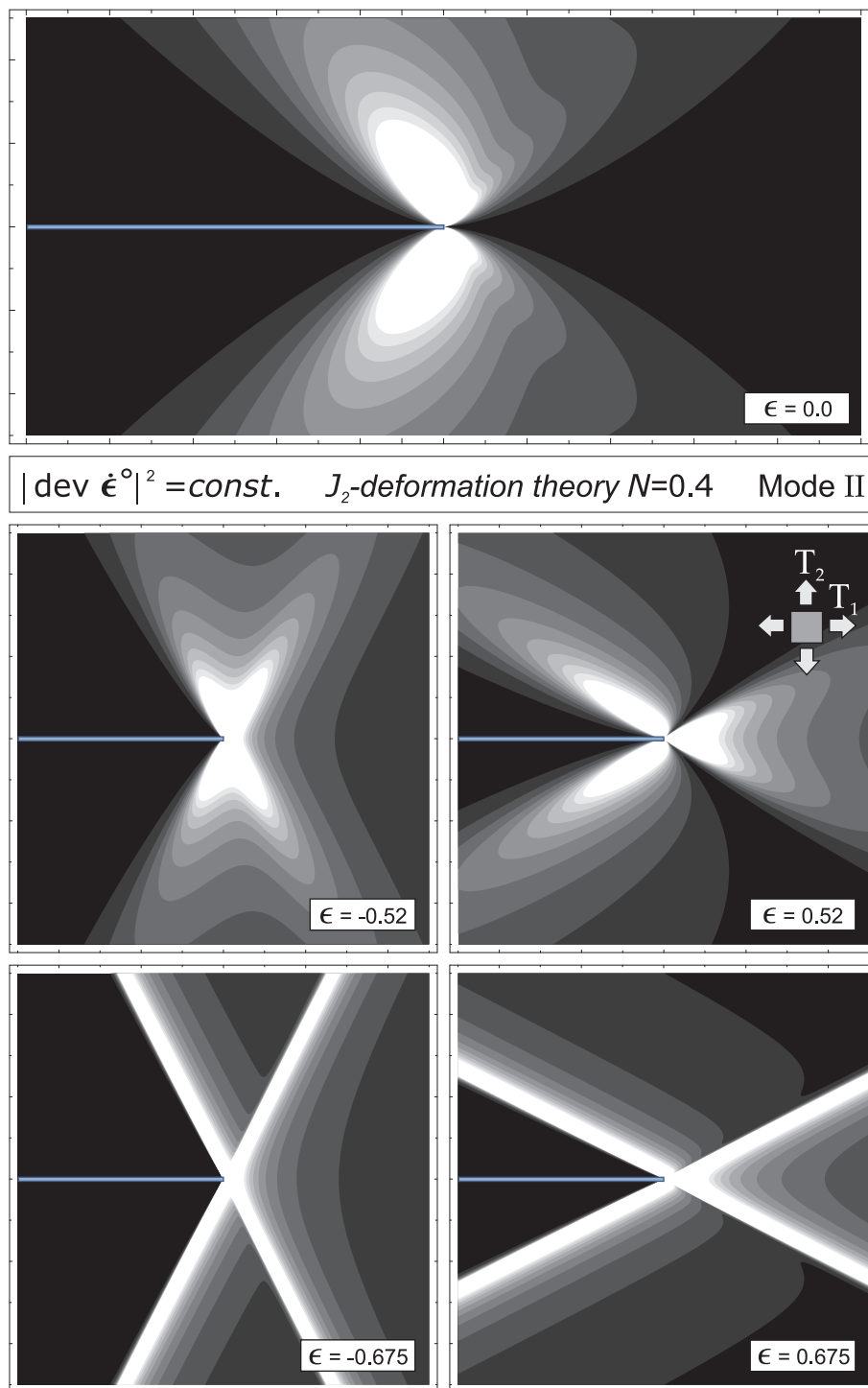


Figure 4.12: Interaction of shear bands and mechanical fields near the tip of a stiffener (asymptotic solution). A  $J_2$ -deformation theory material with  $N = 0.1$  at different values of logarithmic prestrain  $\epsilon$  (increasing from the top to the bottom of the figure) subject to an incremental Mode II perturbation is considered.

Figure 4.13: As for Fig. 4.12, but for higher hardening exponent  $N = 0.4$ .

## 4.2 Mode I perturbation of a stiffener in an infinite material subjected to finite simple shear deformation

In this section the problem of a rigid line inclusion of length  $2l$  embedded in an elastic material, homogeneously prestressed within the elliptic regime by a finite simple shear (appendix C.2) parallel to the inclusion, subject to a uniform perturbation under Mode I is considered (for uniform Mode II loading the stiffener leaves the medium unperturbed).

The homogeneous state of prestress is defined by the shear amount  $\gamma$  and has the principal stress axes inclined of  $\vartheta_E$ , eqn. (C.22), with respect to the inclusion line and is taken as the reference state<sup>11</sup> on which a perturbation corresponding to remote uniform Mode I incremental deformation  $\hat{v}_{2,2}^\infty$  is superimposed.

A  $\hat{x}_1$ - $\hat{x}_2$  reference system located at the stiffener centre, taken with the inclusion line parallel to the  $\hat{x}_1$ -axis, is inclined at an angle  $\vartheta_0$  (taken equal to  $\vartheta_E$ ) with respect to the  $x_1$ - $x_2$  system, defining the principal stress directions, Fig. 4.1.

Due to central symmetry considerations (with respect to the stiffener centre) involved in the far-field loading problem under analysis and the specific form of solution sought in the following, the boundary conditions (4.1) and (4.3) can be reduced to the following homogeneous incremental displacement gradient conditions:

$$\begin{cases} \hat{v}_{1,1}(\hat{x}_1, 0) = 0, \\ \hat{v}_{2,1}(\hat{x}_1, 0) = \omega_S, \end{cases} \quad \forall |\hat{x}_1| < l, \quad (4.79)$$

plus the requirement that the normal stress increment  $\hat{t}_{22}$  be continuous across the stiffener

$$[[\hat{t}_{22}(\hat{x}_1, 0)]] = 0, \quad \forall |\hat{x}_1| < l, \quad (4.80)$$

a condition allowing determination of  $\omega_S$ .

Prescribing an incremental deformation  $\hat{v}_{2,2}^\infty$  at infinity, analogously to the crack problem analyzed in §3.2, the stream function of the perturbed problem

---

<sup>11</sup>The analysis can be carried with respect to a generic, uniform state of prestress (with principal values inclined at  $\vartheta_0$  different from  $\vartheta_E$ ), not necessarily generated through a simple shear deformation.

$\widehat{\psi}^\circ$  can be sought in the form

$$\widehat{\psi}^\circ(\hat{x}_1, \hat{x}_2) = \frac{\widehat{v}_{2,2}^\infty}{2} \sum_{j=1}^2 \operatorname{Re} \left\{ D_j \left[ \hat{z}_j^2 - \hat{z}_j \sqrt{\hat{z}_j^2 - l^2} + l^2 \ln \left( \hat{z}_j + \sqrt{\hat{z}_j^2 - l^2} \right) \right] \right\}, \quad (4.81)$$

satisfying automatically the decaying condition on the velocity, incremental strain and stress at infinity (in the elliptic regime) and providing a stress square-root singularity at the stiffener tips.

Imposing the stream function (4.81) to satisfy the boundary conditions along the stiffener line (4.79) and (4.80) yield the following linear problem for the complex constants  $D_1$  and  $D_2$

$$\begin{bmatrix} \operatorname{Re}[W_1] & -\operatorname{Im}[W_1] & \operatorname{Re}[W_2] & -\operatorname{Im}[W_2] \\ \operatorname{Im}[W_1] & \operatorname{Re}[W_1] & \operatorname{Im}[W_2] & \operatorname{Re}[W_2] \\ 0 & 1 & 0 & 1 \\ -c_{21} & c_{11} & -c_{22} & c_{12} \end{bmatrix} \begin{bmatrix} \operatorname{Re}[D_1] \\ \operatorname{Im}[D_1] \\ \operatorname{Re}[D_2] \\ \operatorname{Im}[D_2] \end{bmatrix} = \begin{bmatrix} 1 \\ 0 \\ 0 \\ 0 \end{bmatrix}, \quad (4.82)$$

where the real constants  $c_{1j}$  and  $c_{2j}$  ( $j=1, \dots, 4$ ) are defined by eqns. (3.53) and depend on the stiffener inclination  $\vartheta_0$  and on the prestress and orthotropy parameters  $\xi$ ,  $k$ , and  $\eta$ . We introduce the normalized stiffener rotation  $\Gamma$  as

$$\Gamma = \frac{\omega_S}{\widehat{v}_{2,2}^\infty} = -\operatorname{Re}[D_1 + D_2], \quad (4.83)$$

and since analytical proof looks awkward, we have numerically checked that:

- i) the solution of the present problem is independent of the in-plane stress parameter  $\eta$ ;
- ii) the coefficients  $D_j$  ( $j = 1, 2$ ) solving system (4.82) satisfy the following two equations

$$W_1^2 D_1 + W_2^2 D_2 = W_1 + W_2 + \Gamma W_1 W_2, \quad (4.84)$$

$$W_1^3 D_1 + W_2^3 D_2 = W_1^2 + W_1 W_2 + W_2^2 + \Gamma W_1 W_2 (W_1 + W_2);$$

- iii) the rotation parameter  $\Gamma$  (4.83) satisfies the conditions

$$\begin{aligned} \Gamma(k=0, \vartheta_0) &= \Gamma(k, \vartheta_0=0) = \Gamma(k, \vartheta_0=\pi/2) = 0, \\ \Gamma &= \Gamma(k, \vartheta_0) = -\Gamma(-k, \pi/2 - \vartheta_0). \end{aligned} \quad (4.85)$$

Defined in terms of incremental velocity gradient as in the case of a stiffener aligned to an orthotropy axis, eqn. (4.23)<sub>1</sub>, the incremental stress intensity factor under Mode I loading is

$$\dot{K}_{(\epsilon)I} = 2\mu \lim_{\hat{x}_1 \rightarrow l^+} \sqrt{2\pi(\hat{x}_1 - l)} \hat{v}_{2,2}(\hat{x}_1, \hat{x}_2 = 0) = 2\mu \hat{v}_{2,2}^\infty \sqrt{\pi l}, \quad (4.86)$$

resulting independent of the prestress parameters  $\xi$ ,  $k$ ,  $\eta$  (but  $\mu$  may depend on the full set of current state variables) and of the angle  $\vartheta_0$  between the stiffener and the directions of principal stress  $T_1$ .

The solution for a stiffener aligned parallel to the principal stress directions (§4.1.3) can be now recovered by setting  $\vartheta_0 = 0$  and thus obtaining

$$\begin{aligned} D_1 = -D_2 &= -\frac{1}{2\alpha}, & \Gamma &= 0, & \text{in EC,} \\ D_1 = -D_2 &= -\frac{i}{\beta_1 - \beta_2}, & \Gamma &= 0, & \text{in EI,} \end{aligned} \quad (4.87)$$

showing that in the case of a stiffener aligned parallel to prestress principal axes there is no rigid rotation of the line due to the symmetry of the problem. The stiffener rotation  $\omega_S$  is null also in an another case corresponding to  $k = 0$  (and  $\{\vartheta_0, \eta\} \neq 0$ ),

$$D_1 = -D_2 = \frac{1}{2\sqrt{1-\xi}}(-\cos 2\vartheta_0 + i\sqrt{\xi} \sin 2\vartheta_0), \quad \Gamma = 0. \quad (4.88)$$

The normalized stiffener rotation  $\Gamma$  (4.83) is reported in Fig. 4.14, for a  $J_2$ -deformation theory material, showing an antisymmetric behaviour with respect to the shear parameter  $\gamma$ . Note that results reported in Fig. 4.14 are independent of the hardening parameter  $N$ , except for the fact that the curve terminates at failure of ellipticity  $\gamma^{EL} = \gamma^{EL}(N)$ .

The previously obtained solution can be now employed to analyze the incremental strain field near the stiffener. In particular, level sets of the modulus of perturbed incremental deviatoric strain for  $J_2$ -deformation theory of plasticity are reported in Fig. 4.15 for low  $N = 0.1$  (upper part) and high  $N = 0.8$  (lower part) strain hardening.

For a  $J_2$ -deformation theory material the loss of ellipticity occurs at  $\gamma^{EL} = 0.654$  for  $N = 0.1$  and at  $\gamma^{EL} = 2.452$  for  $N = 0.8$ . Two values of amount of shear  $\gamma$  have been considered in Fig. 4.15, namely,  $\gamma = 0$  corresponding to a

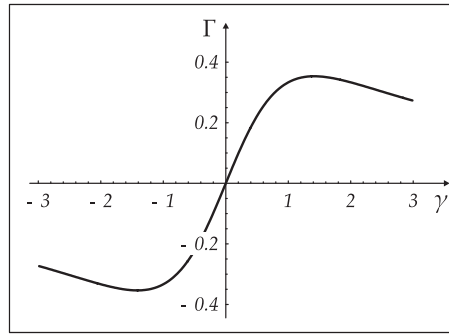


Figure 4.14: The normalized stiffener rotation  $\Gamma = \omega_S / \hat{\psi}_{2,2}^\infty$  of the stiffener in a  $J_2$ -deformation theory material generated by an incremental Mode I superimposed upon a simple shear of finite amount  $\gamma$ .

material with null prestress<sup>12</sup> and  $\gamma \simeq 0.95\gamma^{EL}$ , namely, close to the boundary of ellipticity loss, before the Mode I perturbation is applied.

When the perturbation is applied at high prestrain, the incremental deformation fields appear strongly focussed along the near-tip directions of the shear bands formally possible at ellipticity loss. Moreover, the results pertaining to low strain hardening ( $N = 0.1$ , upper part of Fig. 4.15) show that

*the bands closest to the stiffener line result to be privileged, so that a form of a ‘thick’ shear band parallel to the stiffener appears,*

a finding in qualitative agreement with experimental results by Misra and Mandal (2007).

<sup>12</sup>At null prestress, the  $J_2$ -deformation theory of plasticity becomes incrementally rigid (since both  $\mu$  and  $\mu_*$  tend to infinity, see Fig. 2.2, but their ratio  $\xi$  tends to  $N$ ). It is expedient therefore to plot results normalized through division by  $\mu$ , so that they tend to results pertaining to an incompressible orthotropic material deformed in small strain. The axes of orthotropy are therefore inclined at  $45^\circ$  with respect to the stiffener line in Fig. 4.15.

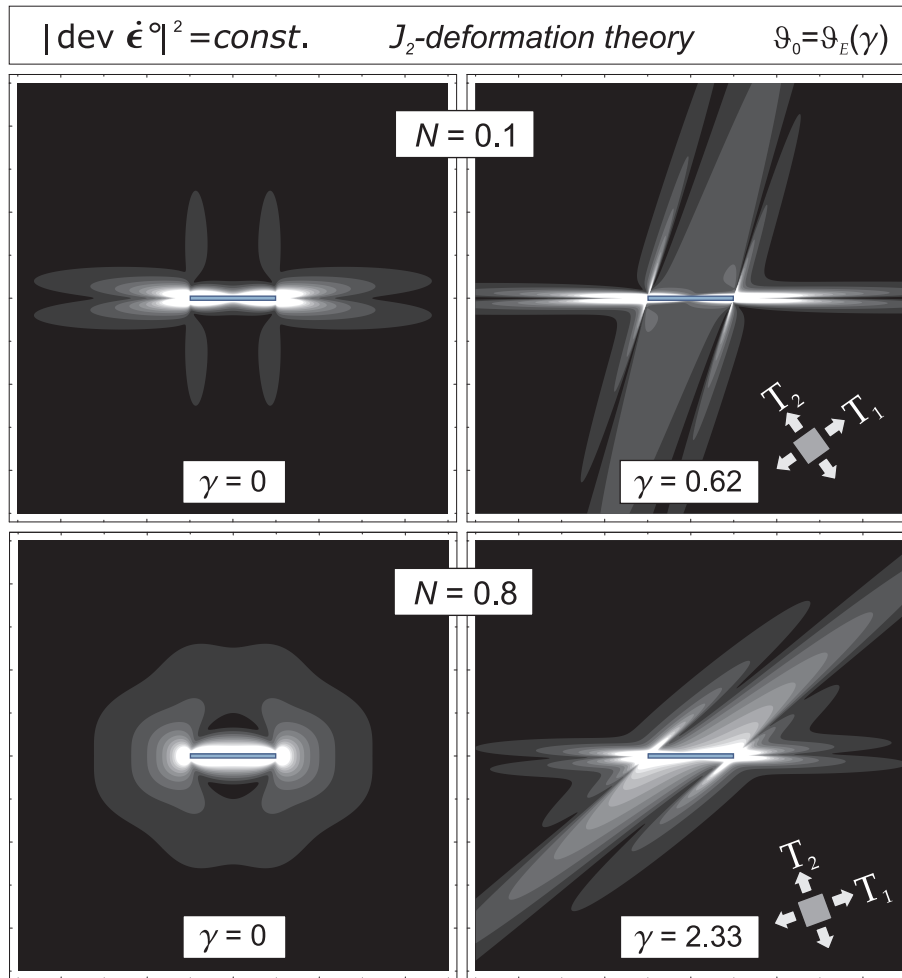


Figure 4.15: Interaction of shear bands and mechanical fields near a stiffener (evidenced with a thin rectangle, providing the scale bar of the representation) embedded in a  $J_2$ -deformation theory material (with  $N = 0.1$  (upper part) and  $N = 0.8$  (lower part)) subject to a finite simple shear of amount  $\gamma$  and a subsequent Mode I incremental uniform remote load. Null shear before the perturbation is considered on the left, while a shear equal to 0.95 times the amount at ellipticity loss,  $\gamma^{EL}$ , is considered on the right. Note that the prestress (of principal components  $T_1$  and  $T_2$ ) generated through the shear deformation is inclined with respect to the stiffener line (and sketched in the figures).

### 4.3 Incremental solution in the parabolic and hyperbolic regimes

Accepting non-decaying of the solution and infinite strain (and stress) increment along certain shear band lines, the previously obtained solution can be extended to the parabolic and hyperbolic regimes. Since beyond the elliptic range a problem is known to be ill-posed, the analysis of the solution within the parabolic and hyperbolic regimes is instructive to reveal features related to ill-posedness.

To obtain a solution (which need not to be unique) beyond the elliptic range, we have to go back to the representation of the stream function (4.81), where now the indices have to range from 1 to  $n$ , so that

$$\widehat{\psi}^\circ(\hat{x}_1, \hat{x}_2) = \frac{\hat{v}_{2,2}^\infty}{2} \sum_{j=1}^n \operatorname{Re} \left\{ D_j \left[ \hat{z}_j^2 - \hat{z}_j \sqrt{\hat{z}_j^2 - l^2} + l^2 \ln \left( \hat{z}_j + \sqrt{\hat{z}_j^2 - l^2} \right) \right] \right\}, \quad (4.89)$$

where  $n$  indicates the number of non-conjugate roots [i.e.  $n = 4$  ( $n = 3$ ) in H (P)].

Outside the elliptic regime, the characteristic lines defined as

$$\hat{z}_j = \text{const} \quad \Rightarrow \quad \frac{d\hat{x}_2}{d\hat{x}_1} = -\frac{1}{W_j}, \quad (4.90)$$

become real and correspond to four (two) different families in the hyperbolic (parabolic) regime and, in particular, their inclinations correspond to the following shear band inclinations with respect to the  $\hat{x}_1$  axis

$$\widehat{\vartheta}_j^{SB} = -\arctan \left[ \frac{1}{W_j} \right] = \vartheta_0 - \arctan \left[ \frac{1}{\Omega_j} \right] = \vartheta_0 - \vartheta_j^{SB}, \quad j = 1, \dots, 4. \quad (4.91)$$

The decaying of solution (4.89) is lost along the characteristic lines emanating from the stiffener tips, where, additionally, the increment of strain, and consequently stress, becomes infinite (while for the other characteristic lines cutting the stiffener the solution remains always bounded). In contrast, incremental displacements remain continuous and finite everywhere, even along characteristics.

The system of linear equations

$$\left\{ \begin{array}{l} \sum_{j=1}^n \operatorname{Re}[W_j] \operatorname{Re}[D_j] - \operatorname{Im}[W_j] \operatorname{Im}[D_j] = 1, \\ \sum_{j=1}^n \operatorname{sign}[\operatorname{Im}[\Omega_j]] \{ \operatorname{Im}[W_j] \operatorname{Re}[D_j] + \operatorname{Re}[W_j] \operatorname{Im}[D_j] \} = 0, \\ \sum_{j=1}^n \operatorname{sign}[\operatorname{Im}[\Omega_j]] \operatorname{Im}[D_j] = 0, \\ \sum_{j=1}^n \operatorname{sign}[\operatorname{Im}[\Omega_j]] \{ -c_{2j} \operatorname{Re}[D_j] + c_{1j} \operatorname{Im}[D_j] \} = 0, \end{array} \right. \quad (4.92)$$

replaces system (4.82) and determine the  $n$  complex constants  $D_j$ , providing the solution. Note that the determination of these  $2n$  real constants depend on 4 equations, so that  $\infty^{2n-4}$  solutions are possible.

Focussing attention to the hyperbolic regime, where the roots  $W_j$  are real, the system (4.92) simplifies to

$$\left\{ \begin{array}{l} \sum_{j=1}^4 W_j \operatorname{Re}[D_j] = 1, \\ \sum_{j=1}^4 W_j \operatorname{Im}[D_j] = 0, \\ \sum_{j=1}^4 \operatorname{Im}[D_j] = 0, \\ \sum_{j=1}^4 W_j^2 \left[ 2 \left( \widehat{\mathbb{G}}_{2221} - \widehat{\mathbb{G}}_{2111} \right) - W_j \widehat{\mathbb{G}}_{2121} \right] \operatorname{Im}[D_j] = 0, \end{array} \right. \quad (4.93)$$

so that the general solution of linear system (4.93) can be written as

$$\begin{aligned}
 \begin{bmatrix} D_1 \\ D_2 \\ D_3 \\ D_4 \end{bmatrix} &= \zeta_1 \begin{bmatrix} 1 \\ 0 \\ 0 \\ 0 \end{bmatrix} + \zeta_2 \begin{bmatrix} 0 \\ 1 \\ 0 \\ 0 \end{bmatrix} + \zeta_3 \begin{bmatrix} 0 \\ 0 \\ 1 \\ 0 \end{bmatrix} + \frac{1 - \zeta_1 W_1 - \zeta_2 W_2 - \zeta_3 W_3}{W_4} \begin{bmatrix} 0 \\ 0 \\ 0 \\ 1 \end{bmatrix} \\
 &+ i \varrho \begin{bmatrix} (c_{14} - c_{13}) W_2 + (c_{12} - c_{14}) W_3 + (c_{13} - c_{12}) W_4 \\ (c_{13} - c_{14}) W_1 + (c_{14} - c_{11}) W_3 + (c_{11} - c_{13}) W_4 \\ (c_{14} - c_{12}) W_1 + (c_{11} - c_{14}) W_2 + (c_{12} - c_{11}) W_4 \\ (c_{12} - c_{13}) W_1 + (c_{13} - c_{11}) W_2 + (c_{11} - c_{12}) W_3 \end{bmatrix}, \tag{4.94}
 \end{aligned}$$

where  $\zeta_1$ ,  $\zeta_2$ ,  $\zeta_3$ , and  $\varrho$  are arbitrary real constants.

Since system (4.93) admits  $\infty^4$  solutions, we have chosen to represent in Fig. 4.16 the deformed shape of an area near the stiffener, for the four solutions corresponding (from left to right and from the upper to the lower part) to index  $h$  ranging between 1 and 4 so that<sup>13</sup>

$$D_h = \frac{1}{W_h}, \quad D_j = 0, \quad j \neq h, \quad j \in [1, 4]. \tag{4.95}$$

We can note from Fig. 4.16 that for given uniform Mode I remote loading of a stiffener embedded in a medium uniformly prestrained beyond the elliptic range:

- i) an infinite number of solutions is possible;*
- ii) these solutions do not decay at infinity;*
- iii) they correspond to infinite incremental strain and stress along shear bands,*
- iv) these shear bands emanate from the tips of the stiffener.*

---

<sup>13</sup>The values in (4.95) are achievable for  $\varrho = 0$  and

$$\begin{aligned}
 \zeta_h &= \frac{1}{W_h}, \quad \zeta_k = 0, \quad k \neq h, & \text{if } h = 1, 2, 3, \\
 \zeta_1 = \zeta_2 = \zeta_3 &= 0, & \text{if } h = 4.
 \end{aligned}$$

The above conclusion, based on an analytical solution, explains the difficulties typically encountered in the numerical analyses of ill-posed boundary value problems.

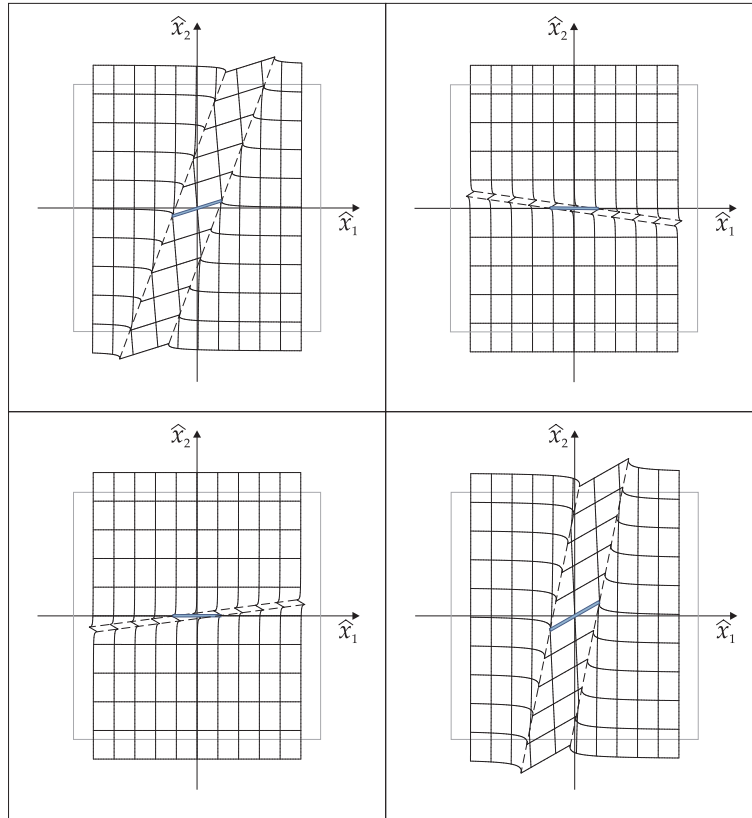


Figure 4.16: Deformed configurations (the grey square represent the undeformed, prestressed material) for a stiffener (evidenced with a thin rectangle, providing the bar scale of the representation) embedded in a  $J_2$ -deformation theory material (with  $N = 0.1$ , subject to a finite shear of amount  $\gamma = 1.2\gamma^{EL}$ ) and a subsequent Mode I incremental uniform remote load. Four solutions are reported among the  $\infty^4$  possible *within the hyperbolic range*, where characteristics are inclined at  $\hat{\vartheta}^{SB} \simeq \{62.984^\circ, -5.874^\circ, 5.434^\circ, 74.292^\circ\}$ , with respect to the  $\hat{x}_1$ -axis.

#### 4.4 Incremental energy release rate for stiffener growth (or reduction)

We attack now the problem of incremental energy release rate for stiffener growth. To this purpose, we refer to Fig. 4.17, where two incremental boundary value problems are compared (for finite bodies subject to identical conditions on the external boundaries  $S_\sigma \cup S_v$ , namely, prescribed incremental nominal tractions  $\dot{\boldsymbol{\sigma}}^0$  on  $S_\sigma$  and incremental displacements  $\mathbf{v} = \bar{\mathbf{v}}$  on  $S_v$ ; note the similarity with the void problem, see Rice, 1968, p. 205) only differing in the sizes of the rigid body that they contain. In particular, the inclusion in

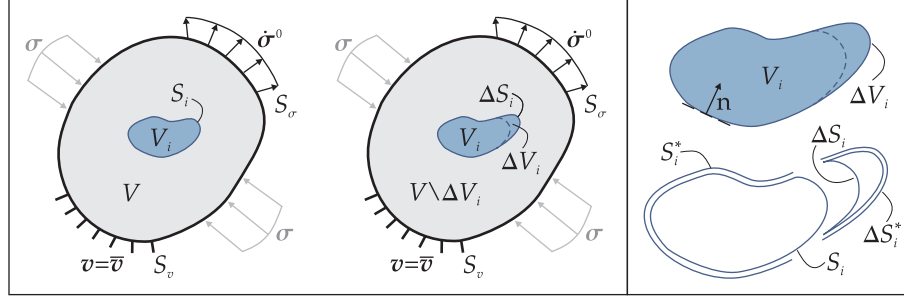


Figure 4.17: Two elastic, prestressed bodies are compared (left), having identical shape, boundary conditions, elastic properties, prestress, and prestrain, but inclusions of different size. The detail of the rigid inclusion and its surface is reported on the right; note the unit normal vector, defined to point outward the elastic body and toward the inclusion.

the body on the right (of volume  $V_i \cup \Delta V_i$ , enclosed by surface  $S_i^* \cup \Delta S_i^*$ ) has been obtained by increasing the size of the inclusion in the body on the left (of volume  $V_i$ , enclosed by surface  $S_i$ ). We define the incremental displacement and nominal traction fields, solutions to the two problems, as  $\mathbf{v}^0$  and  $\dot{\mathbf{t}}^0$  for the problem on the left and  $\mathbf{v} = \mathbf{v}^0 + \tilde{\mathbf{v}}$  and  $\dot{\mathbf{t}} = \dot{\mathbf{t}}^0 + \tilde{\mathbf{t}}$  for the problem on the right. Note that  $\mathbf{v}^0$  and  $\mathbf{v}$  are rigid body incremental displacements within  $V_i$  and  $V_i \cup \Delta V_i$ , respectively.

The two bodies are assumed to be identically prestressed and prestrained, although not necessarily in a homogeneous way. Obviously, in order to have identical prestress and prestrain, the two current configurations shown in Fig. 4.17 cannot be reached through a continuous deformation path starting from unloaded configurations containing different rigid inclusions. The situation sketched in Fig. 4.17 can be obtained through a ‘rigidification’ of different

volumes (corresponding to the two inclusions) at a stage of a deformation process.<sup>14</sup>

Neglecting body forces, the incremental potential energy functional  $\dot{P}$  used by Hill (1961), minimal for the incremental displacement field solution of the incremental problem, is:

$$\dot{P}^0 = \int_V \phi(\nabla \mathbf{v}^0) dV - \int_{S_\sigma} \dot{\boldsymbol{\sigma}}^0 \cdot \mathbf{v}^0 dS, \quad (4.96)$$

for the body on the left in Fig. 4.17, and

$$\dot{P}^0 + \Delta \dot{P} = \int_{V \setminus \Delta V_i} \phi(\nabla \mathbf{v}^0 + \nabla \tilde{\mathbf{v}}) dV - \int_{S_\sigma} \dot{\boldsymbol{\sigma}}^0 \cdot (\mathbf{v}^0 + \tilde{\mathbf{v}}) dS, \quad (4.97)$$

for the body on the right, where the incremental displacement gradient potential  $\phi$  is defined by eqn. (3.63).

Note that when quantity  $-\Delta \dot{P}$  is greater (smaller) than zero in eqns. (4.96) and (4.97), growth (reduction) of the inclusion is expected. This quantity can be obtained by subtracting eqn. (4.97) from eqn. (4.96) as

$$-\Delta \dot{P} = \int_{\Delta V_i} \phi(\nabla \mathbf{v}^0) dV - \int_{V \setminus \Delta V_i} \phi(\nabla \tilde{\mathbf{v}}) dV - \int_{V \setminus \Delta V_i} \tilde{\mathbf{t}}^T \cdot \nabla \mathbf{v}^0 dV + \int_{S_\sigma} \dot{\boldsymbol{\sigma}}^0 \cdot \tilde{\mathbf{v}} dS, \quad (4.98)$$

where T denotes the transpose.

We begin noting that  $\tilde{\mathbf{v}} = \mathbf{0}$  on  $S_v$ ; moreover, we extend the nominal stress field  $\tilde{\mathbf{t}}$  inside the rigid inclusion (which is always possible using incremental equilibrium stress fields), therefore the divergence theorem applied to the domain on the left of Fig. 4.17 yields

$$\int_{S_\sigma} \dot{\boldsymbol{\sigma}}^0 \cdot \tilde{\mathbf{v}} dS = \int_V \tilde{\mathbf{t}}^T \cdot \nabla \mathbf{v}^0 dV, \quad (4.99)$$

where, as  $\phi(\nabla \mathbf{v})$  in eqn. (3.63)<sub>2</sub> is a biquadratic form, the equality

$$\mathbf{t}^{0T} \cdot \nabla \tilde{\mathbf{v}} = \tilde{\mathbf{t}}^T \cdot \nabla \mathbf{v}^0, \quad (4.100)$$

has been exploited. We therefore arrive at

$$-\Delta \dot{P} = \int_{\Delta V_i} \phi(\nabla \mathbf{v}^0) dV - \int_{V \setminus \Delta V_i} \phi(\nabla \tilde{\mathbf{v}}) dV + \int_{\Delta V_i} \tilde{\mathbf{t}}^T \cdot \nabla \mathbf{v}^0 dV. \quad (4.101)$$

---

<sup>14</sup>The rigidification could for instance be obtained in a porous material through infiltration of a resin.

Noting again that the field  $\dot{\mathbf{t}}$  extended into the rigid inclusion makes the field  $\tilde{\mathbf{t}}$  equilibrated at every point and that  $\mathbf{v}^0$  is a rigid-body incremental displacement within the inclusion  $V_i$ , we have

$$\int_{\Delta V_i} \tilde{\mathbf{t}}^T \cdot \nabla \mathbf{v}^0 dV = -2 \int_{\Delta V_i} \phi(\nabla \mathbf{v}^0) dV. \quad (4.102)$$

Since  $\tilde{\boldsymbol{\sigma}} = \tilde{\mathbf{t}}^T \mathbf{n} = \mathbf{0}$  on  $S_\sigma$ , application of the divergence theorem to the domain on the right of Fig. 4.17 provides

$$- \int_{V \setminus \Delta V_i} \phi(\nabla \tilde{\mathbf{v}}) dV = \frac{1}{2} \int_{S_i^* \cup \Delta S_i^*} \tilde{\mathbf{t}}^T \mathbf{n} \cdot \mathbf{v}^0 dS, \quad (4.103)$$

obtaining finally

$$-\Delta \dot{P} = - \int_{\Delta V_i} \phi(\nabla \mathbf{v}^0) dV + \frac{1}{2} \int_{S_i^* \cup \Delta S_i^*} \tilde{\mathbf{t}}^T \mathbf{n} \cdot \mathbf{v}^0 dS. \quad (4.104)$$

Note that eqn. (4.104) is valid both for compressible and incompressible materials since  $\dot{p}$  in eqn. (3.63) is workless.

*Eqn. (4.104) represents the incremental potential energy decrease for a growth of a rigid inclusion in an elastic, incompressible or compressible body, generically anisotropic and prestressed. It is transparent from eqns. (4.103) and (4.104), that the incremental potential energy decrease is negative, implying a reduction of the inclusion, when the Hill exclusion condition (2.20) holds true.*

Note that the second integral on the right hand side of eqn. (4.104) is extended on the whole rigid inclusion (having an external surface  $S_i^* \cup \Delta S_i^*$ ). To keep contact with the analogous void problem, it is expedient now to re-write eqn. (4.104) with reference to the surface  $\Delta S_i$  enclosing the volume  $\Delta V_i$ , namely

$$-\Delta \dot{P} = - \int_{\Delta V_i} \phi(\nabla \mathbf{v}^0) dV + \frac{1}{2} \int_{\Delta S_i} \tilde{\mathbf{t}}^T \mathbf{n} \cdot \mathbf{v}^0 dS, \quad (4.105)$$

and split the incremental displacement field as

$$\mathbf{v}^0 = \mathbf{v}^* + \hat{\mathbf{v}}, \quad (4.106)$$

where  $\mathbf{v}^*$  vanishes inside the rigid inclusion  $V_i$  and  $\hat{\mathbf{v}}$  is the rigid body incremental displacement of the inclusion extended to the whole body  $V$ . The

incremental potential energy decrease is not affected by  $\hat{\mathbf{v}}$ , while, in the second term of eqn. (4.105) the integral along  $\Delta S_i \setminus \Delta S_i^*$  is null because  $\mathbf{v}^*$  vanishes there. We therefore obtain

$$-\Delta \dot{P} = - \int_{\Delta V_i} \phi(\nabla \mathbf{v}^*) dV + \frac{1}{2} \int_{\Delta S_i^*} \tilde{\mathbf{t}}^T \mathbf{n} \cdot \mathbf{v}^* dS. \quad (4.107)$$

*Eqn. (4.107) represents the incremental potential energy decrease for a growth of a rigid inclusion in an elastic (incompressible or compressible, generically anisotropic and prestressed) body, expressed analogously to the corresponding expression in the void problem [see Rice, 1968, his eqn. (55), p. 207].*

Turning now the attention to a thin rigid body, namely, a stiffener, the volume integral in eqn. (4.104) vanishes, so that taking the limit of the length increase  $\Delta l \rightarrow 0$  at fixed incremental stress intensity factor  $\dot{K}$ , eqn. (4.107) becomes

$$\dot{G} = - \frac{d\dot{P}}{dl} = - \lim_{\Delta l \rightarrow 0} \frac{1}{2\Delta l} \int_0^{\Delta l} [[\hat{t}_{2i}(\Delta l - r, \pi)]] \hat{v}_i(r, 0) dr, \quad (4.108)$$

where the symbol  $\hat{\cdot}$  denotes that we are using the inclined stiffener solution, the repeated index is summed, the brackets  $[[\cdot]]$  denote the jump in the relevant argument across the stiffener,  $r$  denotes the radial distance from the stiffener tip and 0 and  $\pi$  indicate values of the polar coordinate (anticlockwise) angle singling out  $r$  from the  $\hat{x}_1$  axis (so that  $\vartheta = 0$  corresponds to points ahead of the stiffener tip, see Fig. 3.2 in which the crack should be thought to represent a stiffener). Eqn. (4.108) defines

*the incremental energy release rate for a mixed mode growth of a stiffener in an elastic, incompressible or compressible body, generically anisotropic and prestressed.*

The proof that the incremental energy release rate (4.108) coincides with the path-independent incremental  $\dot{J}$ -integral (3.65) has not yet been explicitly obtained, but the validity of  $\dot{G} = \dot{J}$  has been verified numerically.

#### 4.4.1 Stiffener parallel to the orthotropy axis

For a stiffener aligned with respect to the principal stress axis  $x_1$  ( $\vartheta_0 = 0$ ), the incremental energy release rate (4.108), due to the symmetry, can be written as

$$\dot{G}_I = - \lim_{\Delta l \rightarrow 0} \frac{1}{\Delta l} \int_0^{\Delta l} \dot{t}_{21}(\Delta l - r, \pi) v_1(r, 0) dr, \quad (4.109)$$

for Mode I loading and

$$\dot{G}_{II} = - \lim_{\Delta l \rightarrow 0} \frac{1}{\Delta l} \int_0^{\Delta l} \dot{t}_{22}(\Delta l - r, \pi) v_2(r, 0) dr, \quad (4.110)$$

for Mode II loading (note the differences with the analogous formulae for fracture mechanics, see Cristescu et al. 2004).

In the absence of prestress and for compressible isotropic elasticity, the available expression for energy release rate for stiffener growth (Wang et al. 1985) is not similar to that corresponding to fracture growth. Employing our definition (4.23) of stress intensity factors, it becomes now possible to express the energy release rate for stiffener growth in a form strictly similar to that known for a fracture, which is obtained for the infinitesimal theory in appendix E. That expression can be generalized for incremental deformations superimposed upon a given homogeneous state of stress using the asymptotic analysis derived in §4.1.1 as

$$\dot{G} = - \frac{\dot{K}_{(\epsilon)I}^2 \sqrt{1-k} + \dot{K}_{(\epsilon)II}^2 \sqrt{1+k}}{4\sqrt{2}\mu} \sqrt{2\xi - 1 + \sqrt{1-k^2}}, \quad (4.111)$$

valid in both the EI and EC regimes and independent of  $\eta$ . Note that the negative sign in eqn. (4.111) shows that:

*reduction of the stiffener is always predicted.*

The incremental energy release rate (4.111) is represented in Fig. 4.18 for Mooney-Rivlin material (upper part) and  $J_2$ -deformation theory material (lower part) as a function of the prestress parameter  $k$  in the former case and of the prestrain parameter  $\epsilon$  in the latter.

The most interesting feature emerging from Fig. 4.18 is that  $\dot{G}$  always vanishes at the EC/H boundary, eqn. (2.62).

At the EI/P boundary the situation is more complicated, so that  $\dot{G}$  becomes null at  $k = 1$  and  $k = -1$  for Mode I and Mode II, respectively, but

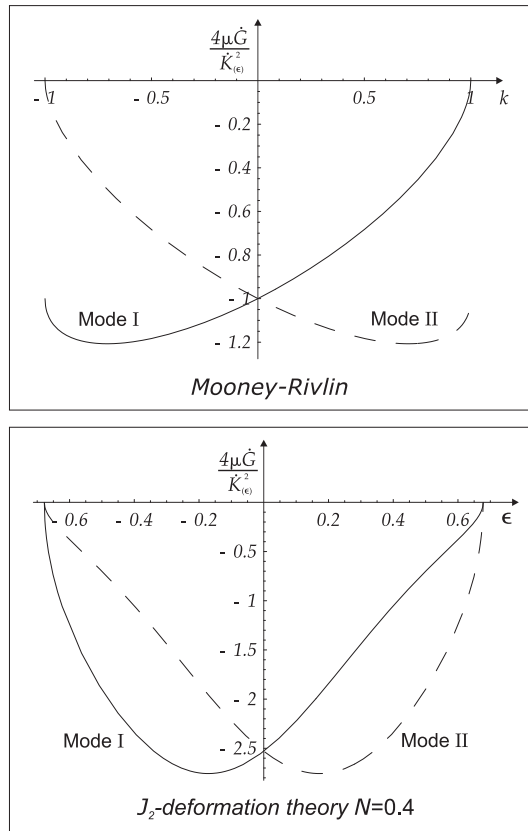


Figure 4.18: Incremental energy release rate in a Mooney-Rivlin (upper part) and a  $J_2$ -deformation theory (lower part) material. Note that the incremental release rate always vanishes at the EC/H boundary, except for Mooney-Rivlin material at  $k = -1$  for Mode I and  $k = 1$  for Mode II.

remains different from zero in the other cases. This conclusion can be reached solving eqn. (4.111) for  $k = \pm 1$ , which gives

$$\dot{G} = -\frac{\sqrt{2\xi - 1}}{4\mu} \times \begin{cases} \dot{K}_{(\epsilon)II}^2 & \text{for } k = 1, \\ \dot{K}_{(\epsilon)I}^2 & \text{for } k = -1. \end{cases} \quad (4.112)$$

Note that when the incremental energy release rate vanishes, reduction of the stiffener is inhibited.

### 4.4.2 The inclined stiffener

The asymptotic fields for a stiffener inclined with respect to the prestress axis (§4.2) result (constant terms have been neglected)

$$\begin{aligned}
[[\hat{t}_{21}(\Delta l - r, \pi)]] &= -\hat{v}_{2,2}^{\infty} \frac{\sqrt{2l}}{\sqrt{\Delta l - r}} \hat{\mathbb{G}}_{2121} \text{Im}[W_1^2 D_1 + W_2^2 D_2], \\
[[\hat{t}_{22}(\Delta l - r, \pi)]] &= -\hat{v}_{2,2}^{\infty} \frac{\sqrt{2l}}{\sqrt{\Delta l - r}} \left\{ 2(\hat{\mathbb{G}}_{2221} - \hat{\mathbb{G}}_{2111}) \text{Im}[W_1^2 D_1 + W_2^2 D_2] \right. \\
&\quad \left. - \hat{\mathbb{G}}_{2121} \text{Im}[W_1^3 D_1 + W_2^3 D_2] \right\}, \\
\hat{v}_1(r, 0) &= -\hat{v}_{2,2}^{\infty} \sqrt{2lr}, \\
\hat{v}_2(r, 0) &= -\Gamma \hat{v}_{2,2}^{\infty} \sqrt{2lr},
\end{aligned} \tag{4.113}$$

from which the incremental energy release rate for stiffener growth (4.108) can be calculated in the form

$$\begin{aligned}
\dot{G}_I &= -\frac{\dot{K}_{(\epsilon)I}^2}{8\mu^2} \left\{ \left[ \hat{\mathbb{G}}_{2121} + 2\Gamma(\hat{\mathbb{G}}_{2221} - \hat{\mathbb{G}}_{2111}) \right] \text{Im}[W_1^2 D_1 + W_2^2 D_2] \right. \\
&\quad \left. - \Gamma \hat{\mathbb{G}}_{2121} \text{Im}[W_1^3 D_1 + W_2^3 D_2] \right\}.
\end{aligned} \tag{4.114}$$

We have numerically checked that:

- i)  $\dot{G}_I$  is independent of  $\eta$ ;
- ii)  $\dot{G}_I$  is always negative in the elliptic regime, so that stiffener reduction is predicted.

The behaviour of the incremental energy release rate for a stiffener embedded in a  $J_2$ -deformation theory material is reported in Fig. 4.19 as a function of the amount of shear  $\gamma$ , for different values of the hardening parameter  $N$ . It should be noted from the figure that the maximum of the curves always occurs at null shear  $\gamma = 0$  for every  $N$ , and that

*at ellipticity loss the incremental energy release rate vanishes, so that stiffener reduction is inhibited.*

Note that  $\mu$  is a function of  $\gamma$  and, in particular,  $\mu$  tends to infinite when  $\gamma$  tends to zero. We have selected to normalize the plot through multiplication

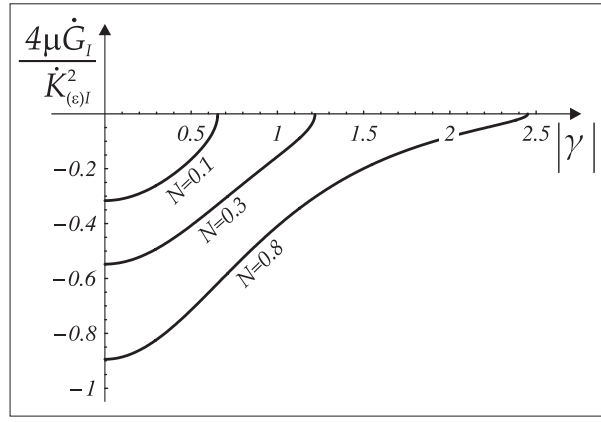


Figure 4.19: Mode I incremental energy release rate for a stiffener embedded in a  $J_2$ -deformation theory material subjected to a finite shear parallel to the stiffener line and defined by the shear amount parameter  $\gamma$ . Different hardening parameters  $N$  are considered.

by  $\mu/\dot{K}_{(\epsilon)I}^2$  to recover linear elasticity results in the special case of absence of prestress (where the  $J_2$ -deformation theory of plasticity loses meaning and our plot refers to an elastic orthotropic material with orthotropy axes inclined at  $45^\circ$  with respect to the stiffener line).

To understand the reasons for the vanishing or not of the incremental energy release rate, it becomes instrumental to digress now on the evaluation of the incremental axial force along the stiffener. Since a full-field solution is needed and this has been found for Mode I (since for Mode II the stiffener is neutral), the following analysis is restricted to this condition.

#### 4.4.3 The incremental axial force in the stiffener under Mode I perturbation

##### Stiffener parallel to an orthotropy axis

Using the expressions for the nominal shear stress increments obtained in §4.1.3 into the definition of incremental axial force in the stiffener, eqn. (4.3)<sub>1</sub>, we get

$$\dot{N}(x_1) = -2\sqrt{2}\mu v_{2,2}^{(\infty)}\sqrt{1-k}\sqrt{2\xi-1+\sqrt{1-k^2}}\sqrt{l^2-x_1^2}, \quad (4.115)$$

valid in both the EI and EC regimes and independent of  $\eta$ .

Values of the incremental axial force in the stiffener  $\dot{\mathcal{N}}$  (divided by  $4\mu v_{1,1}^{(\infty)}$  so that a dilatation parallel to the stiffener is considered) are reported in Fig. 4.20 for Mooney-Rivlin material and  $J_2$ -deformation theory material, with  $N = 0.4$ , for different values of prestress in the former case and logarithmic prestrain in the latter.

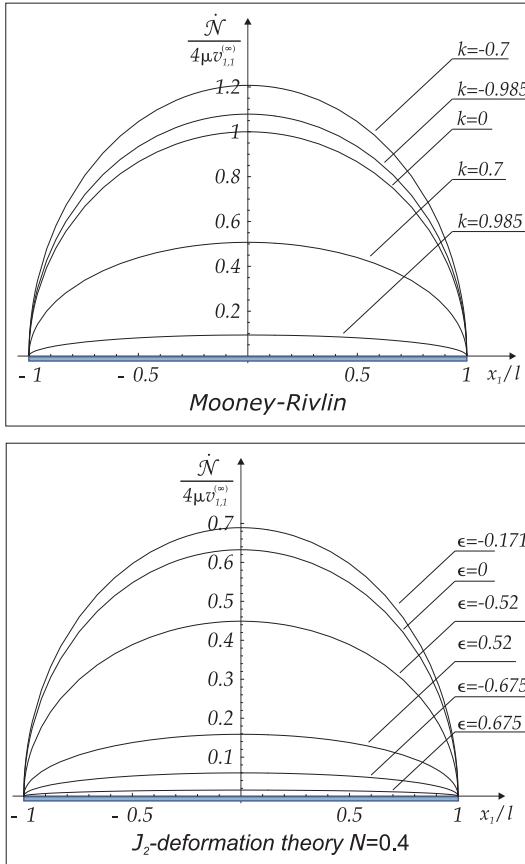


Figure 4.20: The incremental axial force in a stiffener embedded in a prestressed Mooney-Rivlin material (upper part, for different values of prestress  $k$ ) and in a  $J_2$ -deformation theory material (lower part, for different values of logarithmic prestrain  $\epsilon$ ). Note that the incremental axial force in the stiffener vanishes at the elliptic boundary ( $k = 1$  for Mooney-Rivlin and  $\epsilon^{EL} \simeq \pm 0.6778$  for  $J_2$ -deformation theory).

It can be noted from Fig. 4.20 and, more precisely, from eqn. (4.115) that:

- i) the maximum incremental axial force in the stiffener is always attained

at  $x_1 = 0$ ;

ii) the incremental axial force in the stiffener vanishes

- always at the EC/H boundary;
- when  $k = 1$  at the EI/P boundary.

In other words, the incremental axial force does not vanish only at the EI/P boundary when  $k = -1$ .

The last of the above points can be explained considering that at the EI/P boundary, with  $k = -1$ , a shear band forms *orthogonally* to the stiffener tips, so that this can continue to carry an axial load.

Now we are in a position to set the relation (for a uniform Mode I loading) between the incremental energy release rate,  $\dot{G}_I$ , and the maximum value of the incremental axial force in the stiffener

$$\dot{\mathcal{N}}_{max} = \dot{\mathcal{N}}(x_1 = 0), \quad (4.116)$$

[where  $\dot{\mathcal{N}}$  is given by eqn. (4.115)] which indeed can be obtained as

$$\dot{G}_I = \frac{\pi v_{2,2}^{(\infty)}}{4} \dot{\mathcal{N}}_{max}. \quad (4.117)$$

### Inclined stiffener

The jump of the perturbed shear nominal traction increment (§4.2) can be evaluated to be

$$[[\hat{t}_{21}(\hat{x}_1, 0)]] = -2\hat{v}_{2,2}^{\infty} \hat{\mathbb{G}}_{2121} \text{Im}[W_1^2 D_1 + W_2^2 D_2] \frac{\hat{x}_1}{\sqrt{l^2 - \hat{x}_1^2}}, \quad \forall |\hat{x}_1| < l, \quad (4.118)$$

so that, using the identity (4.84) (that has only been numerically checked to hold), the incremental axial force in the stiffener related to a Mode I loading is

$$\dot{\mathcal{N}}(\hat{x}_1) = -2\hat{v}_{2,2}^{\infty} \hat{\mathbb{G}}_{2121} \text{Im}[W_1 + W_2 + \Gamma W_1 W_2] \sqrt{l^2 - \hat{x}_1^2}, \quad \forall |\hat{x}_1| < l, \quad (4.119)$$

resulting again independent of the in-plane mean stress, parameter  $\eta$ .

Note that the maximum of the axial force always occurs at the stiffener centre and we have numerically verified that the incremental maximum axial force is related to the incremental energy release rate by eqn. (4.117), which

is always negative in the elliptic regime, so that the stiffener is subject to compression for positive  $\hat{v}_{2,2}^\infty$ .

Eqn. (4.117) explains the fact that the incremental Mode I energy release rate vanishes if and only if the incremental maximum axial force vanishes too, a circumstance clarifying the conditions for annihilation or not of stiffener reduction.



## Chapter 5

---

### Shear band in a prestressed material

*A weak line inclusion model in a nonlinear elastic solid is proposed to analytically quantify and investigate the stress state and the growth conditions of a finite-length pre-existing shear band in a prestressed material. The deformation is shown to become highly focussed and aligned coaxial to the shear band—a finding that provides justification for the experimentally observed strong tendency towards rectilinear propagation—and the energy release rate to blow up to infinity, for incremental loading occurring when the prestress approaches the elliptic boundary. It is concluded that the propagation becomes ‘unrestrainable’, a result substantiating the experimental observation that shear bands are preferential near-failure deformation modes.*

Localized deformations in the form of shear bands emerging from a slowly varying deformation field are known to be preferential near-failure deformation modes of ductile materials (for instance, Bei et al., 2006; Lewandowski and Greer, 2006; Rittel et al., 2006; Fenistein and van Hecke, 2003). Therefore, shear band formation is the key concept to explain failure in many materials and, accordingly to its theoretical and ‘practical’ importance, it has been the focus of an enormous research effort in the last thirty years. From the theoretical point of view, this effort has been mainly directed in two ways,<sup>1</sup> namely, the dissection of the specific constitutive features responsible for strain

---

<sup>1</sup>Features of strain localization occurring *after* its onset, have scarcely been theoretically explored. For instance, there is almost nothing about post-localization behaviour. Research devoted to this topic has been developed by Gajo et al. (2004), Hutchinson and Tvergaard (1981), Petryk and Thermann (2002) and Tvergaard (1982).

localization in different materials,<sup>2</sup> and the struggle for the overcoming of difficulties connected with numerical approaches.<sup>3</sup> Although these problems still seem far from being definitely solved, the most important questions in this research area have only marginally been approached and are therefore still awaiting explanation. These are the following.

- i) The highly inhomogeneous stress/deformation state developing near a shear band tip is unknown from analytical point of view (and numerical techniques can hardly have the appropriate resolution to detail this).
- ii) It is not known if a shear band tip involves a strong stress concentration.
- iii) The fact that shear bands grow quasi-statically and *rectilinearly* for remarkably long distances under mode II loading conditions, while the same feature is not observed in the akin problem of crack growth, remains unexplained.
- iv) Finally, and most important, the reason why shear bands are preferential failure modes for quasi-statically deformed ductile materials has no justification.

Surprisingly, analytical investigation of the above problems and even of the stress field generated by a finite-length shear band, possibly including near-tip singularities, has never been attempted. Moreover, shear band growth has been considered only in a context pertaining to slope-stability problems in soil mechanics (Palmer and Rice, 1973; Rice, 1973), an approach recently developed by Puzrin and Germanovich (2005).

A full-field solution is given for a finite-length shear band in an anisotropic, prestressed, nonlinear elastic material, incrementally loaded under mode II and revealing: stress singularity, highly inhomogeneity of the deformation and its focussing parallel and coaxially aligned to the shear band. Moreover, the incremental energy release rate is shown to blow up when the stress state approaches the condition for strain localization (i.e. the elliptic boundary). These general findings are applied to the so-called ‘ $J_2$ -deformation theory material’ (see appendix B.2) and provide justification to the above-mentioned aspects of shear banding in ductile materials.

---

<sup>2</sup>This line of research has been initiated by Rudnicki and Rice (1975) and developed in a number of directions [including: gradient effects (Aifantis, 1987; Aifantis and Willis, 2005), temperature effects (Benallal and Bigoni, 2004; Gioia and Ortiz, 1996), anisotropy effects (Bigoni and Loret, 1999), and yield-vertex effects (Petryk and Thermann, 2002)].

<sup>3</sup>Reviews on the numerical work developed in these years have been given by Needleman and Tvergaard (1983) and Petryk (1997).

## 5.1 The shear band model

An infinite, incompressible elastic material obeying to constitutive equations (2.6) is considered homogeneously and quasi-statically deformed in a given loading path directed toward the elliptic boundary. Inspired by the experimental observation that the sensibility of a material to shear banding is linked to pre-existing defects (Xue and Gray, 2006), we assume that there is an imperfection present in the material, in the form of a thin zone of ‘weak’ material, which touches the EI/P or EC/H boundary and is transformed into a shear band of length  $2l$ , while the surrounding material is still in the elliptic regime, although near the boundary of ellipticity loss. In this situation, we analyze the response to an incremental loading perturbation, with the purpose of determining the stress state near a finite-length shear band and on the shear band growth conditions.

A shear band is a thin layer of material across which certain components of the incremental nominal tractions vanish, namely, the incremental nominal shear component tangential to the shear band, for the material model (2.6) considered here. It becomes therefore spontaneous to model a shear band in such a material as a ‘slip discontinuity surface’ across which the normal component of incremental displacement remain continuous, while the tangential incremental nominal stress component vanishes (Fig. 5.1). Such a

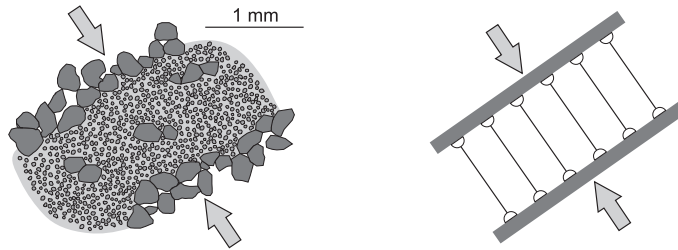


Figure 5.1: Sketch of a weak interface (right) to model a shear band (left, inspired by a deformation band observed in dry sandstone by Sulem and Ouffroukh, 2006). The hinged quadrilateral should be thought to have zero thickness, so that materials in contact can freely slide incrementally along a weak surface, across which normal incremental displacement remains continuous.

discontinuity surface is not a crack, since normal incremental tractions can be transmitted across it, but it can behave equivalently to a crack in certain special symmetry conditions. This is the case when the shear band is aligned parallel to one of the principal orthotropy axes  $x_1$  or  $x_2$ , corresponding either

to a shear band formed at the EI/P boundary or to a shear band formed at the EC/H boundary at  $\xi = 0$  (where two shear bands orthogonal to each other form simultaneously). In these cases, the slip surface model behaves as a crack when subject to a Mode II loading increment and can be directly analyzed with the solution developed in §3.1. In a more general case, a solution for a slip surface embedded in a prestressed material has to be developed and is proposed below.

We analyze the symmetry case corresponding to the EI/P boundary, in which shear band and crack are equivalent models, and the generic situation, corresponding to the EC/H boundary.

In summary, for the proposed weak line model of a shear band of length  $2l$  aligned with respect to  $\hat{x}_1$ -axis (and centered at its origin, see Fig. 5.2), the incremental boundary conditions on the shear band surfaces are:

- null incremental nominal shearing tractions,

$$\hat{t}_{21}(\hat{x}_1, 0^\pm) = 0, \quad \forall |\hat{x}_1| < l; \quad (5.1)$$

- continuity of the incremental nominal normal traction,

$$[[\hat{t}_{22}(\hat{x}_1, 0)]] = 0, \quad \forall |\hat{x}_1| < l; \quad (5.2)$$

- continuity of normal incremental displacement,

$$[[\hat{v}_2(\hat{x}_1, 0)]] = 0, \quad \forall |\hat{x}_1| < l; \quad (5.3)$$

where the brackets  $[[\cdot]]$  denotes the jump in the relevant argument, taken across the shear band.

Before to proceed with the analysis, a digression becomes necessary. It is assumed in our model setting that a sliding surface abruptly forms when a weak thin zone of material touches the elliptic boundary. This model is obviously a strong idealization, since in reality the weak material approaches the elliptic boundary becoming incrementally less and less stiff in a continuous way. The abrupt formation of a sliding surface within an infinite solid may, depending on the stress conditions, generate a sudden ‘spurious’ interfacial instability, so that in this condition the shear band model becomes oversimplified. Therefore, we have to limit the analysis to situations in which all instabilities are a-priori excluded until the elliptic boundary is met, as is the case when the Hill exclusion condition, eqn. (2.20), holds true. Fortunately,

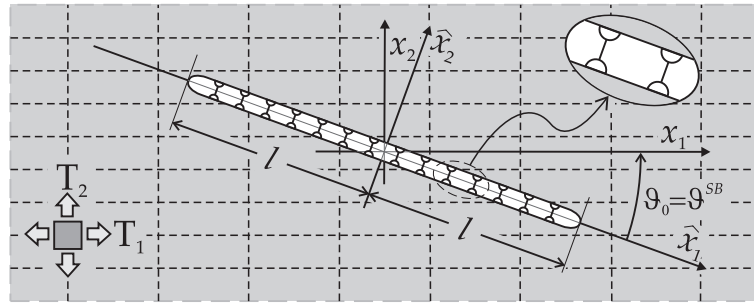


Figure 5.2: Shear band of length  $2l$  in a prestressed, orthotropic material inclined at an angle  $\vartheta_0$  (positive when anticlockwise) with respect to the orthotropy axes  $x_1$  and  $x_2$ .  $T_1$  and  $T_2$  denote the prestress state, expressed through the two in-plane principal Cauchy stresses aligned parallel to the  $x_1$ - $x_2$  reference system.

this condition is so general that all points of the EC/H and EI/P can be explored (by selecting appropriate values for  $\eta$ , to enforce the validity of the Hill exclusion condition until the elliptic boundary is touched for the given loading path, see Fig. 2.8).

## 5.2 The stress state near a shear band and its propagation

### 5.2.1 Shear band at the EI/P boundary

All points of the elliptic imaginary/parabolic boundary can be approached while the Hill exclusion condition holds true when  $\eta = k > 0$ , corresponding to a uniaxial tensile stress state,  $T_1 > 0$ ,  $T_2 = 0$ . In this situation, one shear band forms at the EI/P boundary,  $k = 1$ , parallel to the tensile loading direction (2.58) so that the problem is symmetric and the crack solution, eqns. (3.37) and (3.38), can be used. In fact, due to symmetry, the normal displacement increment and all nominal incremental traction components are null (and therefore a fortiori continuous) at the shear band boundary, under a Mode II loading increment.

Eqns. (3.37) have been used to obtain results shown in Fig. 5.3, where the level sets of incremental deviatoric strain are reported at different levels of prestress, namely, at null prestress,  $k = 0$ , and at  $k = 0.95$ , a value very close to the EI/P boundary. Results similar to those obtained in Fig. 5.3, but

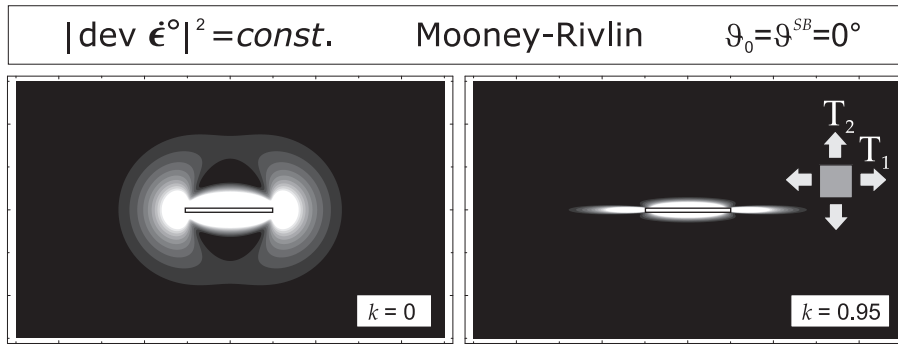


Figure 5.3: Interaction of shear bands and mechanical fields near a shear band of length  $2l$  (evidenced with a thin rectangle, providing the scale bar of the representation) in an incrementally isotropic,  $\xi = 1$ , material without prestress,  $k = 0$ , and prestressed near the EI/P boundary,  $k = \eta = 0.95$ . Incremental Mode II loading is considered.

limited to fields near the tip of the shear band can also be obtained employing the asymptotic analysis presented by Radi et al. (2002).

It should be noticed from Fig. 5.3, that the incremental deformation field evidences a strong focussing in the direction of the shear band. Moreover, the incremental energy release rate for shear band growth can be deduced from the formula for crack advance under Mode II, eqn. (3.69). The energy released for an incremental advance of shear band has the typical behaviour shown in Fig. 3.8 (for Mode II and  $\vartheta_0 = 0$ ), evidencing an asymptote at the EI/P boundary (there are no qualitative changes when other values of the parameter  $\xi \geq 0.5$  are considered, so that the asymptote at  $k = 1$  is always present).

### 5.2.2 Shear band at the EC/H boundary

According to eqn. (2.54), at the EC/H boundary two shear bands form inclined with respect to the  $x_1$ - $x_2$  axes, so that one of these is taken aligned parallel to the  $\hat{x}_1$ -axis inclined at  $\vartheta^{SB}$  with respect the  $x_1$ -axis.<sup>4</sup> Using the weak line model, only Mode II loading plays a role, while a Mode I loading leaves the material unperturbed.

Therefore, with reference to Fig 5.2 and employing a representation similar

<sup>4</sup>The analysis can be carried with respect to a generic, uniform state of prestress with principal values inclined at  $\vartheta_0$  different from  $\vartheta^{SB}$ .

to (3.47), namely,

$$\hat{\psi}^\circ(\hat{x}_1, \hat{x}_2) = \frac{\hat{t}_{21}^\infty}{2\mu} \sum_{j=1}^2 \operatorname{Re} \left\{ B_j^{II} \left[ \hat{z}_j^2 - \hat{z}_j \sqrt{\hat{z}_j^2 - l^2} + l^2 \ln \left( \hat{z}_j + \sqrt{\hat{z}_j^2 - l^2} \right) \right] \right\}, \quad (5.4)$$

and imposing the boundary conditions (5.1)–(5.3) at a sliding surface yields the following algebraic system for the unknown constants  $B_j^{II}$

$$\begin{bmatrix} -c_{21} & c_{11} & -c_{22} & c_{12} \\ c_{31} & c_{41} & c_{32} & c_{42} \\ -c_{41} & c_{31} & -c_{42} & c_{32} \\ 0 & 1 & 0 & 1 \end{bmatrix} \begin{bmatrix} \operatorname{Re}[B_1^{II}] \\ \operatorname{Im}[B_1^{II}] \\ \operatorname{Re}[B_2^{II}] \\ \operatorname{Im}[B_2^{II}] \end{bmatrix} = \begin{bmatrix} 0 \\ -1 \\ 0 \\ 0 \end{bmatrix}, \quad (5.5)$$

where coefficients  $c_{ij}$  are again those defined by eqns. (3.53). The determinant of the coefficient matrix in eqn. (5.5) vanishes both when the surface bifurcation condition, eqn. (2.66) or (3.46), is met and at the EC/H boundary.

Similarly to the crack solution, the asymptotic fields near the shear band tip result for the incremental nominal stress to be given by

$$\hat{t}_{22}(r, 0) = -\frac{\Upsilon \dot{K}_{II}}{\sqrt{2\pi r}}, \quad \hat{t}_{21}(r, 0) = \frac{\dot{K}_{II}}{\sqrt{2\pi r}}, \quad (5.6)$$

ahead of the tip, where

$$\Upsilon = \frac{\hat{t}_{22}^\circ}{\hat{t}_{21}^\infty} = c_{11} \operatorname{Re}[B_1^{II}] + c_{12} \operatorname{Im}[B_1^{II}] + c_{13} \operatorname{Re}[B_2^{II}] + c_{14} \operatorname{Im}[B_2^{II}], \quad (5.7)$$

and for the incremental displacements (where constants have been neglected)

$$\begin{aligned} \hat{v}_1(\Delta l - r, \pm\pi) &= \pm \frac{\hat{t}_{21}^\infty \sqrt{2l} \sqrt{\Delta l - r}}{2\mu} \operatorname{Im} [W_1 B_1^{II} + W_2 B_2^{II}], \\ \hat{v}_2(\Delta l - r, \pm\pi) &= \mp \frac{\hat{t}_{21}^\infty \sqrt{2l} \sqrt{\Delta l - r}}{2\mu} \operatorname{Im} [B_1^{II} + B_2^{II}], \end{aligned} \quad (5.8)$$

holding at the shear band surfaces, for ‘small’  $\Delta l$ .

The following properties<sup>5</sup> of function  $\Upsilon$

$$\Upsilon(k=0, \vartheta_0) = \Upsilon(k, \vartheta_0=0) = \Upsilon(k, \vartheta_0=\pi/2) = 0, \quad (5.9)$$

<sup>5</sup>Note the similarity of eqns. (5.9), (5.10) with eqn. (4.85).

have been proven, while the properties

$$\Upsilon = \Upsilon(k, \vartheta_0) = -\Upsilon(-k, \pi/2 - \vartheta_0), \quad (5.10)$$

have been numerically found to hold, from which the identities

$$\Upsilon(k, \vartheta_0 = \pi/4) = \frac{1 - \sqrt{1 - k^2}}{k}, \quad \Upsilon(k, \vartheta_0 = \pi/3) = \frac{\sqrt{3}(2 + k - 2\sqrt{1 - k^2})}{4 + 5k}, \quad (5.11)$$

follow with the help of a symbolic manipulator.

Employing the asymptotic near-tip representations (5.6) and (5.8) in eqn. (3.64) we obtain

$$\dot{G}^{SB} = \dot{K}_{II}^2 \frac{\text{Im} [W_1 B_1^{II} + W_2 B_2^{II}]}{4\mu}. \quad (5.12)$$

Note that the perturbed solution for the shear band model can be alternatively obtained providing a mixed mode loading to an inclined crack, in which the Mode I loading component is ‘calibrated’ with respect to the Mode II component in such a way to eliminate the jump in normal incremental displacement along the crack faces generated by a pure Mode II loading, in other words, to satisfy condition (5.3). All this procedure bears on the special feature found in the solution of the crack problem that a Mode I loading uniform along the crack faces is sufficient to eliminate a Mode II transversal mismatch in incremental displacements. In particular, eqn. (5.12) can be obtained from eqn. (3.68), considering a mixed mode defined by  $\hat{t}_{22}^\infty = -\Upsilon \hat{t}_{21}^\infty$ , so that the condition of continuity of transversal incremental displacement yields

$$\text{Im}[A_1^{II} + A_2^{II}] - \Upsilon \text{Im}[A_1^I + A_2^I] = 0, \quad (5.13)$$

and the constants defining the crack and shear band solutions are related through

$$B_j^{II} = A_j^{II} - \Upsilon A_j^I, \quad j = 1, 2. \quad (5.14)$$

Therefore, the difference between the crack and shear band problems lies in a uniform nominal normal stress increment applied at the crack surfaces.

Level sets of the modulus of incremental deviatoric strain for a  $J_2$ - deformation theory material (which is a particular case of the developed theory, see §B.2 and §2.2.2) are reported in Fig. 5.4 for low ( $N = 0.1$ ) – and in Fig. 5.5 for high ( $N = 0.8$ ) – strain hardening.

In both cases, null prestrain (and prestress) and a value of prestrain near the EC/H boundary have been considered. Moreover, parameter  $\eta$  has been taken equal to  $0.311 k$  for  $N = 0.1$  and equal to  $0.775 k$  for  $N = 0.8$ , to ensure

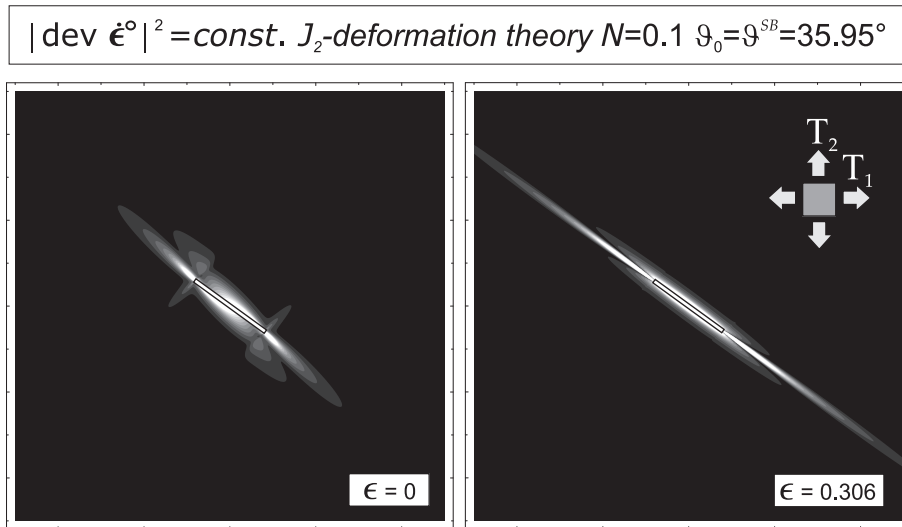


Figure 5.4: Interaction of shear bands and mechanical fields near a shear band of length  $2l$  (evidenced with a thin rectangle, providing the scale bar of the representation) in a  $J_2$ -deformation theory material at low ( $N = 0.1$ ) strain hardening, not prestrained ( $\varepsilon = 0$ , on the left), and near the EC/H boundary ( $\varepsilon = 0.306$ , on the right).

the validity of the Hill exclusion condition (2.20) near the EC/H boundary. Note that, for null prestrain  $\varepsilon = 0$ , the shear band model behaves as a fracture, since the normal component of incremental displacement remains continuous for a crack in an orthotropic, incompressible material at null prestress. Therefore, Figs. 5.4 and 5.5 (left) are identical to the analogue cases reported in Figs. 3.4 and 3.5 (upper parts, right). The difference between the shear band model and the crack becomes evident comparing Figs. 3.4 and 3.5 (lower parts, right) with Figs. 5.4 and 5.5 (right), where in the former figures both conjugate directions of shear bands are activated under Mode II loading, while only the direction aligned to the shear band is activated in the latter case.

We can conclude from Figs. 5.4 and 5.5 that:

*the incremental deformation field near a finite-length shear band is localized, elongated, and evidences a strong focussing in the direction aligned parallel to the shear band. This finding suggests that, while Mode II rectilinear crack propagation in a homogeneous material usually does not occur (since in first approximation cracks deviate from rectilinearity following the maximum near-tip hoop*

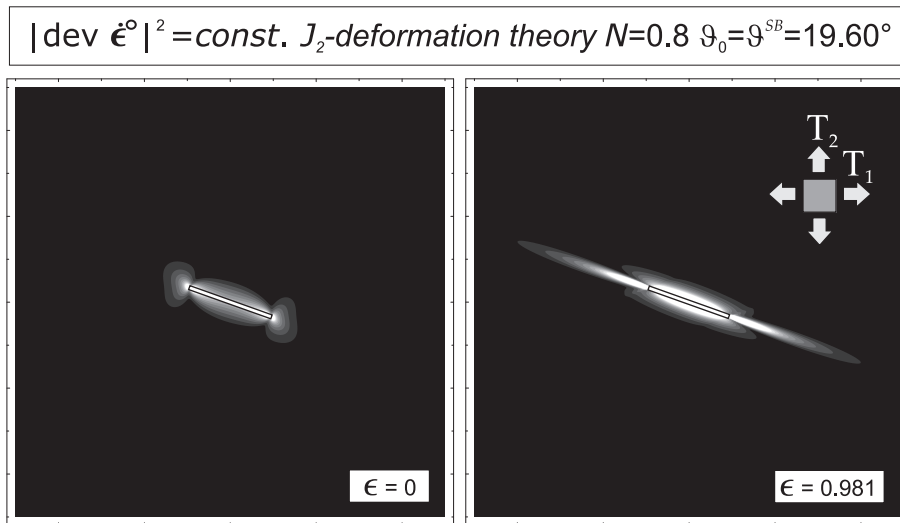


Figure 5.5: Interaction of shear bands and mechanical fields near a shear band of length  $2l$  (evidenced with a thin rectangle, providing the scale bar of the representation) in a  $J_2$ -deformation theory material at high ( $N = 0.8$ ) strain hardening, not prestrained ( $\varepsilon = 0$ , on the left), and near the EC/H boundary ( $\varepsilon = 0.981$ , on the right).

*stress inclination), shear band growth is very likely to occur aligned with the shear band itself. This observation explains the strong tendency that shear bands evidence toward rectilinear propagation for long (compared to their thickness) distances (see, for instance Anand and Spitzig, 1980; 1982). Moreover, the focussing of incremental deformation and the stress singularity strongly promote shear band growth.*

To further analyze shear band growth, *the incremental energy release rate for an infinitesimal shear band advance  $\dot{G}^{SB}$*  can be evaluated for an orthotropic prestressed material using eqn. (5.12) and it can be shown to blow up to infinity when the EC/H boundary is approached. In particular, calculations of the incremental energy release rate (made dimensionless by multiplication by  $4\mu/\dot{K}_{II}^2$ ) for shear band growth in a  $J_2$ -deformation theory material at low ( $N = 0.1$ ) and high ( $N = 0.8$ ) strain hardening are reported in Fig. 5.6, from which the following conclusion can be deduced.

*It is assumed in fracture mechanics that a crack advances under small scale yielding when the energy release rate exceeds a critical*

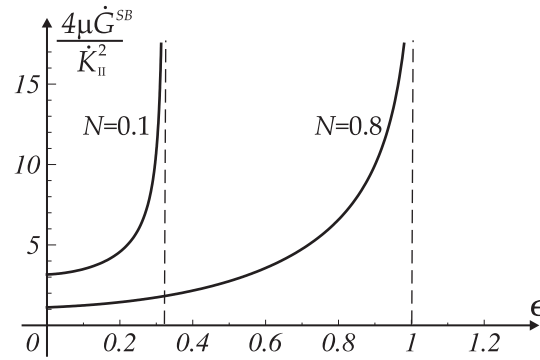


Figure 5.6: Incremental energy release rate for shear band growth in a  $J_2$ -deformation theory material at low ( $N = 0.1$ ) and high ( $N = 0.8$ ) strain hardening, as a function of the prestrain  $\epsilon$ . The curve presents an asymptote at the EC/H boundary ( $\epsilon^{EL} \simeq 0.322$ , for  $N = 0.1$  and  $\epsilon^{EL} \simeq 1.032$ , for  $N = 0.8$ ), so that shear band growth becomes ‘unrestrainable’ when prestress approaches this point.

*threshold, believed to be a characteristic of the material. Whether this criterion can be generalized to the present context or not can still be a matter of discussion, but the important point is that the incremental energy release rate blows up to infinity when the elliptic boundary is approached. In these conditions, a shear band can drive itself on and overcome possible barriers, in other words, can grow ‘unrestrainable’, a finding which, together with the previous results on near-tip stress/deformation states, legitimizes the common experimental observation that shear bands are preferred near-failure deformation modes.*



## Appendix A

---

### Experiments on two-component epoxy resin specimens embedding an aluminum thin platelet

A commercial two-part epoxy resin (Crystal Resin<sup>©</sup> by Gedeo, 305 Avenue du pic de Bretagne, 13420 Gemenos, France), commonly used for producing highly transparent non-yellowing casts has been employed to produce an elastic material enclosing a thin rigid lamina, to be used with transmission photoelasticity. Samples made with this resin have been de-moulded after twelve hours and tested after at least one week. To realize the stiffener, we have used a 0.3 mm thick aluminum sheet, which its superficial rugosity has been improved to enhance adhesion, using a fine (P 180) sandpaper. Seven samples have been produced, five of which are shown in Fig. A.1.

The square 100 mm × 100 mm × 18 mm sample (S3 in Fig. A.1) has a 44 mm × 18 mm × 0.3 mm aluminum platelet embedded and has been produced following the supplier's instructions, namely, mixing one part of hardener B with two parts of resin A. When solid, after ten days, the sample has been cut to obtain parallel edges and finally polished.

The thick rectangular 195 mm × 94.3 mm × 10.3 mm sample (S1) has a 20 mm × 10.3 mm × 0.3 mm aluminum platelet embedded and has been produced by mixing 1 part of hardener B with 1 part of resin A. In this way, a very soft material (deformed 40% longitudinally under a 0.196 MPa uniaxial mean stress at failure) has been obtained by direct casting, without any polishing.

All the other samples have been produced by mixing one part of hardener B with 2.25 parts of resin A.

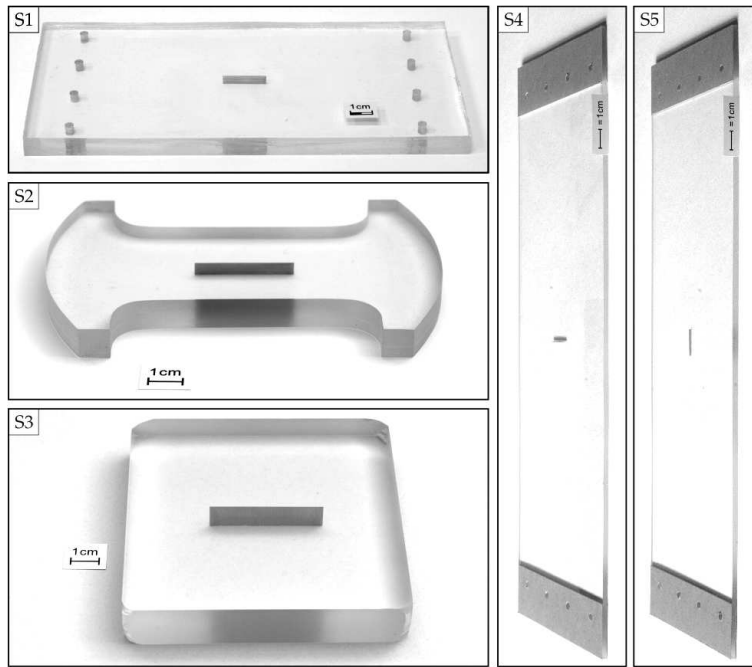


Figure A.1: The two-component epoxy resin samples with lamellar (aluminum) inclusions used in our tests. A rectangular thick sample (S1), a dog-bone shaped sample (S2), a square sample (S3), two rectangular thin samples (S4, S5) are shown.

The dog-bone shaped sample (S2), of thickness equal to 10.6 mm and transverse width of 39.5 mm, contains a  $30 \text{ mm} \times 10.6 \text{ mm} \times 0.3 \text{ mm}$  aluminum platelet. This sample has been cut from a circular disk sample of 115 mm diameter and finally polished.

The two rectangular  $340 \text{ mm} \times 100 \text{ mm} \times 3.2 \text{ mm}$  samples (S4, S5) contain a  $15 \text{ mm} \times 3.2 \text{ mm} \times 0.3 \text{ mm}$  aluminum platelet (parallel to the long sides in one sample and orthogonal in the other) and have been obtained by direct casting into a mould, without any further treatment.

The sample S3 has been tested under compression orthogonal to the long edge of the stiffener by imposing a vertical displacement, obtained at constant velocity of 0.1 mm/min (a Galdabini PMA 10 universal testing machine has been used). After a photoelastic investigation of the stress state has been conducted at low stress, we have tried to break the sample in compression, to investigate cracking. The material has revealed a remarkable ductile be-

behaviour and the sample suffered an out-of-plane buckling. Therefore, the test was stopped after a large strain had occurred and before the final rupture. Interestingly, strain localization near the edges of the stiffener emerged and was made visible by reflected bright light used to illuminate the sample (Fig. 1.1).

The dog-bone shaped sample (S2) has been tested under tensile stress parallel to the long edge of the stiffener, by imposing a vertical displacement, obtained at constant velocity of 0.1 mm/min (a Galdabini PMA 10 universal testing machine has been used). Photoelastic investigation has been performed up to near failure stress. The sample failed at a mean stress near 36 MPa. Before failure, an out-of-plane delamination started near the lower edge of the stiffener, due to Poisson effect. Subsequently, two nearly simultaneous fractures started to grow horizontally and perpendicularly to the stiffener (Fig. 1.3). Initial propagation was slow, so that a few minutes elapsed from when a first fracture was visible and the photo on the left in Fig. 1.3 was taken (so that 30 camera shots were manually taken when a fracture was already visible, before the photo on the left in Fig. 1.3 was taken). About a minute elapsed and 13 camera shots were taken between the photos shown on the left and on the centre were taken. No photos were taken between those shown centrally and on the right in Fig. 1.3.

The three rectangular samples (S1, S4, S5) have been loaded through the imposition of dead loadings, with tensile stresses parallel to the long sides. By means of a plane polariscope, a photoelastic investigation was performed on these samples at small stress (near 4 MPa for S4 and S5, and 11 kPa for S1) giving the best quality photos, approximately identical for the three tests (Fig. A.2). In particular, the isochromatic fringe patterns shown in Fig. 1.2 have been obtained on the soft, 10.3 mm thick rectangular sample (S1). Additional results are reported in Fig. A.2, where, in particular, photos reported on the left and central have been taken on sample (S1), while the photo reported on the right has been taken on the 3.2 mm thick sample (S5).

In general, we note that plane strain deformation prevails near the stiffener, while plane stress dominates at a sufficient distance from it, particularly in samples S1 and S2. The solution for a stiffener in plane stress and plane strain isotropic (compressible) elasticity can be derived taking the limit of null semi-axes ratio for the solution of a rigid elliptical inclusion in an infinite elastic sheet reported by Muskhelishvili (1953, §83a). This solution provides contour plots of the in-plane principal stress difference qualitatively similar to the plane strain case and also both solutions do not depend much on the

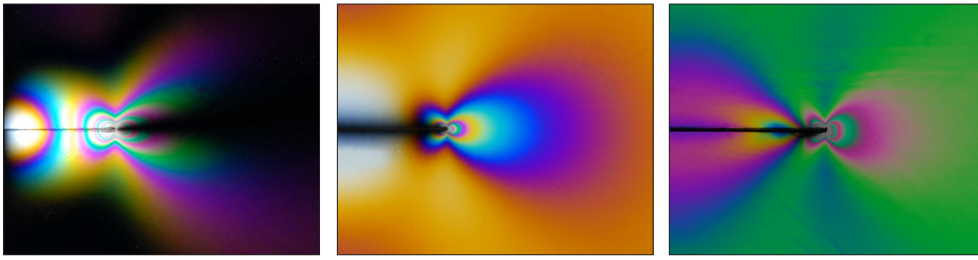


Figure A.2: Isochromatic fringe patterns captured in the photoelastic tests. Left: sample S1 at 51 kPa tensile mean stress (parallel to the stiffener); centre: sample S1 at 11 kPa tensile mean stress (parallel to the stiffener); right: sample S5 at 4.3 MPa tensile mean stress (orthogonal to the stiffener). In the left-hand side picture the axes of polarization are parallel and orthogonal to the stiffener, while these are rotated of  $\pi/4$  clockwise with respect to the other two.

Poisson's ratio. This explains the very good match between the theoretical results –referred to plane strain incompressible material– and the experiments shown in Fig. 1.2.

Although the rectangular samples provided the best photoelastic results, these analyses have been performed on all samples and always gave similar results. At very high stress, near failure under tensile stress for the dog-bone shaped specimen, the shape of the photoelastic contours evidenced details which might be better interpreted with our results for a prestressed material. However, since we had only a few of these data, we decided not to report them.

# Appendix B

---

## Material behaviour

An incompressible ( $\lambda_1\lambda_2\lambda_3 = 1$ ) hyperelastic material is defined by the constitutive relation

$$\mathbf{T}_i = \hat{p} + \lambda_i \frac{\partial W(\lambda_1, \lambda_2, \lambda_3)}{\partial \lambda_i}, \quad i = 1, 2, 3; \text{ no sum on index } i, \quad (\text{B.1})$$

where  $W$  is the strain energy density, function of the principal stretches  $\lambda_i$ , and  $\hat{p}$  represents the mean stress,

$$\hat{p} = \frac{\text{tr} \mathbf{T}}{3} = \frac{\mathbf{T}_1 + \mathbf{T}_2 + \mathbf{T}_3}{3}. \quad (\text{B.2})$$

### B.1 The Mooney-Rivlin material

The Mooney-Rivlin material (Mooney, 1940) is defined by the strain energy density function

$$W(\mathbf{B}) = \frac{\mu_1 \mathbf{I}_1(\mathbf{B}) - \mu_2 \mathbf{I}_2(\mathbf{B})}{2}, \quad (\text{B.3})$$

where  $\mathbf{I}_1(\mathbf{B})$  and  $\mathbf{I}_2(\mathbf{B})$  are two invariants of the left Cauchy-Green strain tensor  $\mathbf{B}$ ,

$$\mathbf{I}_1(\mathbf{B}) = \text{tr} \mathbf{B}, \quad \mathbf{I}_2(\mathbf{B}) = \frac{1}{2} \left[ (\text{tr} \mathbf{B})^2 - \text{tr}(\mathbf{B}^2) \right], \quad (\text{B.4})$$

or equivalently,

$$W(\mathbf{B}) = \frac{\mu_1}{2} (\lambda_1^2 + \lambda_2^2 + \lambda_3^2) - \frac{\mu_2}{2} \left( \frac{1}{\lambda_1^2} + \frac{1}{\lambda_2^2} + \frac{1}{\lambda_3^2} \right). \quad (\text{B.5})$$

Using the strain energy density function (B.3) in the constitutive relation (B.1), we obtain

$$\mathbf{T} = q\mathbf{I} + \mu_1\mathbf{B} + \mu_2\mathbf{B}^{-1}, \quad (\text{B.6})$$

or equivalently,

$$T_i = q + \mu_1\lambda_i^2 + \frac{\mu_2}{\lambda_i^2}, \quad i = 1, 2, 3; \text{ no sum on index } i, \quad (\text{B.7})$$

where  $q$  is related to the mean stress  $\hat{p}$  (B.2) through

$$q = \hat{p} - \mu_1 I_1(\mathbf{B}) - \mu_2 I_2(\mathbf{B}). \quad (\text{B.8})$$

Note that for plane strain deformation, employing arbitrariness of  $\hat{p}$ , there is no difference between Mooney–Rivlin and Neo–Hookean constitutive modelling.

## B.2 The $J_2$ –deformation theory of plasticity

The  $J_2$ –deformation theory of plasticity has been introduced by Hutchinson and Neale (1979) (see also Hutchinson and Tvergaard, 1980; Neale, 1981) and is the most important constitutive model for the plastic response of ductile metals subject to monotonically increasing loading.

Introducing the logarithmic strains  $\epsilon_i = \ln \lambda_i$ , so that the incompressibility condition becomes

$$\epsilon_1 + \epsilon_2 + \epsilon_3 = 0, \quad (\text{B.9})$$

the constitutive law for the  $J_2$ –deformation theory of plasticity can be expressed as

$$T_i = \frac{2}{3}E_s\epsilon_i + \hat{p}, \quad i = 1, 2, 3; \text{ no sum on index } i, \quad (\text{B.10})$$

where  $E_s$  is the secant modulus to the curve representing the effective stress  $\sigma_e$  versus effective strain  $\epsilon_e$

$$\sigma_e = \sqrt{\frac{3}{2}} \sqrt{(\text{devT})_1^2 + (\text{devT})_2^2 + (\text{devT})_3^2}, \quad \epsilon_e = \sqrt{\frac{2}{3}} \sqrt{\epsilon_1^2 + \epsilon_2^2 + \epsilon_3^2}, \quad (\text{B.11})$$

where  $\text{dev T}_i$  are the principal components of deviatoric Cauchy stress  $\mathbf{T}$ ,

$$\text{devT} = \mathbf{T} - \hat{p}\mathbf{I}. \quad (\text{B.12})$$

The curve is assumed to be determined by

$$E_s = K \epsilon_e^{N-1}, \quad (\text{B.13})$$

where  $N \in ]0, 1]$  is a strain hardening exponent,  $K$  is a positive constitutive parameter, with the dimension of stress. The strain energy density results therefore to be given by the power-law function

$$W = \frac{K}{N+1} \epsilon_e^{N+1}. \quad (\text{B.14})$$

Under the plane strain condition ( $\epsilon_3 = 0$ ) eqn. (B.1) yields

$$T_1 - T_2 = \frac{\partial W}{\partial \epsilon_e} \left( \lambda_1 \frac{\partial \epsilon_e}{\partial \epsilon_1} \frac{\partial \epsilon_1}{\partial \lambda_1} - \lambda_2 \frac{\partial \epsilon_e}{\partial \epsilon_2} \frac{\partial \epsilon_2}{\partial \lambda_2} \right), \quad (\text{B.15})$$

where  $\lambda_1 = 1/\lambda_2 = \lambda$  and the effective stress (B.11)<sub>1</sub> and strain (B.11)<sub>2</sub> reduce to

$$\sigma_e = \frac{\sqrt{3}}{2} (T_1 - T_2), \quad \epsilon_e = \frac{2}{\sqrt{3}} |\epsilon_1|, \quad (\text{B.16})$$

and the secant modulus (B.13) becomes (see Fig. B.1)

$$E_s = \left( \frac{2}{\sqrt{3}} \right)^{N-1} |\epsilon_1|^{N-1}. \quad (\text{B.17})$$

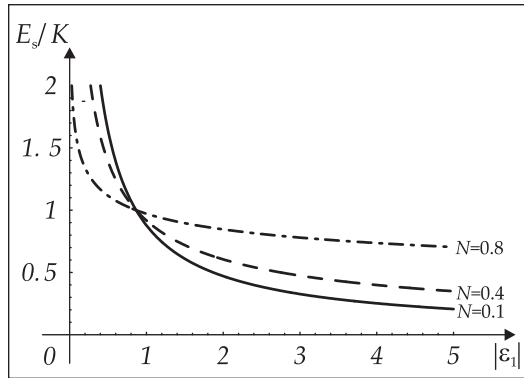


Figure B.1: Secant modulus  $E_s$  (B.17) normalized through division by  $K$  as function of principal strain  $\epsilon_1 = \ln \lambda_1$  for different values of hardening parameter  $N$ .

Finally, we arrive at

$$T_1 - T_2 = K \left( \frac{2}{\sqrt{3}} \right)^{N+1} |\epsilon_1|^{N-1} \epsilon_1, \quad (\text{B.18})$$

from which the behaviour in uniaxial plane strain tension/compression is determined taking  $T_2 = 0$  (see appendix C.1, eqn. (C.14)).

## Appendix C

---

### Simple boundary value problems in finite elasticity

For plane strain isochoric deformation (with out-of-plane direction singled out by the unit vector  $\mathbf{v}_3$ ) the left Cauchy-Green strain tensor  $\mathbf{B}$  takes the form

$$\mathbf{B} = \lambda^2 \mathbf{v}_1 \otimes \mathbf{v}_1 + \frac{1}{\lambda^2} \mathbf{v}_2 \otimes \mathbf{v}_2 + \mathbf{v}_3 \otimes \mathbf{v}_3, \quad (\text{C.1})$$

so that the deformation is defined through the principal stretch  $\lambda$  and the direction of the principal system  $\mathbf{v}_1$ – $\mathbf{v}_2$ . In the following we analyze the case of uniaxial extension, where the principal system has constant direction, and of simple shear, where the principal system changes direction during the deformation process.

#### C.1 Uniaxial plane strain tension and compression of an incompressible elastic block

With reference to Fig. C.1, we consider a plane strain problem of an incompressible elastic block subject to uniaxial tensile or compressive stress in the direction  $\mathbf{e}_1$ .

##### Kinematics

We begin with the kinematics, which is an elongation parallel to  $\mathbf{e}_1$  axis, so that the deformation is given by

$$\mathbf{x} - \mathbf{o} = \left( \frac{h}{h_0} \mathbf{e}_1 \otimes \mathbf{e}_1 + \frac{h_0}{h} \mathbf{e}_2 \otimes \mathbf{e}_2 + \mathbf{e}_3 \otimes \mathbf{e}_3 \right) (\mathbf{x}_0 - \mathbf{o}), \quad (\text{C.2})$$

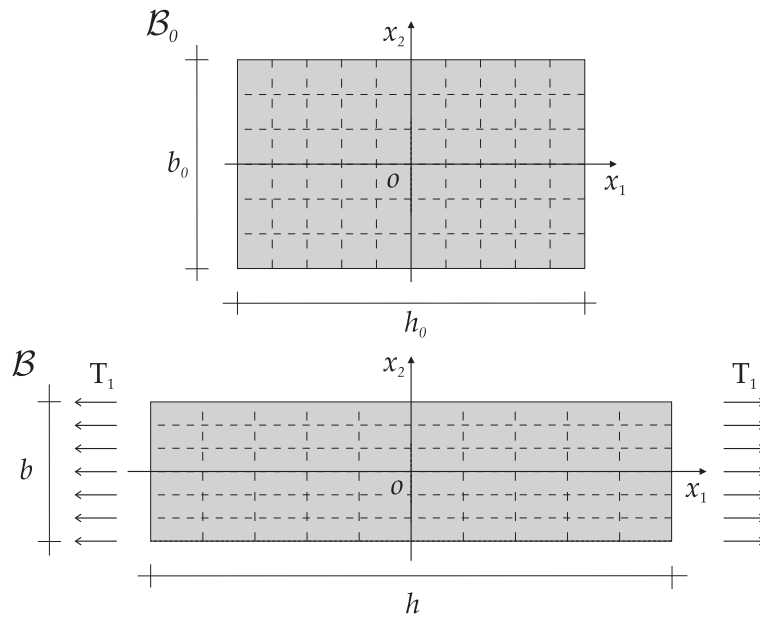


Figure C.1: Uniaxial, plane strain elongation in the  $x_1$  direction of an incompressible elastic material.

where the incompressibility constraint,

$$\frac{b}{b_0} = \frac{h_0}{h}, \quad (\text{C.3})$$

has been used. The deformation gradient ( $\mathbf{F}$ ), the left ( $\mathbf{U}$ ) and right ( $\mathbf{V}$ ) stretch tensors and the rotation tensor ( $\mathbf{R}$ ) result

$$\mathbf{F} = \mathbf{U} = \mathbf{V} = \frac{h}{h_0} \mathbf{e}_1 \otimes \mathbf{e}_1 + \frac{h_0}{h} \mathbf{e}_2 \otimes \mathbf{e}_2 + \mathbf{e}_3 \otimes \mathbf{e}_3, \quad \mathbf{R} = \mathbf{I}, \quad (\text{C.4})$$

so that the left ( $\mathbf{B}$ ) and right ( $\mathbf{C}$ ) Cauchy–Green strain tensor are

$$\mathbf{B} = \mathbf{C} = \frac{h^2}{h_0^2} \mathbf{e}_1 \otimes \mathbf{e}_1 + \frac{h_0^2}{h^2} \mathbf{e}_2 \otimes \mathbf{e}_2 + \mathbf{e}_3 \otimes \mathbf{e}_3, \quad (\text{C.5})$$

showing that there is no difference between Lagrangian and Eulerian axes (coincident to  $\mathbf{e}_1$  and  $\mathbf{e}_2$ ). We can note that uniaxial extension in the  $x_1$  direction is equivalent to a pure shear in a reference system rotated of  $45^\circ$  with respect to the  $x_1$ – $x_2$  reference system, as sketched in Fig. C.2.

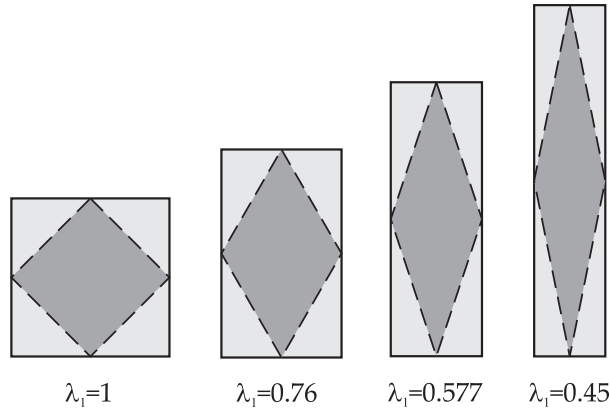


Figure C.2: Equivalence of uniaxial elongation in the  $x_1$  direction and pure shear in a reference system rotated of  $45^\circ$  with respect to the  $x_1$ - $x_2$  reference system.

It may be interesting to note that during elongation of the block a circle in the reference configuration transforms into an ellipse, with axes aligned parallel and orthogonal to the principal axes of  $\mathbf{B}$  and  $\mathbf{C}$ , Fig. C.3, where  $\lambda_1 = h/h_0$ .

Let us consider a fiber inclined at an angle  $\vartheta_0$  with respect to the  $x_1$ -axis in the reference configuration. It has been shown by Weissenberg (1935; 1948) that every fiber inclined at  $\vartheta_0$  and with the exceptions of  $\vartheta_0 = 0, \pi/4$  and  $\pi/2$ , may be transformed by imposing an appropriate deformation into a fiber with identical length (but different orientation, say,  $\vartheta$ ). In fact, the stretch of a fiber initially inclined at  $\vartheta_0$  with respect to the  $x_1$ -axis results

$$\lambda(\vartheta_0) = \left| \mathbf{F} \begin{bmatrix} \cos \vartheta_0 \\ \sin \vartheta_0 \end{bmatrix} \right| = \frac{|\cos \vartheta_0|}{\lambda_1} \sqrt{\lambda_1^4 + \tan^2 \vartheta_0}, \quad (\text{C.6})$$

which is plotted in Fig. C.4. We may observe from Figs. C.3 and C.4 that a fiber inclined at  $\pi/6$  suffers a contraction followed by an elongation, so that for  $h/h_0 = 0.577$  the original length of the fiber is recovered. Obviously, there are no fibers that can be always held at the original length during a continuous, finite elongation. Note that for  $\vartheta_0 = \pi/4$  the tangent of the graph is horizontal, so that there is no elongation for a deformation increment. Moreover, the minima of the curves reported in C.4 correspond to

$$\lambda_1^{min} = \sqrt{\tan \vartheta_0}, \quad \lambda^{min} = \sqrt{\sin 2\vartheta_0}. \quad (\text{C.7})$$

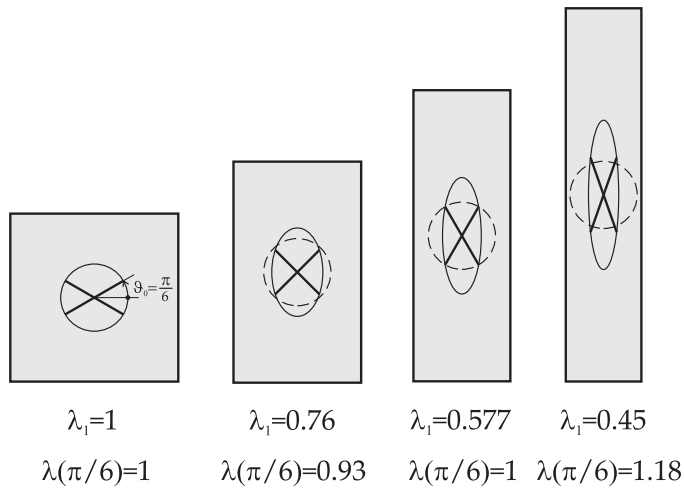


Figure C.3: Uniaxial, plane strain elongation in the  $x_2$  direction of an incompressible elastic material, where  $\lambda_1 = h/h_0$ : zero elongation line and strain ellipse. Note that the initial circle has been reported dashed in the deformed configurations for comparison. The fibers indicated are inclined at  $\pm\pi/6$ .

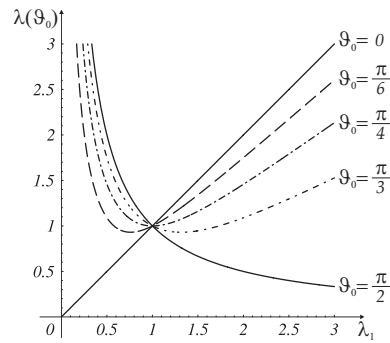


Figure C.4: Uniaxial, plane strain elongation in the  $x_2$  direction of an incompressible elastic material: stretch of fibers inclined at  $\vartheta_0$  with respect to the horizontal axis in the reference configuration, as function of principal stretch  $\lambda_1 = h/h_0$ .

## Stress

For an incompressible, Mooney-Rivlin material, the principal Cauchy stress

components can be evaluated from eqns. (C.5) and (B.7) in the form

$$T_1 = q + \mu_1 \frac{h^2}{h_0^2} + \mu_2 \frac{h_0^2}{h^2}, \quad T_2 = q + \mu_1 \frac{h_0^2}{h^2} + \mu_2 \frac{h^2}{h_0^2}, \quad T_3 = q + \mu_1 + \mu_2. \quad (\text{C.8})$$

Imposing that the stress is uniaxial,

$$T_2 = 0, \quad (\text{C.9})$$

allows determination of  $q$ , so that the plane strain uniaxial stress state becomes

$$T_1 = (\mu_1 - \mu_2) \left( \frac{h^2}{h_0^2} - \frac{h_0^2}{h^2} \right), \quad T_3 = \mu_1 \left( 1 - \frac{h_0^2}{h^2} \right) + \mu_2 \left( 1 - \frac{h^2}{h_0^2} \right), \quad (\text{C.10})$$

or equivalently in terms of logarithmic stretch  $\epsilon = \text{Log}(h/h_0)$ ,

$$T_1 = 2(\mu_1 - \mu_2) \sinh 2\epsilon, \quad T_3 = \mu_1(1 - e^{-2\epsilon}) + \mu_2(1 - e^{2\epsilon}). \quad (\text{C.11})$$

Introducing the shear modulus  $\mu_0$  defined as

$$\mu_0 = \mu_1 - \mu_2, \quad (\text{C.12})$$

the stress state (C.11) corresponds for small  $\epsilon$  to

$$T_1 \sim 4\mu_0\epsilon, \quad T_3 \sim 2\mu_0\epsilon, \quad (\text{C.13})$$

which compared to the plane strain equations of incompressible plane elasticity, shows that  $\mu_0$  represents the initial shear modulus.

It may be interesting to compare (C.11) with the corresponding response to an uniaxial elongation for a  $J_2$ -deformation theory material, eqn. (B.18),

$$T_1 = K \left( \frac{2}{\sqrt{3}} \right)^{N+1} |\epsilon|^{N-1} \epsilon, \quad T_2 = 0, \quad T_3 = \frac{T_1}{2}. \quad (\text{C.14})$$

This comparison is reported in Fig. C.5, where we can observe that:

- i) the behaviours are identical in tension and compression;
- ii) the Mooney–Rivlin material has a locking behaviour, so that stiffness increases at increasing strain, a behaviour expected for rubbers and biological materials;
- iii) the  $J_2$ -deformation theory material is tailored to mimick the behaviour of a metal, with a very stiff initial behaviour, followed by a hardening remaining always positive.

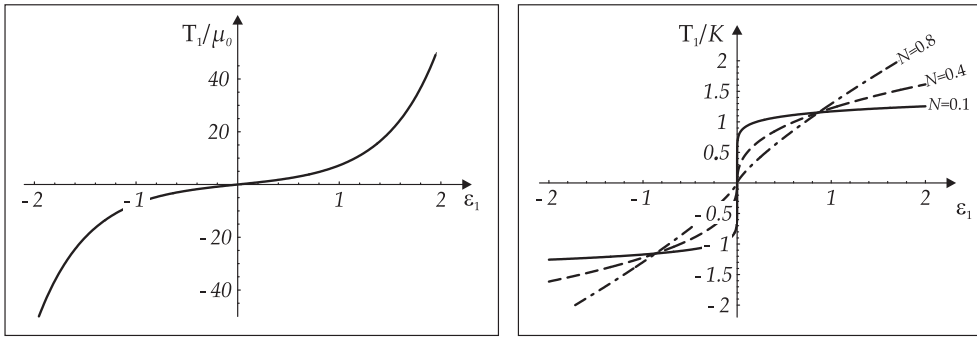


Figure C.5: Uniaxial, plane strain tension and compression of a Mooney-Rivlin (left) and of a  $J_2$ -deformation theory incompressible elastic material (right, for values of the hardening exponent  $N = \{0.1, 0.4, 0.8\}$ ).  $T_1$  is the axial Cauchy stress (normalized through division by  $\mu_0$  (left) and  $K$  (right)) and  $\epsilon_1$  is the logarithmic strain.

## C.2 Simple shear of an elastic block

### Kinematics

With reference to Fig. C.6, a block of a material is subject to a simple shear deformation (Truesdell and Toupin, 1960, §45) when two displacement components are null (along axes  $\hat{x}_2$  and  $\hat{x}_3$ , see the figure) and the other component,  $\hat{u}_1$ , depends linearly only on  $\hat{x}_2^0$ , namely

$$\hat{u}_1(\hat{x}_2^0) = \gamma \hat{x}_2^0, \quad \hat{u}_2 = \hat{u}_3 = 0, \quad (\text{C.15})$$

so that, if a point at  $\hat{x}_2^0 = h$  horizontally displaces of  $s$ , we can determine the dimensionless parameter  $\gamma = s/h$ , controlling the amplitude of shear deformation.

The deformation is defined by

$$\hat{\boldsymbol{x}} = \hat{\boldsymbol{x}}_0 + \gamma(\hat{\boldsymbol{x}}_0 \cdot \hat{\boldsymbol{e}}_2)\hat{\boldsymbol{e}}_1, \quad (\text{C.16})$$

so that the deformation gradient is

$$\boldsymbol{F} = \mathbf{I} + \gamma \hat{\boldsymbol{e}}_1 \otimes \hat{\boldsymbol{e}}_2, \quad (\text{C.17})$$

and the left and right Cauchy-Green deformation tensors are

$$\begin{aligned} \boldsymbol{B} &= \mathbf{I} + \gamma(\hat{\boldsymbol{e}}_1 \otimes \hat{\boldsymbol{e}}_2 + \hat{\boldsymbol{e}}_2 \otimes \hat{\boldsymbol{e}}_1) + \gamma^2 \hat{\boldsymbol{e}}_1 \otimes \hat{\boldsymbol{e}}_1, \\ \boldsymbol{C} &= \mathbf{I} + \gamma(\hat{\boldsymbol{e}}_1 \otimes \hat{\boldsymbol{e}}_2 + \hat{\boldsymbol{e}}_2 \otimes \hat{\boldsymbol{e}}_1) + \gamma^2 \hat{\boldsymbol{e}}_2 \otimes \hat{\boldsymbol{e}}_2. \end{aligned} \quad (\text{C.18})$$

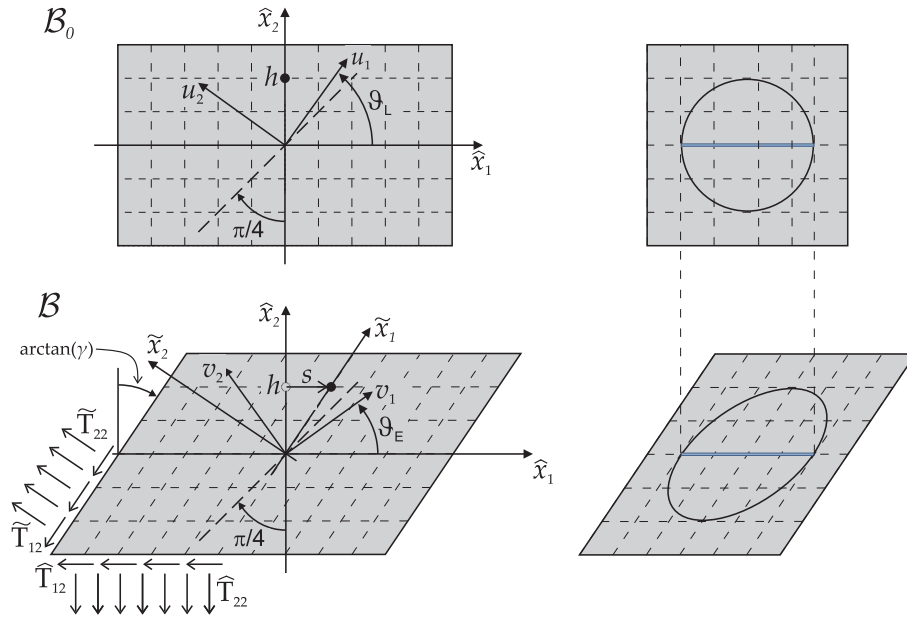


Figure C.6: Simple shear deformation. Upper part: reference configuration; lower part: configuration at a shear  $\gamma = s/h$ , with indicated Eulerian and Lagrangian principal axes, inclined at  $\vartheta_E$  and  $\vartheta_L$ , respectively. Note the circle in the reference configuration (upper part, right) that becomes a strain ellipse (lower part, right). In this sketch  $\arctan \gamma = 34^\circ$ , so that  $\vartheta_E \simeq 35.682^\circ$  and  $\vartheta_L \simeq 54.318^\circ$ .

Note that  $\det \mathbf{F} = 1$ , so that the simple shear deformation is isochoric.

The eigenvectors of  $\mathbf{B}$  and of  $\mathbf{C}$  define the principal Eulerian and Lagrangian axes, so that in the  $\hat{x}_1 - \hat{x}_2$  plane these are

$$\begin{aligned} \mathbf{v}_j &= \frac{1}{\sqrt{4 + \left[ \gamma - (-1)^j \sqrt{4 + \gamma^2} \right]^2}} \begin{bmatrix} \gamma - (-1)^j \sqrt{4 + \gamma^2} \\ 2 \end{bmatrix}, \\ \mathbf{u}_j &= \frac{1}{\sqrt{4 + \left[ \gamma + (-1)^j \sqrt{4 + \gamma^2} \right]^2}} \begin{bmatrix} -\gamma - (-1)^j \sqrt{4 + \gamma^2} \\ 2 \end{bmatrix}, \end{aligned} \quad (\text{C.19})$$

(where  $j = 1, 2$ ), respectively, while the principal stretches result to be given

by

$$\lambda_j = -(-1)^j \frac{\gamma}{2} + \sqrt{1 + \left(\frac{\gamma}{2}\right)^2}. \quad (\text{C.20})$$

Note that

$$\lambda_1 - \lambda_2 = \gamma, \quad (\text{C.21})$$

so that if  $\gamma > 0$  ( $< 0$ ) then  $\lambda_1 > \lambda_2$  ( $\lambda_1 < \lambda_2$ ).

The eigenvectors (C.19) yield (with an elementary use of trigonometry) the inclination of the Eulerian,  $\vartheta_E$ , and Lagrangian,  $\vartheta_L$ , axes with respect to the  $\hat{x}_1$ -axis

$$\vartheta_E = \frac{1}{2} \arctan\left(\frac{2}{\gamma}\right), \quad \vartheta_L = \frac{\pi}{2} - \vartheta_E, \quad (\text{C.22})$$

plotted in Fig. C.7 as functions of the amount of shear  $\gamma$ .

For  $\gamma > 0$ , note that  $0 \leq \vartheta_E \leq \pi/4$  and  $\pi/4 \leq \vartheta_L \leq \pi/2$ , so that in the reference configuration, at null strain,  $\vartheta_E = \vartheta_L = \pi/4$  and the Lagrangian and Eulerian axes coincide, while at infinite strain  $\vartheta_E = 0$  and  $\vartheta_L = \pi/2$ .

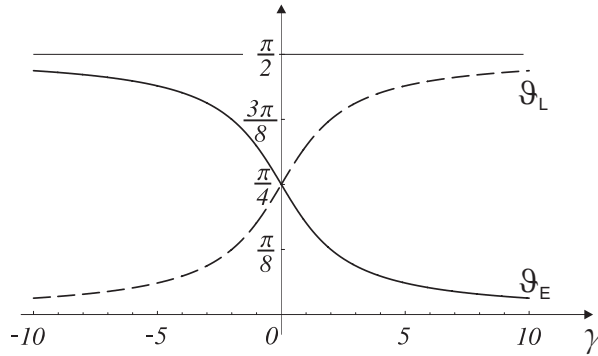


Figure C.7: Angles of inclination of Eulerian,  $\vartheta_E$ , and Lagrangian,  $\vartheta_L$ , principal axes during simple shear deformation, as functions of the amount of shear  $\gamma$ .

With reference to the Cauchy-Green deformation tensors (C.18), we note that a fiber parallel to the  $\hat{x}_1$ -axis, singled out by the unit vector  $\hat{e}_1$  remains unstretched, since

$$\hat{e}_1 \cdot \mathbf{C} \hat{e}_1 = \hat{e}_1 \cdot \mathbf{B}^{-1} \hat{e}_1 = 1, \quad (\text{C.23})$$

so that the fibers parallel to the  $\hat{x}_1$ -axis in Fig. C.6 are so-called ‘zero elongation lines’ (Weissenberg, 1948).

The left and right stretch tensors are

$$\begin{aligned}\mathbf{V} &= \frac{1}{\sqrt{4+\gamma^2}} [2 \hat{\mathbf{e}}_1 \otimes \hat{\mathbf{e}}_1 + \gamma (\hat{\mathbf{e}}_1 \otimes \hat{\mathbf{e}}_2 + \hat{\mathbf{e}}_2 \otimes \hat{\mathbf{e}}_1) + (2 + \gamma^2) \hat{\mathbf{e}}_2 \otimes \hat{\mathbf{e}}_2], \\ \mathbf{U} &= \frac{1}{\sqrt{4+\gamma^2}} [(2 + \gamma^2) \hat{\mathbf{e}}_1 \otimes \hat{\mathbf{e}}_1 + \gamma (\hat{\mathbf{e}}_1 \otimes \hat{\mathbf{e}}_2 + \hat{\mathbf{e}}_2 \otimes \hat{\mathbf{e}}_1) + 2 \hat{\mathbf{e}}_2 \otimes \hat{\mathbf{e}}_2],\end{aligned}\tag{C.24}$$

and the rotation tensor is

$$\mathbf{R} = \frac{1}{\sqrt{4+\gamma^2}} [2(\hat{\mathbf{e}}_1 \otimes \hat{\mathbf{e}}_1 + \hat{\mathbf{e}}_2 \otimes \hat{\mathbf{e}}_2) + \gamma(\hat{\mathbf{e}}_1 \otimes \hat{\mathbf{e}}_2 - \hat{\mathbf{e}}_2 \otimes \hat{\mathbf{e}}_1)],\tag{C.25}$$

so that there is an in-plane rigid-body rotation of an angle (taken positive when anti-clockwise)  $\arctan(-\gamma/2)$ .

### Stress

For a material isotropic in the reference configuration, the Cauchy stress is coaxial to the left Cauchy-Green tensor  $\mathbf{V}$  (C.24)<sub>1</sub>, so that in the Eulerian principal reference system we have the spectral representation

$$\mathbf{T} = T_1 \mathbf{v}_1 \otimes \mathbf{v}_1 + T_2 \mathbf{v}_2 \otimes \mathbf{v}_2 + T_3 \mathbf{e}_3 \otimes \mathbf{e}_3,\tag{C.26}$$

where, in the  $\hat{x}_1$ - $\hat{x}_2$  reference system, the unit vectors  $\mathbf{v}_1$  and  $\mathbf{v}_2$  are defined by the components

$$\mathbf{v}_1 = \begin{bmatrix} \cos \vartheta_E \\ \sin \vartheta_E \end{bmatrix}, \quad \mathbf{v}_2 = \begin{bmatrix} -\sin \vartheta_E \\ \cos \vartheta_E \end{bmatrix}.\tag{C.27}$$

Therefore, in the reference system  $\hat{\mathbf{e}}_1, \hat{\mathbf{e}}_2$ , we have

$$\begin{aligned}\hat{\mathbf{T}}_{11} &= T_1 \cos^2 \vartheta_E + T_2 \sin^2 \vartheta_E, \\ \hat{\mathbf{T}}_{22} &= T_1 \sin^2 \vartheta_E + T_2 \cos^2 \vartheta_E, \\ \hat{\mathbf{T}}_{12} &= (T_1 - T_2) \cos \vartheta_E \sin \vartheta_E = \frac{T_1 - T_2}{2} \sin 2\vartheta_E,\end{aligned}\tag{C.28}$$

which, using simple trigonometric identities, yield

$$\left. \begin{array}{l} \hat{\mathbf{T}}_{11} \\ \hat{\mathbf{T}}_{22} \end{array} \right\} = p \pm \frac{T_1 - T_2}{2} \frac{\gamma}{\sqrt{4 + \gamma^2}}, \quad \hat{\mathbf{T}}_{12} = \frac{T_1 - T_2}{\sqrt{4 + \gamma^2}},\tag{C.29}$$

where  $p$  is the in-plane mean stress,

$$p = \frac{T_1 + T_2}{2}. \quad (\text{C.30})$$

From eqns. (C.28) we obtain

$$\widehat{T}_{11} - \widehat{T}_{22} = \frac{2}{\tan 2\vartheta_E} \widehat{T}_{12} = \gamma \widehat{T}_{12}, \quad (\text{C.31})$$

which is independent of the specific constitutive equation and is therefore an example of a so-called ‘universal relation’. Note that for  $\gamma < 1$  ( $\gamma > 1$ ),  $\widehat{T}_{11} - \widehat{T}_{22} < \widehat{T}_{12}$  ( $\widehat{T}_{11} - \widehat{T}_{22} > \widehat{T}_{12}$ ) and, in particular, the deviatoric stress  $\widehat{T}_{11} - \widehat{T}_{22}$  is of higher order in  $\gamma$  than  $\widehat{T}_{12}$ .

The stress on the inclined faces of the deformed block (sketched in the lower part of Fig. C.7) can be obtained from the components of the unit tangential and normal vector

$$\tilde{\mathbf{e}}_1 = \begin{bmatrix} \frac{\gamma}{\sqrt{1+\gamma^2}} \\ 1 \\ \frac{1}{\sqrt{1+\gamma^2}} \end{bmatrix}, \quad \tilde{\mathbf{e}}_2 = \begin{bmatrix} -\frac{1}{\sqrt{1+\gamma^2}} \\ \gamma \\ \frac{\gamma}{\sqrt{1+\gamma^2}} \end{bmatrix}, \quad (\text{C.32})$$

in the form

$$\left. \begin{array}{l} \tilde{T}_{11} \\ \tilde{T}_{22} \end{array} \right\} = p \pm \frac{T_1 - T_2}{2} \frac{\gamma(3+\gamma^2)}{(1+\gamma^2)\sqrt{4+\gamma^2}}, \quad \tilde{T}_{12} = \frac{T_1 - T_2}{(1+\gamma^2)\sqrt{4+\gamma^2}}. \quad (\text{C.33})$$

Assuming a Mooney-Rivlin response (§B.1) we obtain

$$\left. \begin{array}{l} \widehat{T}_{11} \\ \widehat{T}_{22} \end{array} \right\} = p \pm \frac{\mu_0 \gamma^2}{2}, \quad \widehat{T}_{12} = \mu_0 \gamma, \quad (\text{C.34})$$

in which  $p$  remains undetermined.

In the case of a  $J_2$ -deformation theory material (§B.2) we obtain

$$\left. \begin{array}{l} \widehat{T}_{11} \\ \widehat{T}_{22} \end{array} \right\} = p \pm \frac{\mu \gamma}{\sqrt{4+\gamma^2} \coth 2\epsilon}, \quad \widehat{T}_{12} = \frac{4\mu_* \epsilon}{N\sqrt{4+\gamma^2}}, \quad (\text{C.35})$$

where  $\epsilon = \epsilon_1 = \ln \lambda_1$  is the logarithmic stretch, function of  $\gamma$  through eqn. (C.20),  $N \in ]0, 1]$  is the strain hardening exponent,  $\mu$  and  $\mu_*$  are incremental shear moduli and depend on the current stretch in the following way<sup>1</sup>

$$\mu = \bar{\mu} 2\epsilon |\epsilon|^{N-1} \coth 2\epsilon, \quad \mu_* = N\bar{\mu} |\epsilon|^{N-1}, \quad (\text{C.36})$$

where

$$\bar{\mu} = \frac{K}{3} \left( \frac{2}{\sqrt{3}} \right)^{N-1}, \quad (\text{C.37})$$

in which  $K$  is a positive stiffness parameter.

Considering small shear amplitude  $\gamma$ , the constitutive relations (C.35) become

$$\left. \begin{array}{l} \hat{T}_{11} \\ \hat{T}_{22} \end{array} \right\} = p \pm \frac{\bar{\mu}}{2N} |\gamma|^{N+1}, \quad \hat{T}_{12} = \text{sign}(\gamma) \frac{\bar{\mu}}{2^{N-1}} |\gamma|^N. \quad (\text{C.38})$$

The deviatoric stress and the shear stress, made dimensionless through division by  $\mu_0$  for a Mooney-Rivlin material and for  $K$  for a  $J_2$ -deformation theory material, are reported in Figs. C.8 and C.9, respectively.

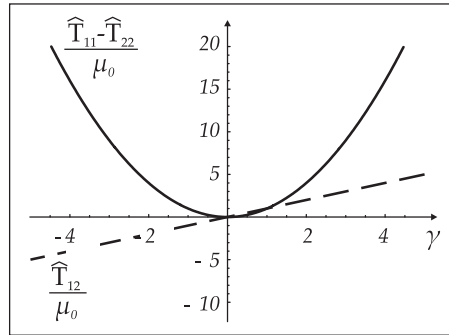


Figure C.8: Simple shear of an elastic (incompressible), Mooney-Rivlin material: stress response at finite shear amplitude  $\gamma$ .

Note that it is evident from eqn. (C.38) that for  $\gamma = 0$  the curve representing the deviatoric stress has an horizontal tangent and the curve representing

<sup>1</sup>Note that the  $J_2$ -deformation theory material is a nonlinear elastic material isotropic in the unloaded state. Due to the fact that the incremental shear moduli  $\mu$  and  $\mu_*$  tend to infinity when  $\epsilon$  tends to zero (and  $N < 1$ ), the ratio  $\mu_*/\mu$  tends to  $N$  (and therefore is different from 1).

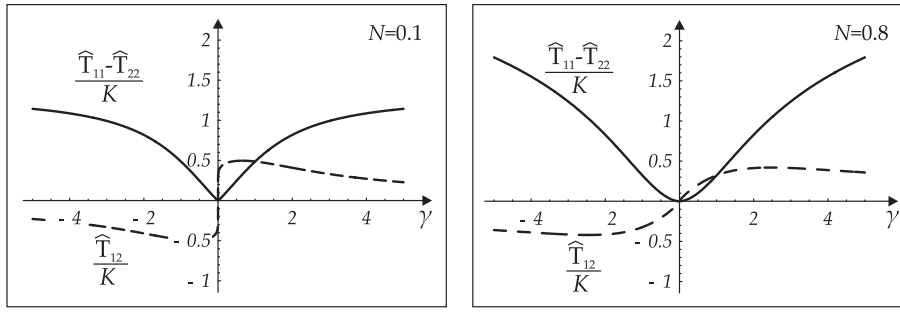


Figure C.9: Simple shear of an elastic (incompressible),  $J_2$ -deformation theory material: stress response at finite shear amplitude  $\gamma$  at low  $N = 0.1$  and high  $N = 0.8$  strain hardening.

the shear stress has a vertical tangent. Although the vertical tangent is not visible in Fig. C.9 (right), it is easy to check its existence; in fact, the incremental equations corresponding to eqn. (C.35) become

$$\dot{T}_{11} = \dot{T}_{22} = \dot{p}, \quad \dot{T}_{12} = \mu_* \dot{\gamma}, \quad (\text{C.39})$$

where  $\dot{\gamma}$  ( $\dot{p}$ ) represents the shear (mean stress) increment, respectively and  $\mu_*$  tends to infinity when  $\gamma$  tends to zero. Moreover, the curve relative to  $N = 0.1$  coincides with that plotted by Harren et al. (1989, their Fig. 2).

The following features may be observed from the obtained equations, holding for both Mooney-Rivlin and  $J_2$ -deformation theory materials.

- i)  $\mu$  represents a shear modulus;
- ii) Normal stress is generated through a shear deformation, this is the so-called ‘Kelvin effect’;
- iii) The two normal stress components are not equal, i.e.  $\hat{T}_{11} \neq \hat{T}_{22}$ , a feature representing the so-called ‘Poynting effect’.
- iv) The linear theory can be recovered by neglecting terms on the order of

$\gamma^2$  or higher. Doing this, we obtain the following linear approximations

$$\begin{aligned}
 \lambda_j &\sim -(-1)^j \frac{\gamma}{2} + 1, \\
 \vartheta_E &\sim \frac{\pi - \gamma}{4}, \\
 \vartheta_L &\sim \frac{\pi + \gamma}{4}, \\
 \mathbf{v}_j &\sim \frac{1}{\sqrt{2}} \left\{ -(-1)^j + \frac{\gamma}{4}, \quad 1 + (-1)^j \frac{\gamma}{4} \right\}, \\
 \mathbf{u}_j &\sim \frac{1}{\sqrt{2}} \left\{ -(-1)^j - \frac{\gamma}{4}, \quad 1 - (-1)^j \frac{\gamma}{4} \right\},
 \end{aligned} \tag{C.40}$$

where  $j = 1, 2$ . For a Mooney-Rivlin material

$$\widehat{\mathbf{T}}_{11} \sim \widehat{\mathbf{T}}_{22} \sim \widetilde{\mathbf{T}}_{11} \sim \widetilde{\mathbf{T}}_{22} \sim p, \quad \widehat{\mathbf{T}}_{12} \sim \widetilde{\mathbf{T}}_{12} \sim \mu_0 \gamma, \tag{C.41}$$

while for a  $J_2$ -deformation theory material a linear theory cannot be obtained starting from an unloaded state, see eqns. (C.38).



## Appendix D

---

### Solution for a prescribed rigid-rotation of a stiffener in a prestressed medium

We consider the problem of a stiffener subject to a prescribed incremental rotation  $\omega_S$  and embedded in a homogeneously prestressed material. This problem may for instance find application to the interpretation of the so-called ‘vane test’ used in geotechnical engineering. Imposing the satisfaction of the kinematical boundary conditions along the stiffener line (4.79), where now  $\omega_S$  is prescribed, we represent the stream function as

$$\widehat{\psi}^\circ(\hat{x}_1, \hat{x}_2) = \frac{\omega_S}{2} \sum_{j=1}^2 \operatorname{Re} \left\{ E_j^{II} \left[ \hat{z}_j^2 - \hat{z}_j \sqrt{\hat{z}_j^2 - l^2} + l^2 \ln \left( \hat{z}_j + \sqrt{\hat{z}_j^2 - l^2} \right) \right] \right\}, \quad (\text{D.1})$$

which yields the following linear problem for the complex constants  $E_1^{II}$  and  $E_2^{II}$

$$\begin{bmatrix} \operatorname{Re}[W_1] & -\operatorname{Im}[W_1] & \operatorname{Re}[W_2] & -\operatorname{Im}[W_2] \\ \operatorname{Im}[W_1] & \operatorname{Re}[W_1] & \operatorname{Im}[W_2] & \operatorname{Re}[W_2] \\ 1 & 0 & 1 & 0 \\ 0 & 1 & 0 & 1 \end{bmatrix} \begin{bmatrix} \operatorname{Re}[E_1^{II}] \\ \operatorname{Im}[E_1^{II}] \\ \operatorname{Re}[E_2^{II}] \\ \operatorname{Im}[E_2^{II}] \end{bmatrix} = \begin{bmatrix} 0 \\ 0 \\ -1 \\ 0 \end{bmatrix}. \quad (\text{D.2})$$

The solution of the present problem does not depend on the in-plane stress parameter  $\eta$ , similarly to the solution (4.82), and satisfies

$$\begin{aligned} W_1^2 E_1^{II} + W_2^2 E_2^{II} &= W_1 W_2, \\ W_1^3 E_1^{II} + W_2^3 E_2^{II} &= W_1 W_2 (W_1 + W_2). \end{aligned} \quad (\text{D.3})$$

In the particular case of  $\vartheta_0 = 0$ , the solution becomes

$$\begin{aligned} \text{in EC} \quad & \begin{cases} E_1^{II} = -\frac{1}{2\alpha}(\alpha + i\beta), \\ E_2^{II} = -\frac{1}{2\alpha}(\alpha - i\beta), \end{cases} \Rightarrow \text{Im}[W_1^2 E_1^{II} + W_2^2 E_2^{II}] = 0, \\ \text{in EI} \quad & \begin{cases} E_1^{II} = \frac{\beta_2}{\beta_1 - \beta_2}, \\ E_2^{II} = -\frac{\beta_1}{\beta_1 - \beta_2}, \end{cases} \Rightarrow \text{Im}[W_1^2 E_1^{II} + W_2^2 E_2^{II}] = 0. \end{aligned} \quad (\text{D.4})$$

The incremental stress intensity factor, eqn. (4.23)<sub>2</sub>, results

$$\dot{K}_{(\epsilon)II} = -2\mu\omega_S\sqrt{\pi l}, \quad (\text{D.5})$$

and the asymptotic fields in the polar coordinate system  $(r, \vartheta)$  centered at the stiffener tip ( $\hat{x}_1 = l, \hat{x}_2 = 0$ ) are (constant terms have been neglected)

$$\begin{aligned} [[\hat{t}_{21}(\Delta l - r, \pi)]] &= -\omega_S \frac{\sqrt{2l}}{\sqrt{\Delta l - r}} \widehat{\mathbb{G}}_{2121} \text{Im}[W_1^2 E_1^{II} + W_2^2 E_2^{II}], \\ [[\hat{t}_{22}(\Delta l - r, \pi)]] &= -\omega_S \frac{\sqrt{2l}}{\sqrt{\Delta l - r}} \left\{ 2(\widehat{\mathbb{G}}_{2221} - \widehat{\mathbb{G}}_{2111}) \text{Im}[W_1^2 E_1^{II} + W_2^2 E_2^{II}] \right. \\ &\quad \left. - \widehat{\mathbb{G}}_{2121} \text{Im}[W_1^3 E_1^{II} + W_2^3 E_2^{II}] \right\}, \\ \hat{v}_1(r, 0) &= 0, \\ \hat{v}_2(r, 0) &= -\omega_S \sqrt{2lr}. \end{aligned} \quad (\text{D.6})$$

Using the identity (D.3), the incremental energy release rate for stiffener growth (4.108) can be calculated in the form

$$\dot{G}_{II} = -\frac{\dot{K}_{(\epsilon)II}^2}{8\mu^2} \left\{ 2(\widehat{\mathbb{G}}_{2221} - \widehat{\mathbb{G}}_{2111}) \text{Im}[W_1 W_2] - \widehat{\mathbb{G}}_{2121} \text{Im}[W_1 W_2 (W_1 + W_2)] \right\}, \quad (\text{D.7})$$

which has been numerically checked to result always negative in the elliptic regime. The incremental ‘global’ axial and shear forces can be computed and result null by equilibrium, while the incremental moment applied to the

inclusion (taken positive when anti-clockwise) is given by

$$\begin{aligned}\dot{\mathcal{M}} &= - \int_{-l}^l [[\hat{t}_{22}(y, 0)]] y dy \\ &= \pi l^2 \omega_S \left\{ 2(\hat{\mathbb{G}}_{2221} - \hat{\mathbb{G}}_{2111}) \text{Im}[W_1 W_2] - \hat{\mathbb{G}}_{2121} \text{Im}[W_1 W_2 (W_1 + W_2)] \right\},\end{aligned}\tag{D.8}$$

that corresponds, when prestress is absent, to the value  $2\mu\pi l^2\omega_S$  calculated by Muskhelishvili (1953, §83a). Note that the following interesting relation holds true in the elliptic regime:

$$\dot{G}_{II} = -\frac{\dot{\mathcal{M}}\omega_S}{2l},\tag{D.9}$$

from which, due to the negativity of  $\dot{G}_{II}$ , we note that  $\dot{\mathcal{M}}$  has always the same sign of  $\omega_S$ .

The incremental moment and level sets of incremental deviatoric strain are reported as functions of the simple shear amplitude  $\gamma$  in Figs. D.1 and D.2, for a  $J_2$ -deformation theory material at different values of strain hardening coefficient  $N$ . In particular, we note that the maximum incremental moment divided by  $\mu$  occurs at null prestress, while at the ellipticity loss the incremental moment vanishes and the shear bands near the direction orthogonal to the stiffener are privileged.

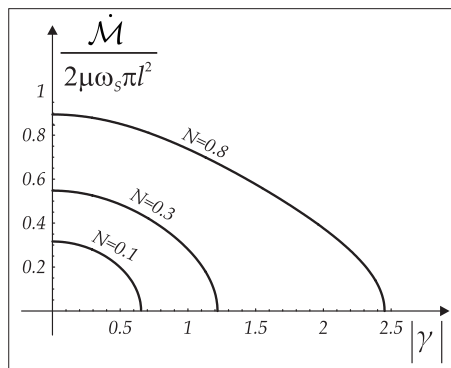


Figure D.1: Incremental moment  $\dot{\mathcal{M}}$  for an incremental rotation  $\omega_S$  of the stiffener as a function of the simple shear amplitude  $\gamma$ , for a  $J_2$ -deformation theory material at different values of strain hardening coefficient  $N$ .

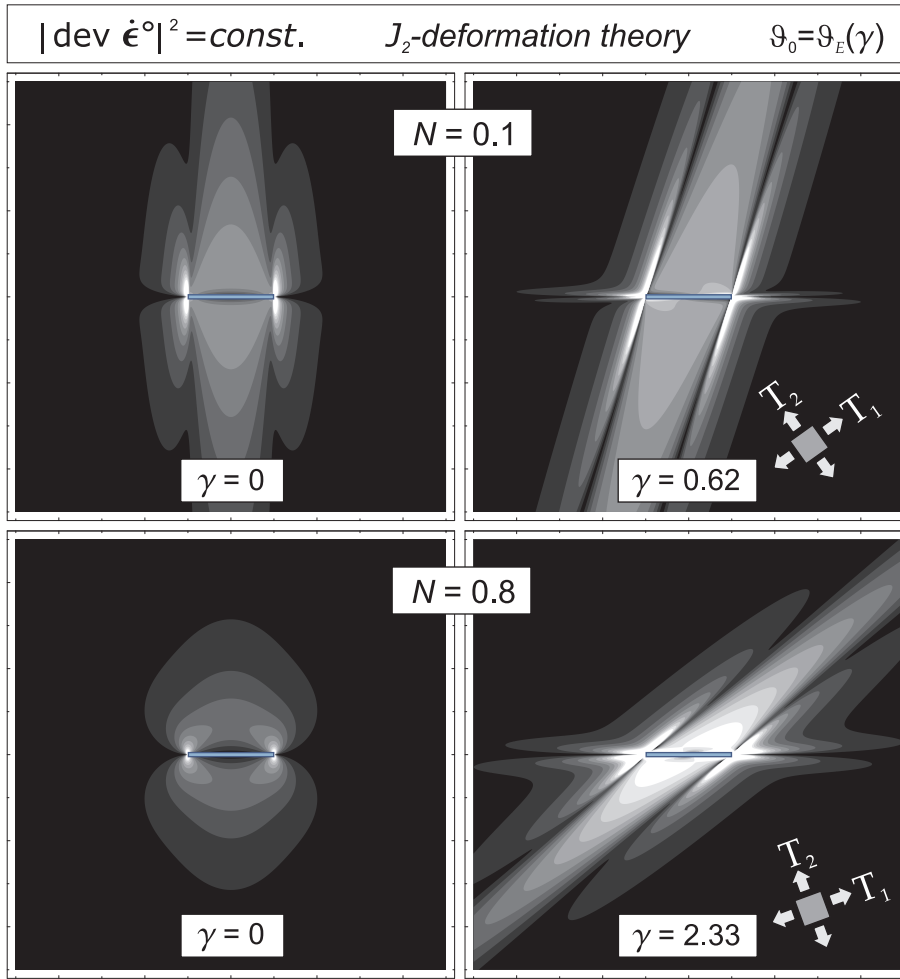


Figure D.2: Interaction of shear bands and mechanical fields near a stiffener of length  $2l$  (evidenced with a thin rectangle, providing the bar scale of the representation) embedded in a  $J_2$ -deformation theory material (with  $N = 0.1$  (upper part) and  $N = 0.8$  (lower part)) subject to a finite shear of amount  $\gamma$  and a subsequent imposed incremental rigid rotation  $\omega_S$ . Null shear before the perturbation is considered on the left, while a shear equal to 0.95 times the amount at ellipticity loss,  $\gamma^{EL}$ , is considered on the right. Note that the prestress (of principal components  $T_1$  and  $T_2$ ) generated through the simple shear deformation is inclined with respect to the stiffener line.

## Appendix E

---

### A stiffener embedded in a linear, compressible and isotropic elastic material

We report for completeness the small-strain asymptotic solution for a stiffener in a linear, elastic, isotropic medium. The Poisson's ratio  $\nu$  enters the solution through the parameter  $\kappa$  defined as

$$\kappa = \begin{cases} 3 - 4\nu, & \text{for plane strain,} \\ \frac{3 - \nu}{1 + \nu}, & \text{for plane stress.} \end{cases} \quad (\text{E.1})$$

For Mode I loading the angular functions result

$$\begin{aligned} \omega_r(\vartheta) &= -a \left[ (2\kappa + 1) \cos \frac{3\vartheta}{2} + (2\kappa - 1) \cos \frac{\vartheta}{2} \right], \\ \omega_\vartheta(\vartheta) &= a (2\kappa + 1) \left( \sin \frac{3\vartheta}{2} + \sin \frac{\vartheta}{2} \right), \\ \tau_{rr}(\vartheta) &= -a \left[ (2\kappa + 1) \cos \frac{3\vartheta}{2} + 5 \cos \frac{\vartheta}{2} \right], \\ \tau_{\vartheta\vartheta}(\vartheta) &= a \left[ (2\kappa + 1) \cos \frac{3\vartheta}{2} - 3 \cos \frac{\vartheta}{2} \right], \\ \tau_{r\vartheta}(\vartheta) = \tau_{\vartheta r}(\vartheta) &= a \left[ (2\kappa + 1) \sin \frac{3\vartheta}{2} - \sin \frac{\vartheta}{2} \right], \end{aligned} \quad (\text{E.2})$$

while for Mode II

$$\begin{aligned}
\omega_r(\vartheta) &= b(2\kappa - 1) \left( \sin \frac{3\vartheta}{2} + \sin \frac{\vartheta}{2} \right), \\
\omega_\vartheta(\vartheta) &= b \left[ (2\kappa - 1) \cos \frac{3\vartheta}{2} + (2\kappa + 1) \cos \frac{\vartheta}{2} \right], \\
\tau_{rr}(\vartheta) &= b \left[ (2\kappa - 1) \sin \frac{3\vartheta}{2} + 5 \sin \frac{\vartheta}{2} \right], \\
\tau_{\vartheta\vartheta}(\vartheta) &= -b \left[ (2\kappa - 1) \sin \frac{3\vartheta}{2} - 3 \sin \frac{\vartheta}{2} \right], \\
\tau_{r\vartheta}(\vartheta) = \tau_{\vartheta r}(\vartheta) &= b \left[ (2\kappa - 1) \cos \frac{3\vartheta}{2} - \cos \frac{\vartheta}{2} \right].
\end{aligned} \tag{E.3}$$

We note that in plane strain, for incompressible material ( $\nu = 0.5$ ), it is  $\tau_{\vartheta\vartheta}(0) = 0$  for Mode I and  $\tau_{r\vartheta}(0) = 0$  for Mode II.

Employing the definition (4.23), the energy release rate for stiffener growth can be obtained from the asymptotic formula expressing the near-tip fields in the form

$$G = -(1 + \kappa) \frac{K_{(\epsilon)I}^2 + K_{(\epsilon)II}^2}{8\mu}, \tag{E.4}$$

which, except for the negative sign (implying stiffener reduction), has the same expression for energy release rate in the crack growth problem.

In the incompressible limit and plane strain, the energy release rate (E.4) can be expressed as

$$G = -\frac{K_{(\epsilon)I}^2 + K_{(\epsilon)II}^2}{4\mu}, \tag{E.5}$$

which can alternatively be (directly) obtained setting  $k = 0$  and  $\xi = 1$  in eqn. (4.111).

# Nomenclature

---

- $\mathbf{x}$  : position vector
- $\mathbf{u}$  : displacement vector, unit vector of Lagrangian reference system
- $\mathbf{v}$  : incremental displacement vector, unit vector of Eulerian reference system
- $x_1$ – $x_2$  : reference system aligned parallel and orthogonal with respect to the principal strain and stress directions
- $\mathbf{F}$  : deformation gradient tensor [ $\mathbf{F} = \nabla \mathbf{x} = \mathbf{R}\mathbf{U} = \mathbf{V}\mathbf{R}$ ]
- $J$  : determinant of  $\mathbf{F}$ , path-independent  $J$ -integral
- $\mathbf{U}$  : left (symmetric and positive definite) stretch tensor
- $\mathbf{V}$  : right (symmetric and positive definite) stretch tensor
- $\mathbf{R}$  : rotation tensor
- $\mathbf{B}$  : left Cauchy-Green (symmetric and positive definite) strain tensor  
[ $\mathbf{B} = \mathbf{F}\mathbf{F}^T = \mathbf{V}^2$ ]
- $\mathbf{C}$  : right Cauchy-Green (symmetric and positive definite) strain tensor  
[ $\mathbf{C} = \mathbf{F}^T\mathbf{F} = \mathbf{U}^2$ ]
- $\mathbf{T}$  : Cauchy (symmetric) stress tensor
- $\mathbf{t}$  : nominal stress tensor [ $\mathbf{t} = J\mathbf{F}^{-1}\mathbf{T}$ ]
- $\lambda$  : stretch

- $\varepsilon$  : logarithmic strain [ $\varepsilon = \ln \lambda$ ]  
 $\varepsilon^{sur}$  : critical logarithmic strain for surface bifurcation  
 $\varepsilon^{EL}$  : critical logarithmic strain at the ellipticity loss  
 $\varepsilon^{PD}$  : critical logarithmic strain for the positive definiteness condition  
 $\vartheta_E$  : inclination of the principal Eulerian axes  
 $\vartheta_L$  : inclination of the principal Lagrangian axes  
 $\vartheta_0$  : inclusion inclination with respect to the  $x_1$ -axis  
 $\vartheta^{SB}$  : shear band inclination with respect to the  $x_1$ -axis  
 $\hat{\vartheta}^{SB}$  : shear band inclination with respect to the  $\hat{x}_1$ -axis  
 $\gamma$  : finite simple shear amount, exponent in the asymptotic analysis  
 $\gamma^{SB}$  : inclination of the shear band normal with respect to the  $x_1$ -axis  
 $\omega_S$  : rigid rotation of the stiffener  
 $\text{Re}[\cdot]$  : real part of the relevant argument  
 $\text{Im}[\cdot]$  : imaginary part of the relevant argument  
 $[[\cdot]]$  : jump in the relevant argument across a discontinuity

# Bibliography

---

- [1] Aifantis, E.C. (1987) The physics of plastic deformation. *Int. J. Plasticity* **3**, 211–247.
- [2] Aifantis, K.E. and Willis, J.R. (2005) The role of interfaces in enhancing the yield strength of composites and polycrystals. *J. Mech. Phys. Solids* **53**, 1047–1070.
- [3] Anand, L. and Spitzig, W.A. (1980) Initiation of localized shear bands in plane strain. *J. Mech. Phys. Solids* **28**, 113–128.
- [4] Anand, L. and Spitzig, W.A. (1982) Shear-band orientations in plane strain. *Acta Metall.* **30**, 553–561.
- [5] Atkinson, C. (1973) Some ribbon-like inclusion problems. *Int. J. Engng. Sci.* **11**, 243–266.
- [6] Ballarini, R. (1987) An integral-equation approach for rigid line inhomogeneity problems. *Int. J. Fracture* **33**, R23–R26.
- [7] Ballarini, R. (1990) A rigid line inclusion at a bimaterial interface. *Eng. Fracture Mechanics* **37**, 1–5.
- [8] Bei, H., Xie, S. and George, E.P. (2006) Softening caused by profuse shear banding in a bulk metallic glass. *Phys. Rev. Lett.* **96**, 105503.

- 
- [9] Benallal, A. and Bigoni, D. (2004) Effects of temperature and thermo-mechanical couplings on material instabilities and strain localization of inelastic materials. *J. Mech. Phys. Solids* **52**, 725–753.
- [10] Bigoni, D. and Hueckel, T. (1991) Uniqueness and localization-I. Associative and non-associative elastoplasticity. *Int. J. Solids Structures* **28**, 197–213.
- [11] Bigoni, D., Ortiz, M. and Needleman, A. (1997) Effect of interfacial compliance on bifurcation of a layer bonded to a substrate. *Int. J. Solids Structures* **34**, 4305–4326.
- [12] Bigoni, D. and Loret, B. (1999) Effects of elastic anisotropy on strain localization and flutter instability in plastic solids. *J. Mech. Phys. Solids* **47**, 1409–1436.
- [13] Bigoni, D. and Capuani, D. (2002) Green’s function for incremental nonlinear elasticity: shear bands and boundary integral formulation. *J. Mech. Phys. Solids* **50**, 471–500.
- [14] Bigoni, D. and Capuani, D. (2005) Time-harmonic Green’s function and boundary integral formulation for incremental nonlinear elasticity: dynamics of wave patterns and shear bands. *J. Mech. Phys. Solids* **53**, 1163–1187.
- [15] Bigoni, D., Capuani, D., Bonetti, P. and Colli, S. (2007) A novel boundary element approach to time-harmonic dynamics of incremental nonlinear elasticity: the role of pre-stress on structural vibrations and dynamic shear banding.. *Comput. Meth. Appl. Mech. Engrg.* **196**, 4222–4249.
- [16] Biot, M.A. (1965) *Mechanics of incremental deformations*. New York, Wiley.
- [17] Broberg, K.B. (1999) *Cracks and fracture*. Academic Press, San Diego, CA, USA.
- [18] Brun, M., Capuani, D. and Bigoni, D (2003a) A boundary element technique for incremental, nonlinear elasticity. Part. I: Formulation. *Comput. Meth. Appl. Mech. Engrg.* **192**, 2461–2479.

- [19] Brun, M., Capuani, D. and Bigoni, D. (2003b) A boundary element technique for incremental, nonlinear elasticity. Part. II: Bifurcation and shear bands. *Comput. Meth. Appl. Mech. Engrg.* **192**, 2481–2499.
- [20] Cristescu, N.D., Craciun, E.M. and Soós, E. (2004) *Mechanics of elastic composites*. Chapman & Hall/CRC, Boca Raton.
- [21] Dascalu, C. and Homentcovschi, D. (1999) Uniform asymptotic solutions for lamellar inhomogeneities in anisotropic elastic solids. *SIAM J. Appl. Math.* **60**, 18–42.
- [22] Erdogan, F. and Sih, G.C. (1963) On the crack extension in plates under plane loading and transverse shear. *J. Bas. Eng.* December, 519–527.
- [23] Erdogan, F. and Gupta, G. (1972) Stresses near a flat inclusion in bonded dissimilar materials. *Int. J. Solids Structures* **8**, 533–547.
- [24] Fenistein, D. and van Hecke, M. (2003) Kinematics - Wide shear zones in granular bulk flow. *Nature (London)* **425**, 256–256.
- [25] Gajo, A., Bigoni, D. and Muir Wood, D. (2004) Multiple shear band development and related instabilities in granular materials. *J. Mech. Phys. Solids* **52**, 2683–2724.
- [26] Ghatak, A. and Chaudhury, M.K. (2003) Adhesion-induced instability patterns in thin confined elastic film. *Langmuir* **19**, 2621–2631.
- [27] Gioia, G. and Ortiz, M. (1996) The two-dimensional structure of dynamic boundary layers and shear bands in thermoviscoplastic solids. *J. Mech. Phys. Solids* **44**, 251–292.
- [28] Guz', A.N. (1999) *Fundamentals of the three-dimensional theory of stability of deformable bodies*. Springer-Verlag, Berlin.
- [29] Hallbäck, N. and Nilsson, F. (1994) Mixed-mode I/II fracture behaviour of an Aluminium alloy. *J. Mech. Phys. Solids* **42**, 1345–1374.
- [30] Harren, S., Lowe, T.C., Asaro, R.J. and Needleman, A. (1989) Analysis of large-strain shear in rate-dependent face-centred cubic polycrystals: correlation of micro- and macromechanics. *Phil. Trans. Roy. Soc. Lond. A* **328**, 443–500.

- 
- [31] Hill, R. (1958) A general theory of uniqueness and stability in elastic–plastic solids. *J. Mech. Phys. Solids* **6**, 236–249.
- [32] Hill, R. (1959) Some basic principles in the mechanics of solids without a natural time. *J. Mech. Phys. Solids* **7**, 209–225.
- [33] Hill, R. (1961) Discontinuity relations in mechanics of solids. In Sneddon, I.N. and Hill, R., eds., *Progress in Solid Mechanics* II. Amsterdam, North–Holland. 247–276.
- [34] Hill, R. and Hutchinson, J. W. (1975) Bifurcation phenomena in the plane tension test. *J. Mech. Phys. Solids* **23**, 239–264.
- [35] Homentcovschi, D. and Dascalu, C. (2000) Uniform asymptotic solutions for lamellar inhomogeneities in plane elasticity. *J. Mech. Phys. Solids* **48**, 153–173.
- [36] Hurtado, J. A., Dundurs, J. and Mura, T. (1996) Lamellar inhomogeneities in a uniform stress field. *J. Mech. Phys. Solids* **44**, 1–21.
- [37] Hutchinson, J.W. and Neale, K.W. (1979) Finite strain  $J_2$  – deformation theory. In ‘Proc. IUTAM Symp. on Finite Elasticity’, D.E. Carlson and R.T. Shield Eds., Martinus Nijhoff, The Hague–Boston–London, 237–247.
- [38] Hutchinson, J.W. and Tvergaard, V. (1980) Surface instabilities on statically strained plastic solids. *Int. J. Mech. Sci.* **22**, 339–354.
- [39] Hutchinson, J.W. and Tvergaard, V. (1981) Shear band formation in plane strain. *Int. J. Solids Structures* **17**, 451–470.
- [40] Kardomateas, G.A. (1986) Fractographic observations in asymmetric and symmetric fully plastic crack growth. *Scripta Metall.* **20**, 609–614.
- [41] Kardomateas, G.A. and McClintock, F.A. (1989) Shear band characterization of mixed mode I and II fully plastic crack growth. *Int. J. Fracture* **40**, 1–12.
- [42] Koiter, W.T. (1955) On the diffusion of load from a stiffener into a sheet. *Quart. J. Mech. Appl. Math.* **VIII**, 164–178.
- [43] Ladyzhenskaya, O.A. (1963) *The mathematical theory of viscous incompressible flow*. Gordon & Breach, New York.

- [44] Lekhnitskii, S.G. (1981) *Theory of Elasticity of an Anisotropic Body*. Mir Publisher, Moscow.
- [45] Lewandowski, J.J. and Greer, A.L. (2006) Temperature rise at shear bands in metallic glasses. *Nature (London)* **5**, 15–18.
- [46] Li, Y., Cui, L.S., Xu, H.B. and Yang, D.Z. (2003) Constrained phase-transformation of a TiNi shape-memory alloy. *Metall. Mater. Trans. A* **34**, 219–223.
- [47] McClintock, F.A. (1971) Plasticity aspects of fracture. In: ‘Fracture. An Advanced Treatise’, Edited by H. Liebowitz, Vol. **III**, Academic press Inc., New York, 47–225.
- [48] Michler, G.H., Adhikari, R. and Henning, S. (2004) Micromechanical properties in lamellar heterophase polymer systems. *J. Mat. Sci.* **39**, 3281–3292.
- [49] Misra, S. and Mandal, N. (2007) Localization of plastic zones in rocks around rigid inclusions: Insights from experimental and theoretical models. *J. Geophys. Res.–Solid Earth* **112**, B09206.
- [50] Mooney, M. (1940) A theory of large elastic deformations. *J. Appl. Phys.* **11**, 582–592.
- [51] Muskhelishvili, N.I. (1953) Some basic problems of the mathematical theory of elasticity. P. Nordhoff Ltd., Groningen.
- [52] Neale, K.W. (1981) Phenomenological constitutive laws in finite plasticity *SM Archives* **6**, 79–128.
- [53] Needleman, A. and Tvergaard, V. (1983) In: ‘*Finite elements: Special problems in Solid Mechanics*’, J.T. Oden and G.F. Carey Editors **V**, 94.
- [54] Needleman, A. and Ortiz, M. (1991) Effects of boundaries and interfaces on shear–band localization. *Int. J. Solids Structures* **28**, 859–877.
- [55] Öztürk, T., Poole, W.J. and Embury, J.D. (1991) The deformation of Cu–W laminates. *Materials Sci. Engng.* **A148**, 175–178.
- [56] Öztürk, T., Mirmesdagh, J., Ediz, T. (1994) Strain partitioning and plastic flow in some metal/metal laminates. *Mater. Sci. Eng.* **A175**, 125–129.

- [57] Palmer, A.C. and Rice, J.R. (1973) The growth of slip surfaces in the progressive failure of over-consolidated clay. *Proc. R. Soc. Lond. A* **332**, 527–548.
- [58] Petryk, H. (1997) Plastic instability: Criteria and computational approaches. *Arch. Comput. Meth. Engng.* **4**, 111–151.
- [59] Petryk, H. and Thermann, K. (2002) Post-critical plastic deformation in incrementally nonlinear materials. *J. Mech. Phys. Solids* **50**, 925–954.
- [60] Puzrin, A.M. and Germanovich, L.N. (2005) The growth of shear bands in the catastrophic failure of soils. *Proc. R. Soc. Lond. A* **461**, 1199–1228.
- [61] Radi, E., Bigoni, D. and Capuani, D. (2002) Effects of pre-stress on crack-tip fields in elastic, incompressible solids. *Int. J. Solids Structures* **39**, 3971–3996.
- [62] Rice, J.R. (1968) Mathematical analysis in the mechanics of fracture. In: ‘Fracture. An Advanced Treatise’, Edited by H. Liebowitz, Vol. **II**, Academic press Inc., New York.
- [63] Rice, J.R. (1973) *Plasticity and Soil Mechanics*, A.C. Palmer Ed., Cambridge University Eng. Dept., Cambridge, 263.
- [64] Rittel, D., Wang, Z.G. and Merzer, M. (2006) Adiabatic Shear Failure and Dynamic Stored Energy of Cold Work. *Phys. Rev. Lett.* **96** 075502.
- [65] Rudnicki, J.W. and Rice, J.R. (1975) Conditions for the localization of deformations in pressure-sensitive dilatant materials. *J. Mech. Phys. Solids* **23**, 371–394.
- [66] Ryzhak, E. I. (1993) On stable deformation of ”unstable” materials in a rigid triaxial testing machine. *J. Mech. Phys. Solids* **41**, 1345–1356.
- [67] Ryzhak, E. I. (1994) On stability of homogeneous elastic bodies under boundary conditions weaker than displacement conditions. *Q. Jl. Mech. appl. Math.* **47**, 663–672.
- [68] Saffman, P.G. and Taylor, G.I. (1958) The penetration of a fluid into a porous medium or Hele-Shaw cell containing a more viscous liquid *Proc. R. Soc. Lond. A* **245**, 312–329.

- [69] Savin, G.N. (1961) *Stress Concentration around Holes*. Pergamon Press, Oxford-London.
- [70] Sih, G.C. and Liebowitz, H. (1968) Mathematical theories of brittle fracture. In: "Fracture. An Advanced Treatise", H. Liebowitz Editor **II**, 67–190.
- [71] Sulem J. and Ouffroukh, H. (2006) Hydromechanical behaviour of Fontainebleau sandstone. *Rock Mech. and Rock Eng.* **39**, 185–213.
- [72] Truesdell, C. and Toupin, R.A. (1960) The classical Field theories. In Flügge, S., ed., *Encyclopedia of Physics*, III/1. Berlin, Springer-Verlag.
- [73] Tvergaard, V. (1982) Influence of void nucleation on ductile shear fracture at a free surface. *J. Mech. Phys. Solids* **30**, 399–425.
- [74] Tvergaard, V. and Needleman, A. (1980) on the localization of buckling patterns. *J. Appl. Mech.* **47**, 613–619.
- [75] van Hove, L. (1947) Sur l'extension de la condition de Legendre du calcul des variations aux intégrales multiples à plusieurs fonctions inconnues. *Proc. Sect. Sci. K. Akad. van Wetenschappen*, Amsterdam, **50**, 18–23.
- [76] Wang, Z.Y., Zhang, H.T. and Chou, Y.T. (1985) Characteristics of the elastic field of a rigid line inhomogeneity. *J. Appl. Mech.* **52**, 818–822.
- [77] Weissenberg, K. (1935) La mécanique des corps déformables. *Arch. Sci. phys. nat. Genève* **5**, 44–106, 130–171.
- [78] Weissenberg, K. (1948) Abnormal substances and abnormal phenomena of flow. In Proc. Int. Congr. Rheology (1948), I-29–I-46.
- [79] Wu, K-C. (1990) Line inclusion at anisotropic bimaterial interface. *Mech. Materials* **10**, 173–182.
- [80] Xue, Q. and Gray, G.T. (2006) Development of adiabatic shear bands in annealed 316L stainless steel: Part I. Correlation between evolving microstructure and mechanical behavior. *Metall. Mater. Trans. A* **37A**, 2435–2446.
- [81] Zheng, Y.J., Cui, L.S., Zhu, D. and Yang, D.Z. (2000) The constrained phase transformation of prestrained TiNi fibers embedded in metal matrix smart composite. *Mat. Letters* **43**, 91–96.